Stony Brook University

The official electronic file of this thesis or dissertation is maintained by the University Libraries on behalf of The Graduate School at Stony Brook University.

Thermal Transport Properties of Thermally Sprayed Coatings: An Integrated Study of Materials, Processing and Microstructural Effects

A Dissertation Presented

by

Weiguang Chi

to

The Graduate School

in Partial Fulfillment of the

Requirements

for the Degree of

DOCTOR OF PHILOSOPHY

in

MATERIALS SCIENCE AND ENGINEERING

Stony Brook University

December 2007

Stony Brook University

The Graduate School

Weiguang Chi

We, the dissertation committee for the above candidate for the
Doctor of Philosophy degree, hereby recommend
acceptance of this dissertation.

Dr. Sanjay Sampath – Dissertation Advisor
Professor, Materials Science and Engineering

Dr. Andrew Gouldstone - Chairperson of Defense
Professor, Materials Science and Engineering

Dr. T. A. Venkatech
Professor, Materials Science and Engineering

Dr. Jon Longtin
Professor, Mechanical Engineering, Stony Brook University

Dr. Hsin Wang
Materials Science and Engineering Division, ORNL, TN

This dissertation is accepted by the Graduate School

Lawrence Martin
Dean of the Graduate School

Abstract of the Dissertation

**Thermal Transport Properties of Thermally Sprayed Coatings:
An Integrated Study of Materials, Processing and
Microstructural Effects**

by

Weiguang Chi

DOCTOR OF PHILOSOPHY

in

MATERIALS SCIENCE AND ENGINEERING

Stony Brook University

2007

The complex microstructures of thermally sprayed coatings are very sensitive to processing conditions and have a significant influence on the properties. The thermal transport property is a very important design parameter for thermally sprayed coatings. Despite considerable progress in this area, there is continued need to clarify the interrelationships among processing, microstructure and thermal transport properties. This has been enabled through continued advancements in processing science and control, enhancements in microstructural characterization and new methods of property characterization.

The purpose of this research is to seek a successive pathway to prior efforts in understanding the effect of microstructural defects on the thermal transport property of thermally sprayed coatings. Relationship between microstructure and thermal conductivity is investigated for three sets of plasma sprayed yttria stabilized zirconia (YSZ) coating systems made using different morphology powders, different particle size distribution and controlled modification of particle states via plasma torch parameters. By integrating the results, maps of the thermal conductivity-porosity relationship have been established. Such maps highlight the role of splat thickness and interfaces in thermal conductivity. Furthermore, a new microstructural parameter termed "effective porosity" is proposed which considers the dominating role of interlamellar pores on through thickness thermal transport in thermally sprayed coatings. This effective porosity is rationalized based on the heat transport mechanism and enables better understanding of microstructure-thermal transport property correlation. An inverse linear model and a

percolation model are established which can serve as predictive tools for understanding microstructure-thermal conductivity relationships. In addition, a systematic assessment of thermal conductivity anisotropy has been carried out for YSZ, Al_2O_3 and several metallic coatings. These results are analyzed from the point of view of modified percolation theory which considers the effect of anisotropic microstructural defects of sprayed coatings on the thermal transport property.

In the case of the ceramic coatings (YSZ, Al_2O_3), the temperature dependent thermal conductivity is also examined for various starting microstructures in collaboration with the Oak Ridge National Laboratory (ORNL). The decisive role of starting microstructure on temperature dependent thermal conductivity is presented. In addition, sintering effects resulting from thermal cycling and isothermal exposure on both room temperature and temperature dependent thermal conductivity have been carefully examined in an effort to assess the relationship to effective starting microstructure and provide quantitative information for life prediction.

This dissertation also extends to an investigation of thermal conductivity of metal and alloy thermal spray coatings. A range of metallic materials have been considered and the variation of thermal conductivity is interpreted from the point of view of intrinsic attributes (atomic structure, electronic structure and phase structure) as well as extrinsic effects (as a consequence of oxidation and defected microstructure). Finally, in order to achieve precise and reliable measurement of thermal transport property, the applicability and repeatability of both the laser and xenon flash techniques have been examined through the measurements on these coating systems: ceramics, semiconductors, metals, alloys and composites.

Table of Contents

List of Figures

ix

List of Tables

Acknowledgements

I would like to express my sincere gratitude to Prof. Sanjay Sampath, my advisor, for his guidance, encouragement and support throughout the course of this study.

I am also greatly thankful to Prof. Andrew Gouldstone, Prof. Jon Longtin, Prof. T. Venkatech, Prof. Dick Gambino, and Prof. Herbert Herman for their enlightenment, support and fruitful discussions.

I would like to express my special thanks to Dr. Hsin Wang in Oak Ridge National Lab who has given me great help in thermal conductivity measurements.

The sincere appreciation is also expressed to Lysa Russo for her help in some industrial project, Glenn Bancke for his help in preparation of the coatings and Jim Quinn for his help in SEM.

Throughout the course of this program, I have had the pleasure of working with and learning from a number of students and post doctoral researchers. Many thanks to all my past and present colleagues in the Center for Thermal Spray Research and materials science and engineering department for all their help, discussion and friendship, Bhuvaragasamy G Ravi, Anirudha Vaidya, Yuhong Wu, Anand Kulkarni, Martin Friis, Yaping Li, Vasudevan Srinivasan, Yang Tan, Xianzhong Guo, Li Li, QingYu Yan, Alfredo Valarezo, Jose Colmenares, Swarnima Deshpande, Wesley Francillon, Brian Choi, and all the people in CTSR.

Chapter 1.

Introduction

Thermal transport property is a very important design parameter for thermally sprayed coatings. Besides its obvious requirement in thermal barrier coatings, thermal transport is also an important factor in wear applications where heat dissipation through the coating is of critical importance in determining the coating performance. Thermal conductivity is used to represent the thermal transport property of coatings. Thermal conductivity of thermally sprayed materials is substantially reduced from that of its bulk counterpart and can be reduced anywhere from 90% to 10% of bulk values. Unlike bulk materials, the thermal conductivity of thermally sprayed coatings is significantly affected by both the intrinsic attributes of materials and the extrinsic characteristics (microstructural defects, oxidation and temperature). In addition to its obvious importance from coating design and performance, understanding this discrepancy is of fundamental importance in understanding the process-microstructure-property relationships.

The intrinsic attributes of materials determine the heat transport mechanisms in bulk materials. Heat is transported in solid materials by both phonons and free electrons at room temperature [1]. In ceramic materials, phonons play the dominant role in heat transfer due to the lack of free electrons. In metallic materials, the electron mechanism of heat transport plays the dominant role.

Temperature has a significant effect on thermal conductivity. For ceramic materials, such as YSZ, the variation of dominant mechanism of heat transport occurs at high temperature. Figure 1.1 shows the temperature dependent thermal conductivity of YSZ coating. The thermal conductivity of YSZ material monotonically decreases from room temperature to $800^{o}C$ or so because scattering of phonons becomes more pronounced with rising temperature. The shape of the thermal conductivity curves is a result of phonon conduction mechanism up to $800^{o}C$. The thermal conductivity is limited by intrinsic phonon scattering scales as $1/T$ [2]. At higher temperatures, the photon conduction (radiation) becomes increasing important and results in a faster elevation of thermal conductivity (proportional to T^3) [1]. In addition, for ceramic coatings, the densification of the coatings occurs at high temperature since the pores are prone to high temperature sintering. The sintering is closely related to the time-at-temperature and cycle annealing mechanisms as well as can decrease the conductivity reduction benefit and even bring on the failure of coatings. Both the time-at-temperature and cycle

annealing result in the change of pore morphology and the closure of interlamellar pores/interfaces, which increases thermal conductivity of TBCs.
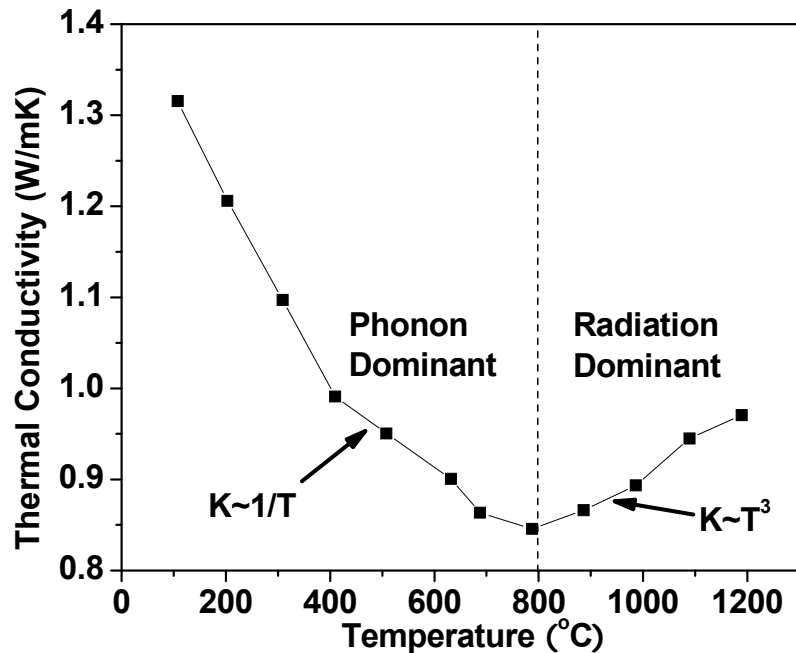
Figure 1.1 Temperature dependent thermal conductivity of YSZ coating

For thermally sprayed coatings, one of the most important extrinsic effects on thermal conductivity is the anisotropic defected microstructure generated by the splat deposited process. The complex anisotropic microstructures of coatings are intimately related to the particle molten state and kinetic state and have proved to be very sensitive to the processing parameters (power level, spray environment, feedstock characteristics, standoff distance, substrate conditions and gas flow). In the case of YSZ coatings, a number of microstructural defects arising from the stochastic spraying process exhibit, such as interlamellar pores (resulting from splat based layered coating build-up), microcracks (associated with relief of quenching stresses) and globular pores (arising from lack of complete filling) [3]. The defected microstructure comprising of pores and cracks contribute substantially to the reduced thermal conductivity of YSZ coatings, which is only about 40% of the bulk value of thermal conductivity [4]. The material alone can not describe such an enormous reduction in thermal conductivity. It is necessary to establish the relationships between microstructural defects and thermal transport property through reliable and practical characterization of both microstructural features and thermal conductivity.

In this study, an integrated and systematic assessment of thermal conductivity dependent factors is carried out for thermally sprayed coatings from the point of view of intrinsic attributes of materials and extrinsic effects (spraying processing and defected microstructure). A range of materials, such as YSZ, Al_2O_3, semiconductor, single element

metals, Ni and Co based alloys, cermets, FGMs, are selected to make coatings using different spraying techniques to examine the material and processing effects on thermal conductivity. The variations of the thermal transport properties arising from the materials are elucidated from the aspects of process induced oxidation, phase structure as well as intrinsic characteristics of materials such as valence electron, atomic structure and crystal structure. The effect of spraying techniques (APS, HVOF and CS) on thermal conductivity is interpreted from the particle state and the consequential oxidation and interfaces.

The characterization of microstructural characteristics and the assessment of thermal conductivity techniques are also performed to explore the effect of microstructural defects on the thermal transport property. To define the microstructure, a variety of methods are adopted including image analysis (IA), precision density, Archimedes' method, pycnometer and mercury intrusion porosimetry (MIP). Effective porosity is established according to the physical mechanism of heat transfer based on "Loeb Theory" which considers the effect of pore morphology in addition to porosity [5]. An inverse linear model and a percolation model are established to interpret the microstructure-thermal conductivity relationship. In addition, various techniques of thermal conductivity measurements are examined for wide range of materials to achieve precise and reliable measurement of thermal transport property. Research in collaboration with Oak Ridge National Laboratory has been carried out to explore the thermal conductivity of coatings as a function of temperature. The stability of the starting microstructure to thermal aging is also considered for both room temperature and temperature dependent thermal conductivity.

This study will advance the understanding of processing-microstructure-thermal transport property relationships of thermally sprayed coatings made of various materials and allow tuning the thermal transport property to meet future design needs.

Background

1.1. Effect of Intrinsic Attributes of Materials on Thermal Conductivity

1.1.1 Thermal Transport in Solids

In the case of fully dense bulk solid materials thermal conductivity is only related to intrinsic attributes of materials. This primarily relates to crystal structure, atomic structure and grain size and boundaries etc. The effect of intrinsic attributes itself can be examined by using bulk solid materials. Different mechanisms play the dominant role in heat transfer for various materials.

1.1.1.1 Thermal transport in ceramics

Ceramic materials are thermal insulators due to the lack of a large number of free electrons. Consequently, the phonon conduction mechanism predominates for thermal transport [1]. The thermal conductivity of cearmics can be expressed as

$$K = \frac{1}{3}CvVl$$

where Cv is the specific heat per unit volume, V is the velocity of heat carriers (phonons for ceramics at room temperature) and l is the mean free path. The specific heat is determined by the intrinsic attributes of materials. Velocity generally is treated as a constant for the same heat carrier (phonon). The mean free path is intimately related to atomic/molecular diameter and concentration. The intrinsic specific heat and mean free path result in the room temperature thermal conductivities of oxide ceramics in a range from 2 to 50 W/mK [1].

The phonon scattering becomes more pronounced with the increase of temperature. The thermal conductivity of most ceramic materials decreases with rising temperature, which is normally inversely proportional to the temperature [1]. This is at least true at relatively low temperature. At higher temperature, the thermal conductivity of ceramics increases with temperature owing to the photon heat transfer. The thermal conductivity arising from photon conduction is [1]

$$K = \frac{16}{3}\pi\sigma_s n^2 l_r T^3$$

where n is the refractive index, lr is the mean free path of phonons and σ s is the Stefan-Boltzmann constant (5.67×10^{-8} W·m^{-2}·K^{-4}). Therefore, the thermal conductivity of ceramics at higher temperatures becomes proportional to T^3.

1.1.1.2 Thermal transport in metals

In high-purity metals, the heat transport is dominated by electrons. The thermal conductivity of metals increases with the free electron concentrations due to more participation in heat transport process as well as the electron mobility. For example, the bulk materials, Ag, Cu, Al and Mo, have very high thermal conductivities with different values. The thermal conductivity from the highest to the lowest is Ag (430W/mK) >Cu (400W/mK) >Al (235W/mk) >Mo (140W/mK). The reason can be interpreted from their atomic characteristics. The valence electrons experience both the attraction force from the nuclei and the repulsion from other electrons. The atomic radius, atomic weight, electron drift mobility, electron concentration and configurations all influence the thermal conductivity. The electron configurations of Ag, Cu, Al and Mo are $1s^22s^22p^63s^23p^63d^{10}4s^24p^64d^{10}5s^1$, $1s^22s^22p^63s^23p^63d^{10}4s^1$, $1s^22s^22p^63s^23p^1$, $1s^22s^22p^63s^23p^63d^{10}4s^24p^64d^55s^1$ and some other characteristics of these metals are listed in Table 1.1. From the electron configurations, all the four metals have one outmost valence electron and similar atomic radius. The number (47) of electrons of Ag is the highest and therefore its valence electron is subject to the largest repulsion force. It is very easy for the valence electron to be removed from the atom and form free electron. With the decrease of the number of electrons, the repulsion force becomes smaller and more energy is required to form free electron, as it is shown in the case of Cu and Al. For the Mo, its 4d state is not fully filled out. The trend of attracting electron makes it difficult to remove the 5s^1 to form and transport free electron. The free electrons contribute to both electrical and thermal conductivity and the relation between thermal conductivity and electrical conductivity of single element metals follows the Wiedemann-Franz law as below [1]:

$k = \sigma TL$

where k is thermal conductivity, σ is electrical conductivity, T is the absolute temperature, and L is Lorenz number-a constant ($2.44\times10^{-8}\Omega \bullet W / K^2$). The electrical conductivity is proportional to the electron drift mobility and electron mobility. The highest electron drift mobility of Ag gives rise to the highest electrical conductivity and thus thermal conductivity. The thermal conductivity of Cu is lower than that of Ag due to the slower electron drift mobility despite of the higher electron concentration. The electron concentrations of Al and Mo are similar to that of Ag. However, the slower electron drift mobility generates the lower thermal conductivity. The thermally sprayed coatings follow the same sequence Ag>Cu> Al> Mo even if there are some different decreased magnitudes compared to bulk values. Therefore, intrinsic thermal conductivity of bulk samples is related to electron concentration and mobility which are controlled by atomic/electronic structure.

Table 1.1 Characteristics of some single element metals

materials	atomic radius (m)	atomic weight	melting point (^{o}C)	electron drift mobility ($cm^2V^{-1}s^{-1}$)	electron concentration (cm^{-3})
Ag	1.6×10^{-10}	108	960	65	6×10^{22}
Cu	1.35×10^{-10}	63.5	1085	43.4	8.5×10^{22}
Al	1.43×10^{-10}	27	660	39.2	6×10^{22}
Mo	1.39×10^{-10}	96	2610	20	6.5×10^{22}

1.1.2 Thermal Transport in Coatings

The intrinsic attributes of materials will be transferred to and kept in the thermally sprayed coatings despite the introduced extrinsic effects arising from process. The intrinsic thermal conductivity of either ceramics or metals determines the coating thermal conductivity. The effects of intrinsic attributes of materials on thermal conductivity will be examined for ceramic coatings (YSZ and Al_2O_3), single elemental metallic coatings (Ag, Cu, Al, Mo) and alloy coatings (Ni-based and Co-based) in this dissertation.

1.2. Extrinsic Effects on Thermal Conductivity

Although there are significant effects of intrinsic attributes on thermal conductivity, the extrinsic effects arising from spraying process substantially change the thermal transport properties of coatings compared with their bulk counterpart. The extrinsic effects are related to the sprayed materials. Ceramic coatings and metallic coatings include different extrinsic effects.

For ceramic coatings, the extrinsic effects are mainly microstructural defects which lead to significant phonon scattering and therefore dramatically reduce the thermal transport property. In the case of YSZ coatings, the microstructural defects consist of three types of pores: interlamellar pores (resulting from splat based layered coating build-up), microcracks (associated with relief of quenching stresses) and globular pores (arising from lack of complete filling), as shown in Fig. 1.2 [3, 6]. These three types of pores fall into different ranges of size distribution as shown in Fig. 1(a). Globular pores are coarse pores in the size range 3~10 μm. The size distribution of interlamellar pore is approximately in 0.1~3 μm. The cracks have the smallest size, around 0.01~0.5 μm. A great deal of computational modeling had been successfully carried out to characterize the coating microstructure [3, 6]. The coating thermal conductivity is strongly dependent on the pore morphology and porosity. The effect of microstructural defects will be discussed to detail in this dissertation.

(a)   (b)
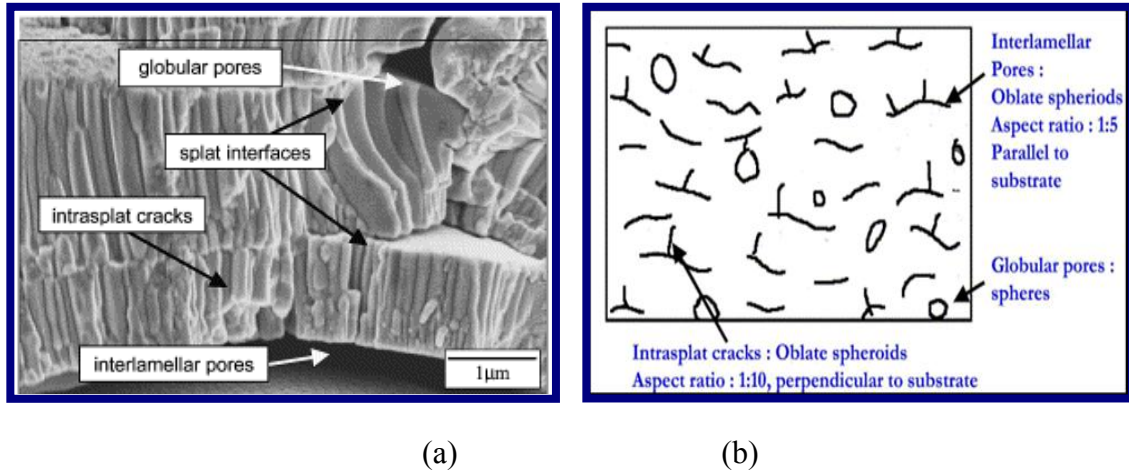
Figure 1.2 YSZ coating microstructure (a) image [6] (b) model [3]

In addition, at higher temperatures, the photon conduction becomes increasingly important for YSZ coatings. The microstructural defects in the heterogeneous YSZ coatings result in the scattering, reflection and absorption of photons at high temperature[7]. Therefore, the high temperature thermal conductivity is influenced by pore features, such as porosity, pore size and pore morphology. Quantitative correlations between microstructural defects and thermal radiation photon transport are required to be investigated in the future step.

For metallic coatings, the extrinsic effects on thermal conductivity include microstructural defects and oxidation arising from spraying processing. Figure 1.3 shows the microstructural defects (interlamellar pores and globular pores) and oxide in metallic NiAl coating [8]. The microstructural defects and oxide arising from spraying processing are intimately related to the different spraying techniques and significantly change the thermal transport properties of coatings as compared to bulk materials. The investigation of extrinsic effects on thermal conductivity will be carried out for single elemental metallic coatings and Ni/Co based alloy coatings.
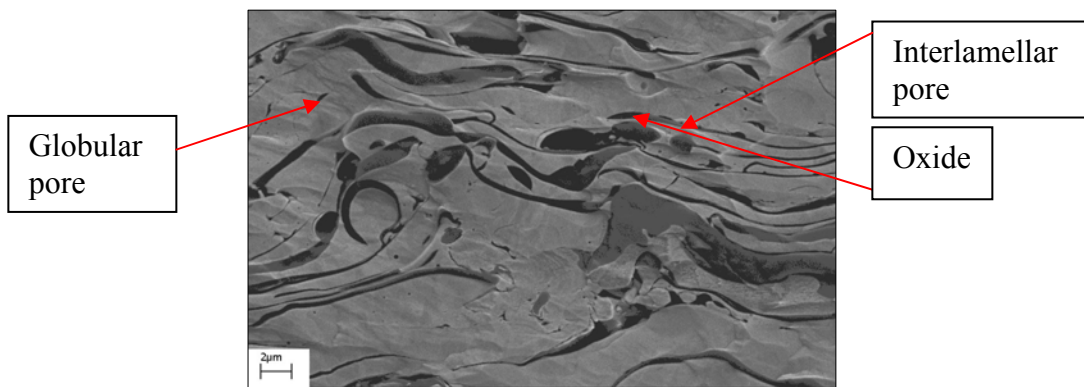
Figure 1.3 Microstructural defects and oxide in metallic NiAl coating [8]

To examine extrinsic effects on thermal conductivity, it is necessary to achieve precise and reliable microstructural characterization. However, the complex microstructure of thermally sprayed coatings offers a significant challenge in defining the microstructural features. In addition, determining a suitable theory to enable interpretation and predication of thermal conductivity change with extrinsic effects are of value to both science and technology.

1.2.1 Microstructural Characterization of Thermally Sprayed Coatings

To achieve precise and reliable microstructural characterization, numerous techniques have been developed [9]. The principal techniques are described as below: image analysis (IA), mercury intrusion porosimetry, computed microtomography and small angle neutron scattering. Earlier studies on microstructural characterization using these techniques as well as their advantages and disadvantage are discussed.

1.2.1.1 Established characterization methods

1.2.1.1.1 Earlier studies of image analysis

Image analysis method is widely used for the characterization of microstructure due to its straightforward, versatile, reliable and inexpensive feature.

Work by Fowler et al. [10] have shown that image analysis methods can reproducibly detect and measure microstructural features (pores, cracks, etc.) within thermally sprayed coatings. The reliability of these methods for specific experiments and metallographic conditions was statistically tested to give a 95% confidence level. Lavigne et al. [11] established a method with good reliability and reproducibility for TBCs porosity characterization using SEM and IA. Mailhot et al. [12] have also applied IA to porosity analysis for supersonic induction plasma sprayed electrolyte layers of solid oxide fuel cells (SOFC) and the threshold value was obtained in a region where the porosity had a sudden jump with a small change of that value.

Besides porosity, image analysis has been used for many other features of coatings. Fowler et al. [10] and Bluni et al. [13] applied IA to the characterizations of coating thickness, oxides and inter-splat grain size. Study by Schorr et al. [14] showed the use of IA for the carbide and oxide phases in FeCrAlY coatings. Zhu et al. [15] have obtained the distribution of steel, copper, oxide by IA from RGB images instead of gray scale images. Markov and Preziosi [16] developed the IA method to predict some properties through microstructure characterization via statistical correlation functions. A local volume averaging method was established by Kaviany et al. [17] for heat transfer analysis in periodic porous materials. Kachanov et al. [18, 19] have employed image analysis on modeling the parallel family and the perpendicular family and estimating the effective anisotropic properties of the coatings. Leigh and Berndt [20, 21] assumed the pores to be elliptical and determined their size–shape distribution for a water-stabilized plasma-spray-formed Al_2O_3–13 wt% TiO_2 coating using quantitative stereological analysis. Numerous studies have been carried out for the effective elastic constants of porous materials [22-27], which can be categorized into two groups: non-interacting

models (without the influence of neighboring pores) and interacting models (including this neighbor's influence). The self-consistent, differential and Mori-Tanaka schemes [28, 29] methods were also employed in image analysis.

Recently, Deshpande et al. [30] have systematically studied splats and coating microstructures. The versatility of IA methods for microstructural quantification was investigated for thermally sprayed coatings made by different spraying techniques and made of various feedstock characteristics. In this work, the IA methods were successfully applied to alumina coatings made by APS and HVOF and YSZ coatings made of different morphology and particle size distribution powders. Deshpande et al. [30] have also employed IA to evaluate the oxidation of metallic coatings and its role in the evolution of the microstructure. In-flight oxidation and the oxidation generated after impact determines the nature of splats and results in the microstructural difference. Therefore, oxidation can significantly affect the phase composition, microstructure, properties and performance of thermally sprayed metallic coatings.

Although IA is relatively simple, versatile and easier to interpret, IA measures two dimensional quantities, which give rise to error.

1.2.1.1.2 Mercury Intrusion Porosimetry (MIP)

MIP can achieve 3D characterization for thermally sprayed coatings. It can detect a number of microstructural parameters including pore size, pore shape, pore connectivity and surface area. Although the absolute values of the determined pore information were different, the relative changes between the MIP (3D) and the image analysis (2D) track in a consistent manner. Kulkarni et al. [3, 6, 31, 32] have successfully utilized MIP to measure porosity and density of ceramic coatings. However, MIP only traces surface-connected pores and provides a lower total porosity owing to its inability to penetrate closed pores.

1.2.1.2 Advanced microstructural characterization methods

Although the traditional microstructural characterization methods reveal a great deal of microstructural information, their apparent disadvantages have pointed to the continued need for the development of microstructural definition. Advanced techniques, such as computed microtomography and small angle neutron scattering, are developed to quantify microstructure.

1.2.1.2.1 Computed Microtomography (CMT)

X-ray CMT is a powerful non-destructive tool for 3D imaging of microstructure of thermally sprayed coatings. Kulkarni et al. [32] investigated Al_2O_3 coatings by using CMT to elucidate microstructure-property correlations. The volumetric data of elemental composition can be obtained by mapping 3D X-ray absorption through the sample. A linear array of detectors is adopted to record the data of linear attenuation coefficient (LAC), which depends on the physical density of the material, the effective atomic

number and the X-ray beam energy [33]. Then, the data are analyzed using Fast Filtered Back Transform algorithm to reconstruct horizontal slices and 3D images of density maps at 2.7 μm resolution are built up by stacking these slices. The 3D CMT images consist of point-to-point LAC and eliminate the limitation of conventional radiography to distinguish between thickness and density changes [34-36]. Thus, the quantitative information of the microstructural features, such as the porosity, pore size, surface area and pore connectivity can be examined for thermally sprayed coatings. CMT has been successfully used to assess interconnectivity of pore or elements in geological and biological materials [37]. However, CMT is not able to fulfill the quantitative delineation for the component porosities and only total porosity can be obtained. In addition, alumina based coatings are more suitable for this technique than YSZ coatings due to large X-ray absorption coefficient of YSZ material.

1.2.1.2.2 Small Angle Neutron Scattering (SANS)

SANS is an efficient and valuable technique to obtain more information on porosity, microcracks, pore size distribution, surface area and orientation distribution. In this approach, the pore morphology is idealized by artificially rebuilding according to the collective microstructural information: the opening dimensions and orientation. During the operation of the SANS, monochromatic neutrons pass through the specimen in transmission geometry and the scattered neutrons are recorded on a 2D detector. The scattering occurs at the void–grain interface owing to differences in scattering length density between the material and the pores. SANS provides the total void surface area per unit sample volume, independent of the precise void morphology. The fine features in the microstructure are intimately related to surface area. SANS also yields the information of microstructural anisotropy through a measurement of the beam-broadening arising from anisotropic multiple scattering of long wavelength neutrons. The coarse features in the microstructure are major contributors to the anisotropic multiple scattering. A combination of these two derived results along with the total porosity gives quantitative information of the microstructural features, such as the porosity, pore size and orientation for different morphology pores (interlamellar pores, intrasplat cracks and globular pores). Ilavsky et al. [38] and Kulkarni et al. [3] have employed multiple small angle neutron scattering in conjunction with appropriate scattering models of the pore solid interfaces to delineate the pore morphology [39].The application of self consistent models to describe the microstructure has allowed for quantitative definition of the coating into its anisotropic defect contributors namely, interlamellar pores (resulting from splat based layered coating build-up), microcracks (associated with relief of quenching stresses) and globular pores (arising from lack of complete filling). These void features are classified on the basis of aspect ratios, 1:1, 1:5 and 1:10 for globular pores, interlamellar pores and intrasplat cracks, respectively. In a related study, Wang et al. [6], assessed the contribution of the various microstructural features of plasma sprayed YSZ on its room temperature thermal conductivity. They concluded that the pore architecture alone cannot describe the more than 60% reduction in thermal conductivity and the contribution from splat interfaces (from successively formed, rapidly quenched and flattened droplets) plays a significant role.

However, SANS appears ineffective to the pores whose size is larger than 2μm. This method is quite complex and require expensive equipments and experienced person. It is time-consuming and therefore not convenient to perform, which makes this method not able to be widely used in industry.

All these studies indicate the significant effect of porosity on thermal conductivity, especially interlamellar porosity. The same porosity contributed by interlamellar pores reduces thermal conductivity more than those contributed by globular pores. Although the phenomenon has been observed, there is no theoretical treatment to interpret the reason. To accomplish this, we examine this literature [5] on thermal conductivity measurements in morphologically defected systems and apply those findings as relevant to thermally sprayed coatings. The theory which elucidates the important role of interlamellar porosity in thermal conductivity is described below.

1.2.2. A Theory for the Important Role of Interlamellar Porosity

In porous media, there are three mechanisms for heat transport: heat conduction, radiation and convection. The convection can be neglected for the porous media with small pores. With an assumption that the heat flux is unidirectional and the unidirectionality is not disturbed by pores, Loeb [5] established a theory for the effective thermal conductivity of porous media, which indicated the relation of the conductivity to the emissivity of pore surface, to the size, shape, and distribution of pores.

The thermal conductivity is defined in terms of the expression

$$W = -k \frac{dT}{dx}$$

where T is the temperature, x is the distance along flow direction, k is thermal conductivity, and W denotes the amount of heat crossing a unit area in unit time.

If the temperature distribution over any pore surface is known, the amount of heat per unit time per unit area across a small temperature drop ΔT should be

$$W = 4\varepsilon\sigma T^3 \Delta T$$

where ε denotes the emissivity of radiating surface, σ is Stefan's radiation constant and is equal to $5.735*10^{-5}$ erg/(cm$^3\cdot$ s $\cdot$deg), T is the average absolute temperature of the region across which radiation occurs.

Figure 1.4. shows the heat transport for a globular pore with the isotherms and lines of heat flux. W is constant along any line of flux. The linearity of heat flux makes the temperature drop proportional to the distance. In Fig. 1.4, four pointes A, B, P and Q are marked. A and B lie on the isotherms that are tangent to the pores representing respectively the temperature T_1 and T_2. P and Q lie on the pore surface. The distance from the center of the pore to the line AB is y. The temperature drop ΔT_{PQ} between P and Q is proportional to the distance PQ

$$\frac{\Delta T_{PQ}}{T_1 - T_2} = \frac{PQ}{AB}$$

For a pore with radius of r,

$$\frac{\Delta T_{PQ}}{T_1 - T_2} = \frac{2\sqrt{r^2 - y^2}}{2r} = \sqrt{1 - (\frac{y}{r})^2}$$

The effective radiating surface for a set of flow lines whose projection on Fig. 1.4. is line AB is chosen as a circular strip with radius y and width dy, in planes perpendicular to the heat flux lines. The amount of heat for the circular strip is

$$W 2\pi y dy = 8\varepsilon\sigma T^3 \Delta T_{PQ}\pi y dy = 8\varepsilon\sigma T^3 \sqrt{1 - (\frac{y}{r})^2}(T_1 - T_2)\pi y dy$$

The total amount of heat across the globular pore is

$$\int_0^r W 2\pi y dy = 8\pi\varepsilon\sigma \bullet r^2 T^3 (T_1 - T_2)\int_0^1 \sqrt{1 - x^2}\, x dx = \frac{8\pi}{3}\varepsilon\sigma \bullet r^2 T^3 (T_1 - T_2)$$

So, the average amount of heat across the pore per unit area is

$$\overline{W} = \frac{8\pi}{3}\varepsilon\sigma \bullet r^2 T^3 (T_1 - T_2) = \overline{k}\frac{T_1 - T_2}{2r}$$

$$\overline{k} = \frac{16}{3}r\varepsilon\sigma T^3$$
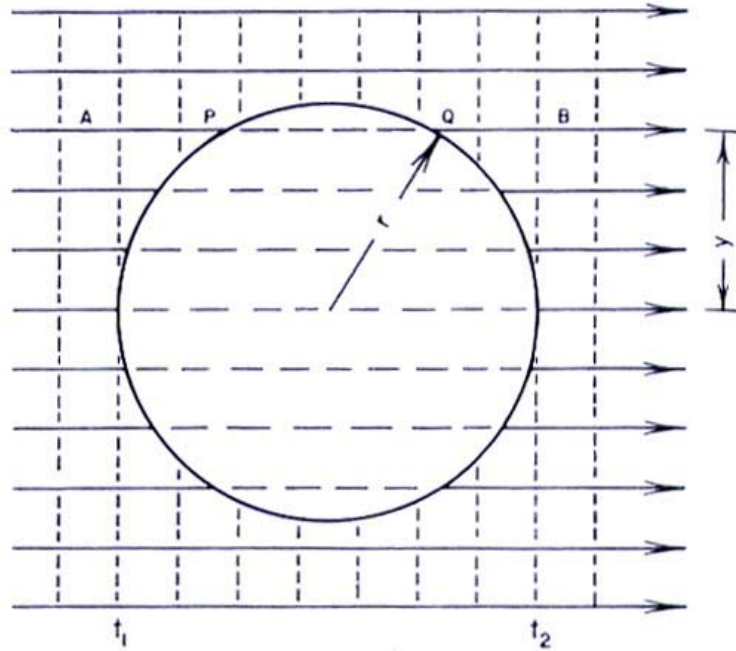
Figure 1.4 Heat flow across a pore [5]

For a cylindrical pore with the axis perpendicular to the heat flux, the effective radiating surface for a set of flow lines whose projection on Fig. 1.4. is line AB may be chosen as a rectangular strip of length l (the length of the cylindrical pore) and of width dy, oriented with the long side parallel to the axis of the cylinder and with the short side

perpendicular to the direction of heat flux. Using equation $W = 4\varepsilon\sigma T^3 \Delta T$, the amount of heat for such a strip from P to Q can be expressed as

$$Wldy = 4\varepsilon\sigma T^3 \Delta T_{PQ} ldy = 4\varepsilon\sigma T^3 \sqrt{1-(\frac{y}{r})^2}(T_1 - T_2)ldy$$

The entire amount of heat across the pore is

$$\int Wldy = 4\varepsilon\sigma T^3 (T_1 - T_2)l \int_{-r}^{r} \sqrt{1-(\frac{y}{r})^2}\, dy = 2\varepsilon\sigma T^3 (T_1 - T_2)lr\pi$$

So, the average amount of heat across the pore per unit area is

$$\overline{W} = \pi\varepsilon\sigma T^3 (T_1 - T_2) = \overline{k}\, \frac{T_1 - T_2}{2r}$$

$$\overline{k} = 2\pi r\varepsilon\sigma T^3$$

For a cylindrical pore with the axis parallel to the heat flux, the heat per unit area is

$$\overline{W} = 4\varepsilon\sigma T^3 (T_1 - T_2) = \overline{k}\, \frac{T_1 - T_2}{d}$$

where d is the width of gap, so

$$\overline{k} = 4d\varepsilon\sigma T^3$$

The different morphology pores in thermally sprayed coatings can be modeled as simple geometric figures according to the above-mentioned Loeb's theory. The globular pores in thermally sprayed coatings are equal to the globular pores in Fig. 1.4. Considering that the region between splats is not completely empty, and there is more or less contact, the interlamellar pore can be approximated as a roll of cylinders (roller model) whose axes are perpendicular to the heat flux. The vertical cracks are also treated as cylinders with axes perpendicular to the heat flux. This modeling offers a chance to unify various-morphology pores to be just a second phase according to the heat transport mechanism and simplify the determination of the relationships between microstructural defects and thermal conductivity. The further investigation will be carried out in this dissertation.

1.2.3 Theoretical Technique for Disordered Systems (Percolation)

Loeb Model points out the significant effect of pore geometry on thermal conductivity and is successfully used to elucidate the important role of interlamellar porosity. However, the change of thermal conductivity with the volume of pores can not be fully interpreted and predicted by Loeb Model. Additional theoretical strategies are needed.

Percolation theory provides a well defined and intuitively satisfying model to interpret and predict the thermal conductivity change with pore volume for random systems. The term percolation for the statistical-geometry model was created in 1957 by the mathematician J.M. Hammersley [40]. This theory is suitable for a broad range of physical phenomena. In this percolation model, there is a sharp phase transition point at which long-range connectivity suddenly appears with the increase of connectedness or density or occupation or connection. This qualitative change in a go/no-go manner is

called percolation transition, which constitutes the percolation threshold Pc. For the connected fraction smaller that percolation threshold, there exists no connected path. This percolation theory has a tacit assumption that the ratio of the dimension to the bond lattice is infinite. There is no percolation in one dimension since Pc=1.

Figure 1.5 shows the behavior of key percolation probability P (p) and random-network electrical conductivity σ as a function of fraction (p) of filled bonds [41]. The percolation probability P is the fraction of the entire system that is taken up by the percolation path. That is, the chance of a randomly chosen bond being connected bond that belongs to the infinite cluster is P as the fraction of connected bonds is p. It is obvious that P is less than p excluding the filled system (P=p=1). The sameness of and difference between the probability and the electrical conductivity can be observed from Fig. 1.5. For the sameness, both the probability and the electrical conductivity are functions which take off from zero at the percolation threshold p_c and then grow monotonically to a finite maximum value at p=1. The probability and the electrical conductivity vanish throughout the low density regime. The difference is that P rises very steeply just above p_c whose initial slope is infinite at threshold whereas the electrical conductance shows a very soft rise with an initial slope zero. This behavior is called critical phenomena, which is controlled by critical exponents. The explosive growth in P displays the rapidity of contention between finite clusters and the infinite ones when the concentration exceeds Pc. The reason is that a finite cluster joins up with previously formed percolation path with the increase of p, which contributes to the percolation probability P. But for the macroscopic current, the new bonds add nothing in the way of a new parallel path because they do not lead anywhere. Just above threshold, only a negligible fraction contributes to the conductivity and thus the electrical conductivity has a slow start. That is, the impedance of the extended network is immense near threshold.

The percolation concepts in amorphous solid-state physics have been successfully applied to two phenomena: the glass transition (for atomic motion) and the Anderson transition (for electronic motion). Lobb, Skocpol, and Tinkham [42] and Tinkham [43] have reported electrical-resistivity measurements on a system consisting of superconducting niobium filaments imbedded in a copper matrix, and obtained a critical exponent s=1.05, which is higher than the reported value 0.5<s<0.9 [44] due to the highly anisotropic nature of the system.

The percolation theory has also been successfully used to evaluate the anisotropic microstructures [45].The orientations of pores and cracks for the microstructures of the networks tend to be either parallel or normal to the substrate, with an orientational scatter around these preferential orientations. The microstructural anisotropy results in the anisotropy of the effective electrical conductive properties and gives rise to different percolation thresholds, as shown in Fig. 1.6. The increase of anisotropy will decrease half of the conductor in the array, and will thus decrease the net conductance of the array. It is found that increasing microstructural anisotropy at a constant f shortens the inclusions in the direction parallel to the current and proportionately widens them in the direction perpendicular to the current. Thus, the current is effectively blocked over a wider region and the effective conductivity is reduced significantly due to the large depolarization factor of the slits. Therefore, the effects of the anisotropy are nontrivial and fairly dramatic, in that a small variation of anisotropy can cause a sizeable change in the conductance.

In the critical region in which $|p - p_c| \ll 1$, the percolation functions are observed to obey power-law from threshold. The two-state property has asymptotic scaling behavior, as shown in Fig. 1.5 [41]. It is very difficult to obtain an unambiguous value for the critical exponent, which depends strongly on the precise choice of the percolation threshold and the extent of the asymptotic region over which the fit is presumed to be reasonably valid. Smith et al. [45] used percolation theory to investigate the anisotropy of 2-dimensional conductor-insulator networks and found that the critical exponents increase with the decrease of aspect ratio (represent the anisotropy of microstructure) when the percolation threshold is the same for all samples. However, experimental work on 3D continuum systems often produces values of critical exponent higher than those obtained from numerical simulation of lattice networks. Deptuck et al. [46] found that the critical exponents of electrical conductivity and elasticity for a three-dimensional percolation system including sintered, submicron, silver power are respectively 2.15±0.25 and T=3.8±0.5, larger than the theories and numerical simulations by taking account of the anisotropic nature. Measurements on anisotropic networks and numerical simulations indicate that percolation threshold, critical exponent and the size of the "asymptotic region" vary with the degree of anisotropy.
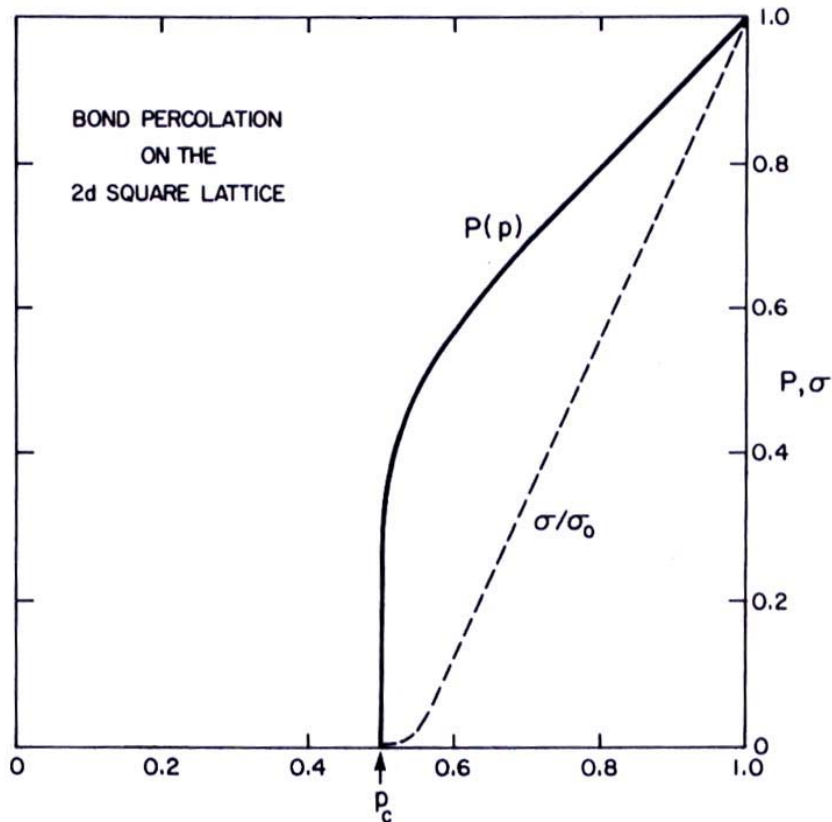
Figure 1.5 The behavior, as a function of fraction (*p*) of filled bonds, of key properties (percolation probability P (*p*) and random-network conductivity σ) that characterize bond percolation on the square lattice in two dimensions [41]
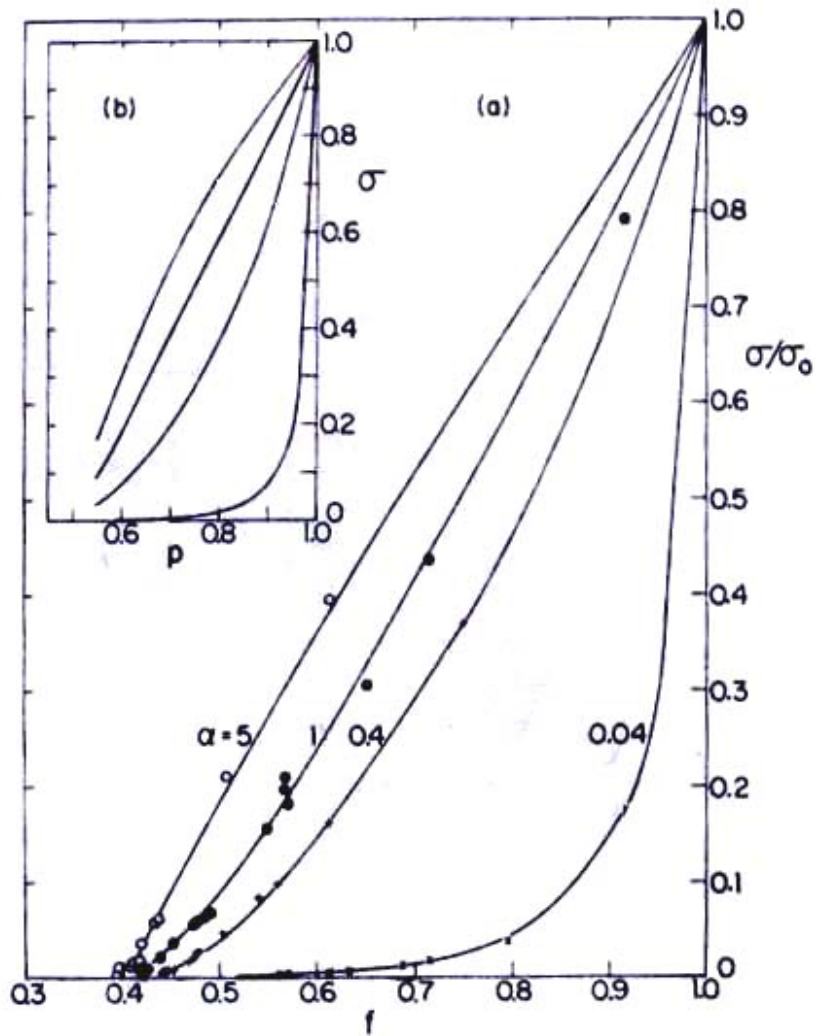
Figure 1.6 (a) Normalized conductivity vs. metal area fraction (b) Results of Monte Carlo calculations on a square lattice with the same degrees of anisotropy as the data (a)[45]

All these effects of intrinsic attributes and extrinsic factors on thermal conductivity will be investigated in this dissertation. The effect of intrinsic attributes will be examined for the coatings made of a variety of materials. The above-mentioned methods and theoretical strategies will be used to explore the extrinsic effects in the following research.

References

1. L. Pawlowski and P. Fauchais, Thermal transport properties of thermally sprayed coatings, *International Materials Reviews*, Vol. 37, No.6, 1992, p. 271-290.

2. K. W. Schlichting, N. P. Padture and P. G. Klemens, Thermal conductivity of dense and porous yttria-stabilized zirconia, *Journal of Materials Science*, Vol. 36, No.12, 2001, p. 3003-3010.

3. A. Kulkarni, Z. Wang, T. Nakamura, S. Sampath, A. Goland, H. Herman, J. Allen, J. Ilavsky, G. Long, J. Frahm and R. W. Steinbrech, Comprehensive microstructural characterization and predictive property modeling of plasma-sprayed zirconia coatings, *Acta Materialia*, Vol. 51, No.9, 2003, p. 2457-2475.

4. D. R. Clarke and C. G. Levi, Materials design for the next generation thermal barrier coatings, *Annual Review of Materials Research*, Vol. 33, 2003, p. 383-417.

5. A. L. Loeb, Thermal Conductivity .8. A Theory of Thermal Conductivity of Porous Materials, *Journal of the American Ceramic Society*, Vol. 37, No.2, 1954, p. 96-99.

6. Z. Wang, A. Kulkarni, S. Deshpande, T. Nakamura and H. Herman, Effects of pores and interfaces on effective properties of plasma sprayed zirconia coatings, *Acta Materialia*, Vol. 51, No.18, 2003, p. 5319-5334.

7. V. Debout, A. Vardelle, P. Abelard, P. Fauchais, E. Meillot, E. Bruneton, S. Schelz and N. Branland, Optical Properties of Yttria-Stabilized Zirconia Plasma-Sprayed Coatings, *Proceedings of the 2006 International Thermal Spray Conference,Seattle,WA,USA*, 2006.

8. S. Deshpande, S. Sampath and H. Zhang, Mechanisms of oxidation and its role in microstructural evolution of metallic thermal spray coatings - Case study for Ni-Al, *Surface & Coatings Technology*, Vol. 200, No.18-19, 2006, p. 5395-5406.

9. R. Mcpherson, A Model for the Thermal-Conductivity of Plasma-Sprayed Ceramic Coatings, *Thin Solid Films*, Vol. 112, No.1, 1984, p. 89-95.

10. D. B. Fowler, W. Riggs and J. C. Russ, Inspecting Thermal Sprayed Coatings, *Adv. Mater. Process.*, Vol. 11, 1990, p. 41–52.

11. O. Lavigne, Y. Renollet, M. Poulain, C. Rio, P. Moretto, P. Brannvall and J. Wigren, Microstructural characterization of plasma sprayed thermal barrier coatings by quantitative image analysis, *Quantitative microscopy of high temperature materials conference, Sheffield, UK*, 1999.

12.　　K. Mailhot, F. Gitzhofer and M. I. Boulos, Absolute coating porosity measurement using image analysis, *Proceedings of the 15th ITSC, Nice, France, 1*, 1998, p. 917–922.

13.　　S. T. Bluni and A. R. Marder, The use of quantitative image analysis for the characterization of a thermal spray coating, *Proceedings of the 4th NTSC, Pittsburgh, PA*, 1991, p. 89-96.

14.　　B. Schorr, K. Stein and A. Marder, Characterization of thermal spray coatings, *Mater. Charact.*, Vol. 42, 1999, p. 93–100.

15.　　Y. Zhu, H. Liao, C. Coddet and B. Xu, Characterization via image analysis of cross-over trajectories and inhomogeneity in twin-wire arc spraying, *Surf. Coat. Technol.*, Vol. 162, 2003, p. 301–308.

16.　　K. Markov and L. Preziosi, Heterogeneous media: micromechanics modeling methods and simulations, c/o Springer-Verlag New York, Inc, Birkhäuser Boston, 1999.

17.　　M. Kaviany, Principles of heat transfer in porous media (2nd ed.), *Springer-verlag New York Inc*, 1995.

18.　　F. Kroupa and M. Kachanov, Effect of microcracks and pores on the elastic properties of plasma sprayed materials. In:, 1998, p. 325–330.

19.　　I. Sevostianov and M. Kachanov, Modeling of the anisotropic elastic properties of plasma-sprayed coatings in relation to their microstructure, *Acta Mater*, Vol. 48, 2000, p. 1361–1370.

20.　　S.H. Leigh and C.C. Berndt, Modelling of elastic constants of plasma spray deposits with ellipsoid-shaped voids, *Acta. Mater.* , Vol. 47, 1999, p. 1575–1586.

21.　　S.H. Leigh and C.C. Berndt, Quantitative evaluation of void distributions within a plasma-sprayed ceramic, *J. Am. Ceramic. Soc.*, Vol. 82, No.1, 1999, p. 17–21.

22.　　Y. H. Zhao, G. P. Tandon and G. J. Weng, Elastic Moduli for a Class of Porous Materials, *Acta Mech*, Vol. 76, 1989, p. 105–130.

23.　　Y. H. Zhao and G. J. Weng, Effective Elastic Moduli of Ribbon-Reinforced Composites, *J. Appl. Mech., Trans ASME*, Vol. 57, No.1, 1990, p. 158–167.

24.　　J. Argyris, I. S. Doltsinis, M. Eggers and R. Handel, Studies on Ceramic Coatings, Deduction of Mechanical and Thermal Properties from the Microstructure of the Material, *Comput Methods Appl Mech Eng*, Vol. 111, No.203–234, 1994.

25.　　M. Kachanov, I. Tsukrov and B. Shafiro, Elastic solids with many cracks: a simple method of analysis, *Int J Solids Struct*, Vol. 23, 1987, p. 23–43.

26.   M. Kachanov, I. Tsukrov and B. Shafiro, Effective Moduli of Solids with Cavities of Various Shapes, *Appl. Mech. Rev.*, Vol. 47, 1994, p. 151–174.

27.   T. Nakamura, G. Qian and C. C. Berndt, Effects of pores on mechanical properties of plasma-sprayed ceramic coatings, *J Am Ceramic Soc.*, Vol. 83, No.3, 2000, p. 578–584.

28.   Z. Hashin, The differential scheme and its application to cracked materials, *J. Mech. Phys. Solids.*, Vol. 36, 1988, p. 719–734.

29.   R.M. Christensen, A critical evaluation for a class of micromechanical models, *J. Mech. Phys. Solids.* , Vol. 38, 1990, p. 379–404.

30.   S. Deshpande, A. Kulkarni, S. Sampath and H. Herman, Application of image analysis for characterization of porosity in thermal spray coatings and correlation with small angle neutron scattering, *Surface & Coatings Technology*, Vol. 187, No.1, 2004, p. 6-16.

31.   A. Kulkarni, A. Vaidya, A. Goland, S. Sampath and H. Herman, Processing effects on porosity-property correlations in plasma sprayed yttria-stabilized zirconia coatings, *Materials Science and Engineering a-Structural Materials Properties Microstructure and Processing*, Vol. 359, No.1-2, 2003, p. 100-111.

32.   A. Kulkarni, S. Sampath, A. Goland, H. Herman and B. Dowd, Computed microtomography studies to characterize microstructure-property correlations in thermal sprayed alumina deposits, *Scripta Materialia*, Vol. 43, No.5, 2000, p. 471-476.

33.   D. C. Copley, J. W. Eberhard and G. A. Mohr, Computed Tomography Part I: Introduction and Industrial Applications, *JOM*, 1994, p. 14-26.

34.   ASM-Handbook, Nondestructive Evaluation and Quality Control, Materials Park, Ohio: ASM, Vol. 17, 1992, p. 358.

35.   S. L. Wellington and H. J. Vinegar, X-ray Computerized Tomography, *J. Petro. Technol.*, 1987, p. 885.

36.   B. P. Flannery, H. W. Deckman, W. G. Roberge and K. L. D'Amico, Three-Dimensional X-ray Tomography, *Science*, Vol. 237, 1987, p. 1439.

37.   B. A. Dowd, A. B. Andrews, R. B. Marr, D. P. Siddons, K. W. Jones and A. M. Peskin, Advances in X-ray Computed microtomography at the NSLS, *Advances in x-ray analysis*, Vol. 42, 1999.

38.   J. Ilavsky, G. G. Long, A. J. Allen, H. Herman and C. C. Berndt, Use of small-angle neutron scattering for the characterization of anisotropic structures produced by thermal spraying, *Ceramics-Silikaty*, Vol. 42, No.3, 1998, p. 81-89.

39.   A. J. Allen, J. Ilavsky, G. G. Long, J. S. Wallace, C. C. Berndt and H. Herman, Microstructural characterization of yttria-stabilized zirconia plasma-sprayed deposits using multiple small-angle neutron scattering, *Acta Materialia*, Vol. 49, No.9, 2001, p. 1661-1675.

40.   J. M. Hammersley, Percolation Processes - Lower Bounds for the Critical Probability, *Annals of Mathematical Statistics*, Vol. 28, No.3, 1957, p. 790-795.

41.   R. Zallen, *The physics of amorphous solids* 1998: New York : Wiley.

42.   C. J. Lobb, M. Tinkham and W. J. Skocpol, Percolation in Inhomogeneous Superconducting Composite Wires, *Solid State Communications*, Vol. 27, No.12, 1978, p. 1273-1275.

43.   M. Tinkham, in Electrical Transport and Optical Properties of Inhomogeneous Media, *AIP Conference Proceeding*, Vol. 40, 1978, p. 130.

44.   J. Bernasconi, Real-Space Renormalization of Bond-Disordered Conductance Lattices, *Physical Review B*, Vol. 18, No.5, 1978, p. 2185-2191.

45.   L. N. Smith and C. J. Lobb, Percolation in 2-Dimensional Conductor-Insulator Networks with Controllable Anisotropy, *Physical Review B*, Vol. 20, No.9, 1979, p. 3653-3658.

46.   D. Deptuck, J. P. Harrison and P. Zawadzki, Measurement of Elasticity and Conductivity of a 3-Dimensional Percolation System, *Physical Review Letters*, Vol. 54, No.9, 1985, p. 913-916.

Chapter 2.

Statements of the Problem

Thermally sprayed coatings are known to be structurally complex due to the stochastic nature of coating build-up process. The continuous impact of melted and semi-melted droplets during the spraying process produces an anisotropic layered arrangement of microstructural defects (pores, cracks, etc.) in the coating and brings on a significant effect on thermal transport property. The understanding of the relationships between the microstructural defects and properties are essential to tailor and control properties of thermally sprayed coatings. However, the complexities of the microstructures arising from the spraying processing which involves a large number of interrelated variables make it difficult to establish microstructure–property relationships. Furthermore, the dynamic evolution of microstructure and property during service offer additional challenges to microstructural characterization as well as the life prediction. Establishing the structure-property relationships is also dependent on the understanding for the nature of sprayed materials. In addition, the applicability and repeatability of the techniques for thermal conductivity measurements have a significant effect on the fidelity of the obtained results and thus the reliable description of microstructure-property relationships. The continued advancements are necessary in microstructural characterizations, material assessments, property measurements and process technologies as well as the life prediction capabilities.

Investigation presented in this dissertation focuses on developing the characterization of coating microstructure while concurrently examining thermal conductivity of thermally sprayed coatings at both room temperature and high temperature for a range of thermal spray material systems. The principal goals include understanding the anisotropic nature of coatings, examining the effect of annealing on thermal conductivity, and assessing the techniques for thermal conductivity measurements. The following specific issues are considered.

Effective Porosity

The microstructures of plasma sprayed YSZ coatings include different morphological defects such as globular pores, interlamellar pores, and cracks. Quantitative microstructure characterization seeking to better understand microstructure-property relationships is of considerable interest in plasma sprayed coating research. There have been many studies aimed at understanding the effect of these microstructural defects, porosity in particular, on the thermal conductivity of plasma sprayed YSZ

coatings. Some early research has related the effective conductivity of the porous materials to total porosity. However, total porosity does not fully capture the anisotropic pore features and associated abnormal variations of the thermal transport property with total porosity. Recent development of microstructure characterization promotes the qualitative and quantitative investigation of microstructural features (surface area, porosity, pore morphology and orientation) as well as the relationship of each microstructural feature to thermal transport property. The important role of interlamellar porosity in both room temperature and temperature dependent thermal conductivity was pointed out and the effective contribution of different morphology pores on thermal conductivity was also investigated. Despite all these efforts regarding porosity, the variation of the thermal conductivity still needs to be interpreted from many aspects, such as the morphology and amount of pores, which brings out the difficulty of establishing microstructure-property relationships. There appears to be no unified, yet practical, parameter that is suitable to be used to characterize microstructural defects just as a second phase regardless of their geometry features to determine the effects on thermal physical properties. It becomes necessary to determine or establish such a microstructural parameter. In this dissertation, all the various morphology porosities are unified to one single microstructural parameter named "effective porosity" for better understanding of microstructure-thermal transport property relationships according to the heat resistance principle since all the different morphology pores play the role as a second phase in essence.

High Temperature Thermal Conductivity

Past studies have focused on microstructure-room temperature thermal conductivity relationships. However, the application temperatures of YSZ coatings used as thermal barrier coatings (TBCs) are well above 1000°C. The distinctions in microstructure and the high temperature thermal conductivity of the coatings up to the desired engine operational temperatures are needed to be examined. At such high temperatures the photon conduction becomes increasingly important due to the increase of the radiation contribution. The radiation experiences the absorption, reflection, refraction and transmission when it proceeds from the coatings. Working in collaboration with the Oak Ridge National Laboratory (ORNL) on high temperature thermal conductivity measurements and detailed investigations were carried out for TBCs with a range of starting microstructures.

Materials

Thermal conductivity of thermally sprayed coatings is also composition dependent. For metallic coatings, the electron mechanism of heat transport plays the dominant role since electrons are not as easily scattered as phonons and have higher velocity. The atomic radius, atomic weight, electron drift mobility, electron concentration and valence electrons all affect the thermal conductivity. Another important aspect of thermally sprayed metallic coatings is the oxidation generated from the spraying process. The oxidation results in more complexity of the variations of thermal transport property for different material coatings. The introduced atoms other than host atom act as impurities, distort the crystal lattice, scatter the electron motion and decrease the conductivity. A

range of dependent factors of thermal conductivity need to be studied and it is essential to distinguish the dominant ones for various material systems.

Anisotropy

The splat-based layered microstructure causes anisotropy of the coating. Thus, the microstructural anisotropy of thermally sprayed coatings gives rise to the anisotropy of property. Few theoretical techniques are available for dealing with severely disordered systems and anisotropic situations. Percolation theory provides a well defined, transparent and intuitively satisfying model for spatially random processes. Percolation theory has been successfully applied to the studies for the anisotropy of electrical conductivity, elastic modulus and so on. However, limited scientific literature focuses on the introduction of the percolation concepts to the investigation for the anisotropy of thermal conductivity. The theoretical treatment for the anisotropy of thermal conductivity is carried out by using percolation concepts toward an understanding of the processing-microstructure-property relationships for thermally sprayed coatings in this study.

Annealing Effects

YSZ coatings, are designed as thermal barrier coatings (TBCs) to protect the components from the harsh and severe thermal environment notably in gas turbine engines, increase the operating temperature with consequent improvements in efficiency, and prolong the component durability and life extension. The thermally sprayed coatings have much lower thermal conductivity than the bulk material with the same composition due to the contribution of the pores. It is well known though the pores are prone to high temperature sintering which can reduce or even eliminate the conductivity reduction benefit. This failure of the TBCs mainly results from two factors: a time-at-temperature component and a cycle-frequency component. Both components give rise to significant microstructural changes and thus the thermal conductivity variations. Substantive studies simulating the mechanical system in operation have been performed to understand the effects of these two components on coating microstructure and properties. It was found that both components contribute to improve the splats contact and result in the closure of interlamellar pores, which elevates thermal conductivity of TBCs. Unfortunately, quantitative investigation of the relationship between thermal conductivity and microstructural defects for TBCs before and after annealing is still limited. So, many questions need to be answered.

Thermal Conductivity Measurements

Aside from its importance as a design parameter for thermally sprayed coatings, measuring thermal conductivity of thermally sprayed coatings itself provides a unique method to critically characterize the nature, quantity and anisotropy of the defect morphologies in these splat-based coatings. Development of precise and reliable measurement methods is an important step in the study of the thermal transport property of inherently complex coatings. The flash methods of measuring thermal conductivity remove the steady-state condition at the expense of measuring temperature as a function of time and avoid the error arising from non-realization of the steady-state conditions. Laser flash technique had been proved to be the most accurate and fastest way of determining thermal conductivity of coatings. A complex laser flash system may not

always be required for the routine measurement. The xenon flash technique, an alternate approach to characterization of the thermal transport property, has been developed recently in ORNL. The comparison of the applicability and repeatability of the laser and xenon flash techniques is carried out for coatings in which either phonons or electrons are the predominant heat transporters in order to obtain reliable and accurate thermal conductivities to optimize design and assure the safe operation of turbine engines.

Summary of Proposed Strategy:

This dissertation seeks to address the problems outlined in the above section through a comprehensive examination for the intrinsic and extrinsic effects on thermal conductivity of thermally sprayed coatings. This is vitally important for future incorporation of thermal spray coatings into design.

The results are synthesized in chapters 4-7, while chapter 8 addresses the measurement issues and reliability for thermal transport in thermal spray coatings. Chapter 4-6 critically examine the extrinsic effects on coating thermal conductivity, such as microstructural defects, thermal aging, oxidation, etc through an integrated study of yttria-stabilized zirconia thermal barrier coatings. A wide range of experimental explorations of the quantitative characterization for coating microstructure are carried out in an effort to establish porosity-thermal conductivity maps. Specifically, this dissertation complements and expands past work in this area, through carefully separating processing effects, conducting measurements at relevant temperatures of interest and synthesizing all of the results within the context of 2nd order process maps. Finally, new methods of quantitative microstructural definition based on *effective porosity* are proposed to capture the weighted contribution of interfaces, which enable better understanding of microstructural defects - thermal conductivity relationship. Percolation theory is applied to interpreting the change of anisotropy for thermal conductivity with porosity and predicting microstructure-thermal conductivity relationship.

Chapter 6 examines thermal transport in defected metallic and alloy coatings produced via thermal spray. Although the thermal transport is not of direct industrial relevance to many of these coatings (at least as of now), new phenomena such as oxidation, vacancies and impurity effects can be studied. Such systems will allow simultaneous examination of both intrinsic effects on process on the material as well as on extrinsic morphological defects on thermal transport. A careful set of elemental metals and alloys have been selected and subjected to wide ranging process conditions. New insights into process induced chemical and microstructural changes are demonstrated through this integrated investigation.

Finally, in the future work section, several new ideas are discussed that are worthy of future consideration. They include microstructural gradients through thickness, relationship between electrical and thermal conductivities for sprayed metals and transport measurement in multilayer coatings.

This dissertation, perhaps the first time performs a comprehensive assault on the thermal transport problem in complex heterogeneous coatings. The outcome is not only important for the specific area of interest (i.e. thermal spray coatings) but for materials science of complex systems.

Chapter 3.

Materials and Experimental Methods

To understand the effect of materials, processing and microstructure on the thermal transport property, the microstructure and thermal transport property are assessed for thermally sprayed coatings made of a range of materials, such as YSZ, Al_2O_3, semiconductor, single element metals, Ni and Co based alloys, cermets, FGMs. The techniques for microstructural characterization and thermal conductivity measurement used in this dissertation are discussed below in details.

3.1. Techniques for Microstructural Charaterization

3.1.1 Image Analysis

Various methods are employed for quantitative measurement of porosity, which form an important and integral part of microstructural characterization of thermally sprayed coatings. Studies have been conducted here to establish image analysis (IA) as an efficient method for the characterization of porosity in thermally sprayed coatings.

The characterizations of microstructure using image analysis require reliable and reproducible cross-sectional images and also are dependent on image acquisition conditions and threshold selection for porosity. In other words, the key element of the image analysis approach is to identify and model the realistic microstructural images [1]. The Matlab program is designed to read pixels from this image file and group them according to their colors or grayscale levels. In this case, by setting threshold pixel value, two groups are obtained: the pores and the matrix material, respectively. The threshold pixel value should be selected carefully in order that chosen pixel groups closely match the actual distribution of pores. Conversion of the gray scale image into a binary image is fulfilled by using two filters of different size to compare each pixel of the gray scale image in the middle of the filter with the mean value of the pixels covered by the filter. The middle pixel appears black if darker and white if brighter than the mean value of the neighboring pixels. It is easier to use the smaller filter to detect small-scale features and therefore all details but bring on a great deal of noise. The larger filter is able to remove the noise at the expense of missing some details. A combination of the smaller and larger filters can achieve a final binary image containing all details of the defects and no noise[2].

The total pores can be categorized into globular and interlamellar pores using Matlab. The procedure is shown in Fig. 3.1. The threshold value is chosen in a region

where a small variation of that value generates large variations of the porosity and the gray scale (0-255 gray scales) image (Fig. 3.1 (a)) are converted into a binary image (Fig. 3.1 (b)). The binary image gives an indication of the total priority and is used to obtain average of porosity. Based on aspect ratio and direction, in Fig. 3.1 (c), the total pores are categorized into interlamellar pores (aspect ratio less than 1/6, angle between this pore and horizontal line less than 45°) and globular pores (all the others). The interlamellar pores are subtracted to yield the image for the crack network (Fig. 3.1 (d)).

The component porosity and total porosity are calculated by the Matlab program, shown in Fig. 3.2. It can be seen that globular pores contribute larger percentage of the total porosity. The interlamellar pores have lower contribution to total porosity but they are the main reason for anisotropy.

Fig. 3.3 shows how the cumulative mean of total porosity evens out for 40 images of the cross-sections of a YSZ coating. 40 porosities were obtained by image analysis. Then, the first porosity was associated with number 1, the average of the first and second porosity was associated with number 2, and the average of the first, second and third porosity was associated with number 3 and so on. Fig. 3.3(a) is the evolution of the cumulative mean value of total porosity for 200x (1315×1013 pixels) images of the YSZ coating and Fig. 3.3 (b) is for 500x (1315×1013 pixels) images.

(a)   (b)

(c)   (d)
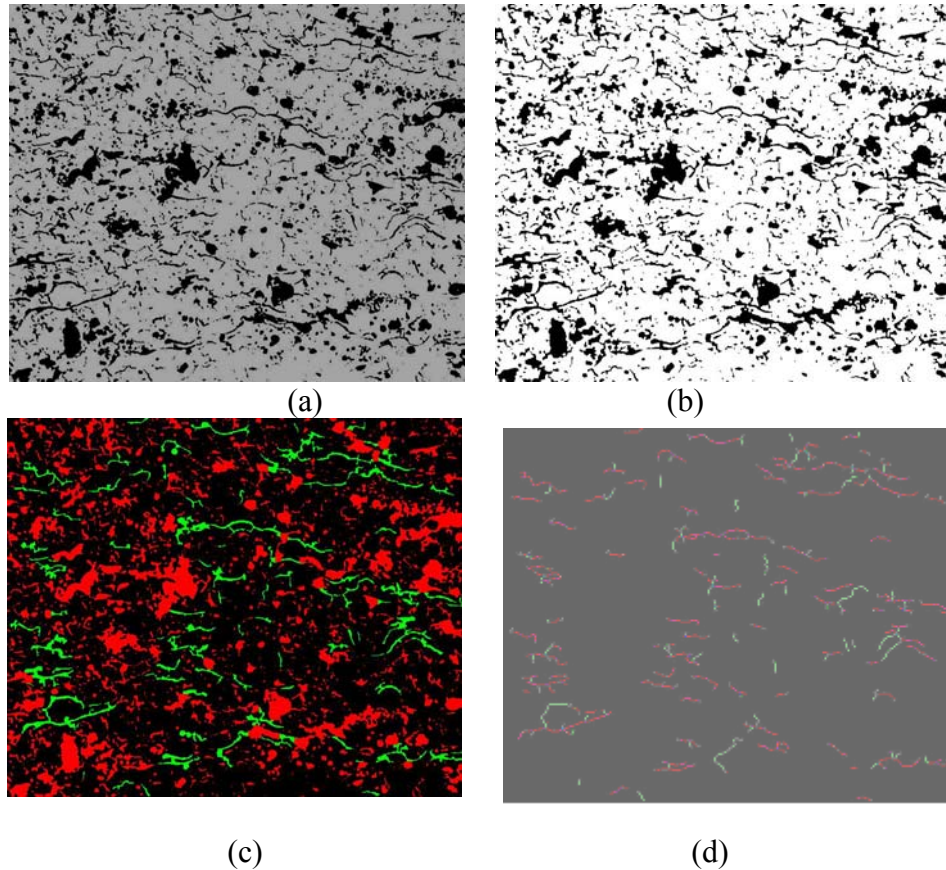
Figure 3.1   Image analysis procedure for separating microstructural void features

(a) gray image (b) binary image (c) separation of pore and crack (d) crack network
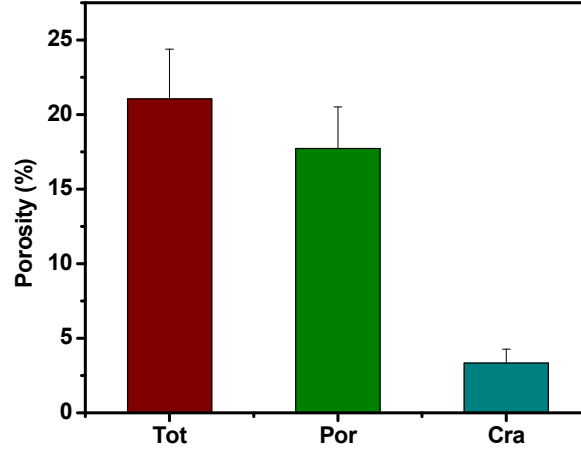
Figure 3.2 Component porosity and total porosity of optical images determined by IA

(a)

(b)
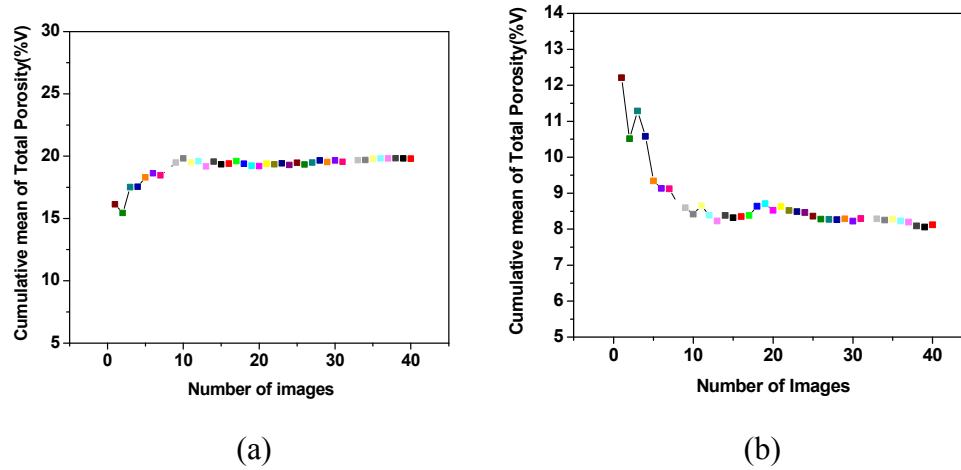
Figure 3.3 Cumulative mean porosity of coatings determined by image analysis

(a) 200x (b) 500x

Cumulative mean porosity changes little after number 20 for both 200x and 500x images. Hence, 20 points are sufficient for a measurement, which is followed for other samples. The images taken at 200x image magnification produce higher porosity that the images taken at 500x image magnification using IA for the same coating. The reason is that the optical images taken at 500x image magnification have bad quality and appear blurred. Therefore, some information of microstructural defects can not be detected in the images. In this dissertation, all the optical image magnification is 200.

3. 1. 2. Archimedes' Method

To achieve reliable results, image analysis is complemented with the Archimedes's method. Four YSZ coatings (No. 1-4) made of HOSP powder at constant temperature and velocity were analyzed to acquire total porosity, globular porosity and interlamellar porosity using IA (Fig. 3.4(a)) whereas the open porosity, closed porosity and total porosity by using Archimedes' method (Fig. 3.4(b)). From Fig. 3.4(a), it is observed that the YSZ coatings include more globular pores than interlamellar pores. From Fig. 3.4(b), it is found that the pores mainly are open pores in the YSZ coatings.

The whole procedure of Archimedes' method is economical and simple in operation. Firstly, the freestanding coating is immersed into water. Secondly, the water is heated to boil for 3h. After cooling down, the coating is measured for 3 weights: the weight of the coating in water (m_2), the wet weight (m_3) and the dry weight (m_1). Finally, porosity and density are calculated using the formulas as below:

Open porosity $P_{open} = (m_3 - m_1)/(m_3 - m_2)$
Density $D = m_1/(m_3 - m_2)$
Total porosity $P_{total} = 1 - D/D_{theory}$
Closed porosity $P_{closed} = P_{total} - P_{open}$

(a)   (b)
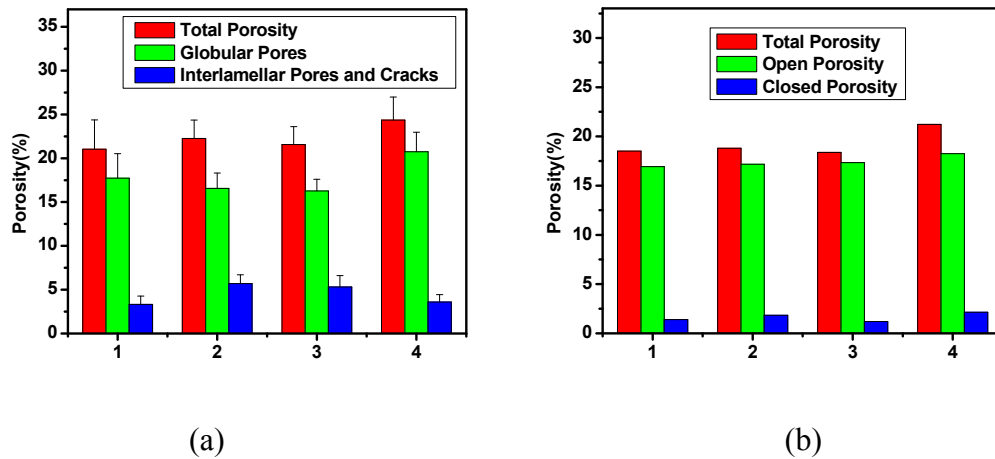
Figure 3.4 Porosities of YSZ coatings obtained by different methods

(a) Image analysis (b) Archimedes's method

3.1.3. Precision Density Method

The method, precision density method, is one of the easiest methods for total porosity measurement. The sample dimension and weight are measured to calculate porosity with known parameter - theoretical density. Fig. 3.5 shows the comparison of the total porosity obtained by IA, Archimedes' method and precision density method for 4 YSZ samples. The total porosity values obtained by these different methods are close for the same sample and the trends in variation of total porosity for different samples are in

agreement. However, the porosity detected by Archimedes's method is in general 3% lower than that detected by image analysis because metallographic preparation enlarges fine cracks and generates pullouts that have a crack network associated with them, which also gets counted through image analysis. As such, image analysis overestimates the volume of pores, although the microcracks within splats are invisible to image analysis [3]. However, the method of image analysis provides a means to quantify different features of the microstructure. The porosity obtained by Archimedes' method is about 1% lower than obtained by precision density method due to incomplete saturation of water to pores.
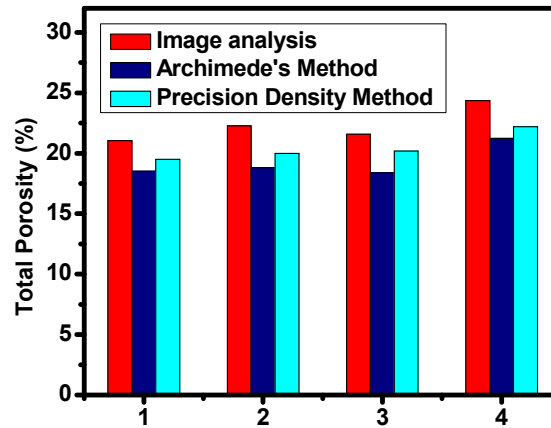
Figure 3.5 Comparison of porosity obtained by three different methods

3.1.4 Pycnometer

Gas pycnometry is based on Boyle-Mariotte's law of volume pressure relationships. The Micro-Ultrapycnometer is specifically designed to measure the volume and true density of solid materials, which consists of a sample chamber with a screw cap, a tank and an absolute pressure transducer. The Archimedes' principle of fluid displacement is employed to determine the volume. The helium gas is adopted as the displaced fluid due to its small atomic dimensions and thus it is easier to penetrate the finest pores (approaching one Angstrom) and achieve maximum accuracy. In addition, the gas pyconometer provides the chance to measure the volume of substances that react chemically or physicochemically with liquid, such as water. But there are some fundamental hypotheses for gas pyconometer:

(1) ideal gas behavior
 (2) rigid sample and pycnometer
 (3) fast speed for expanding gas to reach a static equilibrium.
This method can be used to complement other methods and attain reliable measurements for porosity as Archimedes's method.

3.1.5 MIP

Mercury intrusion porosimeter is a commonly used technique for measuring the pore structure, such as pore size in a range from about 400 to 0.007 μ m and pore volume. An external pressure is applied for wetting the pore surface in MIP. The intrusion of mercury into the material is the function of pressure. The MIP instrument can fulfill both low pressure and high pressure measurements. The range of low pressure for Poremaster-33 is 3.5-350kPa (0.5-50psi) and the low pressure measurement is used for the pores with diameter 400-4.3 μ m. The range of high pressure for Poremaster-33 is 140kPa-230MPa (20-33000psi) and the low pressure measurement is suitable for the pores smaller than 4.3μ m.

MIP can acquire different microstructural parameters for thermally sprayed coatings, i.e. surface area, density, porosity, pore size distribution and tortuosity.
(1) For a cylindrical pore of radius r and length L, r is related to the pressure P by the Washburn equation,

$$r = 2\gamma \cos(\theta)/P$$

where γ is the surface tension (400~550 ergs/cm^2,usually 480 ergs/cm^2) and θ is the contact angle (between 90.01° and 179.99°). The Washburn equation indicates that when the pressure goes up, the mercury will intrude into narrow pores.

(2) The surface area of pores filled up to pressure P is given by:

$$s = \frac{1}{\gamma|\cos\theta|}\int_0^V PdV$$

(3) The bulk density ρ is defined as the sample density determined by the volume of mercury displaced at fill pressure. The porosity can be calculated according to the density:

$$p = 1 - \frac{\rho}{\rho_{theory}}$$

MIP can only measure open porosity with precision since the mercury has inability to penetrate closed porosity.
(4) The volume pore size distribution Dv(r) is defined as the pore volume per unit interval of radius. It can be represented by:

$$Dv(r) = \frac{P}{r}\frac{dV}{dP}$$

(5) For porous materials, the effective diffusivity D$_{eff}$ differs from the theoretical diffusivity D$_b$ by a structural factor τ as below:

$$D_{eff} = \frac{D_b\theta_c}{\tau}$$

where θ c is the pore volume fraction and τ is the tortuosity factor.
The generalized form of tortuosity factor is:

$$\tau = (2.23 - 1.13V_{co}\rho_{Hg})(0.92y)^{1+E}$$

where:

$$y = \frac{4}{S}\Sigma\frac{\Delta Vi}{di}$$

S-total surface area
ΔVi-change in pore volume within a pore size interval
Di - average diameter within a pore size interval
Vco -volume intruded at the maximum experimental pressure attained
ρ_{Hg}-bulk density
E-pore shape exponent (1 for cylinder)

Mercury is a dangerous and poisonous material. It can be absorbed through the skin, so direct contact should be avoided. If not handled properly, mercury may cause skin, eye and intestinal tract irritation, as well as central nervous system effects. So, mercury must be stored in closed containers or under oil to control its evaporation, and should be used only in well-ventilated rooms to avoid prolonged exposure to mercury vapor. Liquid nitrogen is required to prevent any mercury vapors from contaminating the system.
Despite its wide application, the MIP suffers from some disadvantages. The pore size measured is that of the smallest constriction in a pore and not the average radius. This can give rise to incorrect analysis of pressure-volume data, especially when the pore shape is change (such as sintering). The contact angle is also uncertain. In addition, the high pressures can lead to significant sample compression effects/errors.

3.2. Techniques for Thermal Conductivity Measurement

Aside from its importance as a design parameter for coatings, the measurement of the thermal transport property of thermally sprayed coatings itself provides a challenge given the complex architecture of defects and interfaces in the system. Significant attention has been directed increasingly towards characterizing, understanding and controlling the thermal transport property. Laser radiation has some unique properties: monochromaticity, coherence, small angular divergences and high radiation densities. These unique properties provide some special applications of laser. Since its introduction in 1961[4], the laser flash technique has become a standard testing method for the thermal transport property measurements of solids [5, 6]. The laser pulse is less than 1 millisecond using for thermal conductivity measurements. Regular thermal conductivity measurement requires the specimen to be opaque to both wavelengths of the laser pulse and the infrared detector (3 to 5μm) [7]. The TBC materials which will be studied in this work are typically translucent. Therefore, the conventional treatment is to put opaque graphite coating on both sides in order to enhance the absorption of laser energy and the emission of IR radiation to the detector. The graphite coating greatly increases the resulting signal-to-noise ratio. The specific heat measurement also requires that the reference sample and the test samples have a graphite coating with the same absorption and emittance. All the laser energy is absorbed at the front surface and the IR detector measures thermal radiation of the rear surface. The front and rear surface temperatures of 300μm-thick or thinner TBCs having low thermal conductivity will increase much more than those of thicker samples having moderate thermal conductivity after the fired shot of laser pulse. The excessive temperature increase could drive the IR detector into a nonlinear temperature-voltage response and thereby cause significant errors in the measured conductivity values. Therefore, the laser power level should be large enough to

obtain good signal-to-noise ratios, yet not result in excessive rear surface temperature rises (i.e., $\Delta T > 5^oC$).

A complex laser flash system may not always be required for the routine measurement. The xenon flash technique, an alternate approach to characterization of the thermal transport property, has been developed recently in Oak Ridge National Laboratory (ORNL). Detector signal monitoring, data acquisition and analysis are integrated into one executable program [8]. The low energy of the xenon pulse (12 Joule) is also favorable for reducing the temperature increase of the front and rear surfaces. Three flash systems will be introduced in details below and adopted to explore the thermal conductivities of a variety of thermally sprayed coatings in this dissertation.

3.2.1 Xenon Flash Thermal Diffusivity (XFTD) System

Reliable measurement of thermal diffusivity in many cases can be obtained through the xenon flash technique. The Room Temperature Xenon Flash Thermal Diffusivity (XFTD) System was designed using a high power flash lamp, an InSb IR detector and a computer (Fig. 3.6).The pulse energy is 12 Joule and the pulse time is 6~8ms. The excitation wavelength is not a simple number since the xenon pulse is not monochromatic light. It is calculated using the field of view (or solid angle) to view 0.8 cm diameter area of the sample to maximize the signal. Xenon flash thermal diffusivity system is optimized for room-temperature thermal diffusivity measurements of ceramics, metals, composites, and coatings. However, this system can not be used to measure thermal conductivity directly. A separate Differential Scanning Calorimeter (DSC) system is necessary to measure Cp in order to calculate thermal conductivity and its accuracy is about 1-2% [9]. The formula for thermal conductivity calculation is $K=\alpha\rho Cp$, where K is the thermal conductivity, ρ is the bulk density and Cp is the specific heat. The accuracy of XFTD is somewhat better than that of laser flash instrument due to higher signal to noise ratio [8]. (Details in Chapter 4).
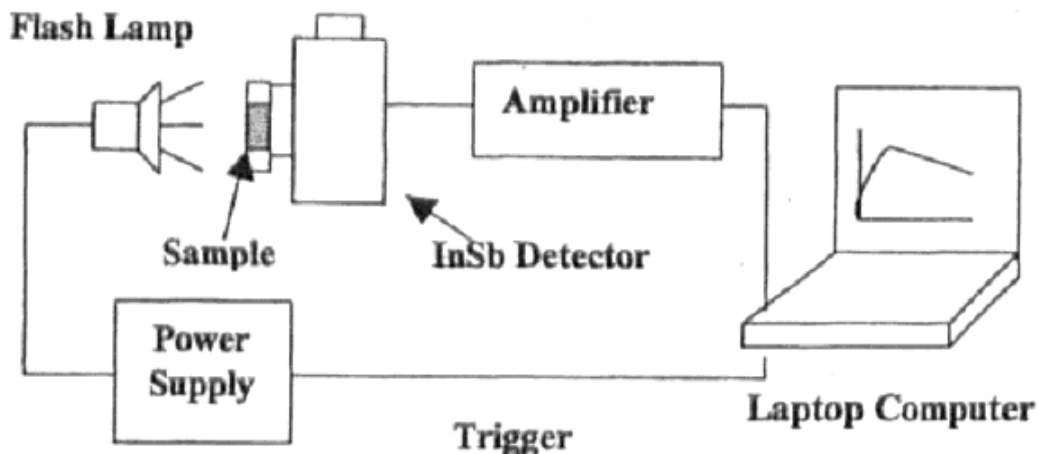
Figure 3.6 Set-up of room temperature xenon flash diffusivity system [8]

3.2.2 Laser Flash Instrument for Room Temperature (RT)

Holometrix laser flash instrument (HLF) can be used to measure both thermal diffusivity and thermal conductivity by obtaining Cp and α in one test for metals, coatings, composites, ceramics, and polymers and so on. In the through-thickness measurement, the sample can be as part of a sheet of material infinite in two dimensions but of finite thickness. The measurement of the thermal diffusivity of a material is usually carried out by rapidly heating one side of a sample and measuring the temperature rise curve on the opposite side. The temperature rise of the other side is measured as a function of time using an infrared detector. Before the flash, the temperature of sample and surroundings is at some uniform temperature that can be taken as zero. Immediately after the flash, the front surface of the sample is at some higher temperature. The heat flux lines are parallel and directed through the sample; there is no heat flow in the plane of the sample, as shown in Fig. 3.7(a).

The specific heat is calculated from the same data of temperature rise recorded in thermal diffusivity measurement with a suitable calibration by comparing to the temperature rise of a reference sample of known specific heat. It is assumed that the laser pulse energy and its coupling to the sample remain essentially unchanged between samples.

Laser pulse energy $= (m \cdot Cp \cdot \Delta T)_{ref} = (m \cdot Cp \cdot \Delta T)_{sample}$

and

$$Cp_{sample} = \frac{(mCp\Delta T)_{ref}}{(m\Delta T)_{sample}}$$

With an additional measurement of bulk density, thermal conductivity can be calculated.

The other advantage is that in-plane measurements of thermal diffusivity and conductivity are available. Figure 3.7(b) shows the schematic of in plane laser flash measurement. The laser beam is collimated or focused on the front face of the sample, and the distance that heat must flow is significantly greater. A mask with a circular pinhole concentric with the beam axis is used to define the viewing radius of the IR detector. The radial, in-plane measurement does not constrain the heat flow to one or even two dimensions. The heat flow has two components: one through the sample and one in the plane of sample. Heat that flows directly through the samples will be blocked by the mask [10].
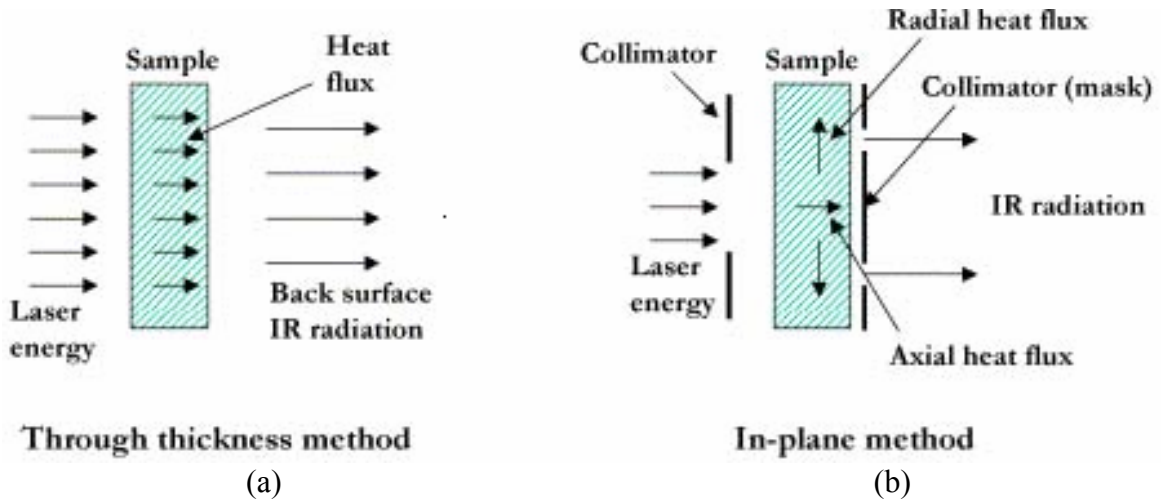
Figure 3.7 Schematics of through plane and in plane laser flash measurement [10]

3.2.3 Laser Flash Thermal Diffusivity (LFTD) System for High Temperature (HT)

The high temperature thermal property can be measured by the Anter Flashline 5000 LFTD system that is designed to acquire data automatically from cryogenic temperatures up to 2500°C. A schematic of the system is shown in Fig. 3.8. The ultra-high temperature graphite furnace is deigned to operate from 500°C to 2500°C in inert gas environment and up to 2000°C in vacuum. It employs a water cooled stainless steel outer shell, molded fibrous carbon insulation, and pyrolitic graphite reflector inside. The temperature of the sample holder is monitored by an optical pyrometer. The operating range of low temperature aluminum furnace is from -150°C to 500°C. It is made out of aluminum and stainless steel and has similar design to the graphite furnace carousel. Thermal couples are used to measure and control furnace temperature.

A small disk-shaped specimen is placed in an evacuated tube furnace and oriented with its flat surfaces perpendicular to the furnace axis. A heat pulse (less than 1 millisecond) is transmitted to the front face of a specimen using a laser flash, and the temperature change of the rear face is measured with an infrared (IR) detector. Data analysis algorithms interpret the rear face temperature response and provide instrumental and specimen dependent corrections. The change of thermal diffusivity with temperature can be obtained by this LFTD system [11].
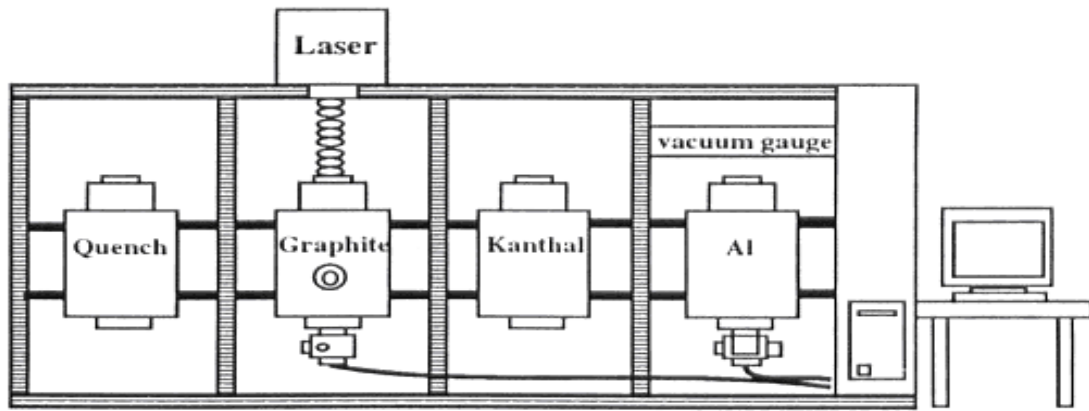
Figure 3.8 Schematic of Anter Flashline 5000 laser flash diffusivity system [11]

References

1.   Z. Wang, A. Kulkarni, S. Deshpande, T. Nakamura and H. Herman, Effects of pores and interfaces on effective properties of plasma sprayed zirconia coatings, *Acta Materialia*, Vol. 51, No.18, 2003, p. 5319-5334.

2.   M. Friis, C. Persson and J. Wigren, Influence of particle in-flight characteristics on the microstructure of atmospheric plasma sprayed yttria stabilized ZrO2, *Surface & Coatings Technology*, Vol. 141, No.2-3, 2001, p. 115-127.

3.   S. Deshpande, A. Kulkarni, S. Sampath and H. Herman, Application of image analysis for characterization of porosity in thermal spray coatings and correlation with small angle neutron scattering, *Surface & Coatings Technology*, Vol. 187, No.1, 2004, p. 6-16.

4.   W. J. Parker, R. J. Jenkins, G. L. Abbott and C. P. Butler, Flash Method of Determining Thermal Diffusivity, Heat Capacity, and Thermal Conductivity, *Journal of Applied Physics*, Vol. 32, No.9, 1961, p. 1679-1684.

5.   R. E. Taylor, Thermal conductivity determinations of thermal barrier coatings, *Materials Science and Engineering a-Structural Materials Properties Microstructure and Processing*, Vol. 245, No.2, 1998, p. 160-167.

6.   L. M. Clark and R. E. Taylor, Radiation Loss in Flash Method for Thermal-Diffusivity, *Journal of Applied Physics*, Vol. 46, No.2, 1975, p. 714-719.

7.   H. Wang and R. B. Dinwiddie, Reliability of laser flash thermal diffusivity measurements of the thermal barrier coatings, *Journal of Thermal Spray Technology*, Vol. 9, No.2, 2000, p. 210-214.

8.   H. Wang and R. B. Dinwiddie, Development of a LabViewTM Based Portable Thermal Diffusivity System, *Thermal Conductivity 27/Thermal Expansion 15* 2004, p. 484-492.

9.   W. Chi, S. Sampath and H. Wang, Ambient and High Temperature Thermal Conductivity of Thermal Sprayed Coatings, *Journal of Thermal Spray Technology*, Vol. 15, No.4, 2006.

10.   A. Kulkarni, J. Gutleber, S. Sampath, A. Goland, W. B. Lindquist, H. Herman, A. J. Allen and B. Dowd, Studies of the microstructure and properties of dense ceramic coatings produced by high-velocity oxygen-fuel combustion spraying, *Materials Science and Engineering a-Structural Materials Properties Microstructure and Processing*, Vol. 369, No.1-2, 2004, p. 124-137.

11.   H. Wang, R. B. Dinwiddie and P. S. GAAL, Multiple Station Thermal Diffusivity Instrument, *Thermal Conductivity 23*, p. 119-126.

Chapter 4.

On The Microstructure-Thermal Conductivity Relationships for Plasma Sprayed Yttria Stabilized Zirconia Coatings

4.1 Introduction:

Yttria stabilized zirconia coatings continue to dominate the application of thermal barrier coatings (TBCs) in gas turbine engines. As TBCs find expanded applicability in both aero and land based gas turbine engines, the requirement for coating reliability and performance have become increasingly stringent. Among the coating processes, plasma spraying of YSZ for TBC application finds wide spread application particularly in land based gas turbine components with large component sizes. Land based gas turbines utilize YSZ TBCs in a significant number of components and are exposed to ever increasing operating temperatures and extended use times before replacement. As such, continued advancements become necessary in TBC materials and process technologies as well as their life predictions capabilities.

It is widely appreciated that the defected microstructure comprising of pores and cracks contribute substantially to the reduced thermal conductivity of YSZ TBC coatings. Clarke and Levi in their review [1] have shown that the typical thermal conductivity of plasma sprayed YSZ coating is of the order of 1 W/m.K which represents only about 40% of the bulk value of thermal conductivity for YSZ (~ 2.5 W/m K). The air plasma sprayed TBC shows a substantially reduced thermal conductivity even compared to its Electron Beam Physical Vapor Deposited (EB-PVD) counterpart (~ 1.6 W/ m K).

Several earlier studies [2-6] have focused on quantitative description of the plasma sprayed YSZ coating and its linkages to process and properties. To delineate the pore morphologies, Ilavsky et al. [2, 3] and Kulkarni et al. [4] have employed multiple small-angle neutron scattering in conjunction with appropriate scattering models of the pore solid interfaces. The application of self consistent models to describe the microstructure has allowed for quantitative definition of the coating into its anisotropic defect contributors namely, interlamellar pores (resulting from splat based layered coating build-up), microcracks (associated with relief of quenching stresses) and globular pores (arising

from lack of complete filling). In a related study, Wang et al.[5] assessed the contribution of the various microstructural features of plasma sprayed YSZ on its room temperature thermal conductivity. They concluded that the pore architecture alone cannot describe the more than 60% reduction in thermal conductivity and the contribution from splat interfaces (from successively formed rapidly quenched and flattened droplets) plays a significant role. Deshpande et al. [6] linked the small-angle neutron scattering data with image analysis based description of the microstructural defects.   Although the absolute values of the determined pore distribution were different, the relative changes between the SANS approach (3D) with the image analysis (2D) tracked in a consistent manner.

These expansive studies have pointed to the continued need for microstructural definition and the interrelationships of the properties with the complex microstructures. Furthermore new developments in process science and control have allowed unprecedented opportunities for tailoring the microstructural sub-components with concomitant possibilities for optimizing thermal conductivity of YSZ TBCs. As alternative materials are envisioned for new generations of TBCs, the requirement of microstructural control of the complex layered, defected plasma sprayed microstructure can transcend to new systems in the future.

This study seeks a successive pathway to the previous efforts and relates to the following two objectives:

- Recent investigations [7-10] in process science has allowed for manipulation and control of the plasma spray particle stream enabling synthesis of coatings with factored microstructures. This is achieved in a number of ways (a) through selection of varying starting powder feedstock morphologies but effectively controlled in the process so as to achieve similar temperature and velocity distribution (b) by careful modification of particle size distributions and (c) through variations in process conditions integrated with sophisticated diagnostic tools (d) the viability of feedback control methods for microstructural controls.
- Past studies [4-6] have focused on microstructure-room temperature thermal conductivity relationships. Here we examine the distinctions in microstructure on the temperature dependent thermal conductivity of the coatings up to and in some cases beyond the desired engine operational temperatures. Furthermore the stability of the starting microstructure to thermal aging is also considered in the context of both room temperature and temperature dependent thermal conductivity.

Ultimately, such studies will provide not only a scientific analysis of the microstructure property relationships in these complex systems, but will enable new opportunities in design and control in industrial applications of the advanced coatings.

4.2 Materials and Experimental Methods:

To achieve the above mentioned objectives, three sets of plasma sprayed YSZ coatings were investigated.

1) The first set comprised of three YSZ powder feedstock morphologies which are prevalent in most industry application specifications. They are described as Fused and Crushed (F&C), Agglomerated and Sintered (A&S) and Plasma Densified Hollow Sphere (HOSP). Each of these materials was processed under individually optimized process conditions through control of the kinetic and thermal parameters of the spray stream (described here as particle temperature and particle velocity). The specific methodology employed for such process control is beyond the scope of this dissertation, but it is notable to mention that each of the powder morphologies achieved nominally the same average temperature and velocity and similar temperature and velocity distributions. This enables clarification of the microstructural distinctions rather than any processing variabilities.

2) The second set comprised of three YSZ powder feedstocks nominally of the same morphologies but with different particle size distributions. Here a single, broad distribution of powder (referred to as *ensemble*) was broken up into a *fine* and *coarse* fractions respectively. The process was optimized for each powder although the temperature and velocity distributions here were different.

3) In the third set, a single powder feedstock was chosen and process parameters were varied to achieve 3 distinct sets of coatings resulting from different average particle temperatures and velocities. The basis of this study was to develop process-microstructure-property relationships through the establishment of process maps. Details of the processing science is provided elsewhere [7, 11-14].

For each set of coatings, detailed characterization of porosity and thermal diffusivity and specific heat measurements were conducted.

4.2.1. Porosity:

Information on porosity was obtained using a variety of methods; including image analysis (IA), precision density, Archimedes' method, pycnometer and mercury intrusion porosimetry (MIP). The image analysis provides a 2D interpretation of microstructural images and the associated classification of pores and cracks. In this case, 20 gray images of each sample were taken at different locations using a Nikon Epiphot 200 optical microscope (200x, 1315×1013 pixels). The threshold value was chosen in a region where a small variation of that value generates large variations of the porosity [14]. The 20 gray scale (0-255 gray scales) images were then converted into binary images. The binary images gave an indication of the total porosity, which were used to obtain average of porosity. Based on an aspect ratio and direction, the total pores were categorized into interlamellar pores (aspect ratio less than 1/6, angle between this pore and horizontal line less than 45°) and globular pores (all of the remaining). Total porosity was also measured by Archimedes' method to complement the image analysis results. Finally, surface-connected porosity was measured by MIP using a Quantachrome Autoscan 33* porosimeter.

4.2.2. Thermal conductivity:

For all of the characterization and measurements, free standing form of the coating was obtained by grinding the substrate away from the back side to a thickness of 100~300μm and then bending substrate carefully to detach the coating from it. [At the thickness, the ceramics separate readily from the aluminum substrates]. Subsequently, the coating edges were rounded to a disk with diameter 12.7 mm and coated with graphite. Room temperature through thickness thermal conductivity was measured using a Holometrix Laser Flash Instrument. Specific heat and thermal diffusivity were also measured and allowed simultaneously extraction of the thermal conductivity. High temperature thermal diffusivity was obtained at Oak Ridge National Laboratory using an Anter Flashline 5000 Laser Flash Thermal Diffusivity (LFTD) system. Differential Scanning Calorimeter (DSC) system was conducted in nitrogen atmosphere for high temperature specific heat measurement. The high temperature thermal conductivity values (through thickness) were then calculated using thermal diffusivity, specific heat and density.

4.3 Results

In the following section, we present the microstructure, porosity and thermal conductivity results for each cluster of YSZ coatings.

4.3.1 Effect of Starting Powder Morphology:

A number of past investigations have examined the effect of powder feedstock particle size distribution and manufacturing methods on the microstructural characteristics of YSZ coatings [4-6, 13]. These studies have shown that both powder morphology and particle size distribution play an important role in the effective porosity and, therefore, thermal conductivity of the coating. However, in these studies, the process parameters were kept constant and the powder feedstock was the only variable. In recent years, it has been observed that optimization of particle injection and particle parameters differ greatly for different morphologies and sizes [4, 6, 9, 10, 13, 15]. Particle injection into the plasma flame is a crucial variable that determines the effectiveness of the particle-plasma interaction and therefore the deposit formation dynamics. In this study, the injection locations of different powders were controlled so as to produce the most optimum particle state in terms of temperature and velocity [16]. In the case of powder morphologies, as discussed earlier, the effective particle states were similar in both average (T, V) and distribution, thus enabling a critical comparison of the microstructure-property relationships.

Figure 4.1 compares the microstructures of the three starting morphologies deposited at the nominal "same particle T, V" condition. The micrographs suggest that all three coatings contain significant porosity, with the A&S material showing a somewhat higher pore content. Image analysis was used to discriminate the pore

architecture and the results are shown below the images in Fig. 4.1. The results confirm the visual observation that the A&S material displayed a higher porosity, however, the content of interlamellar porosity with respect to total porosity was largest for the HOSP material. Concurrent measurements of porosity through other techniques, precision density, He pycnometry and mercury intrusion porosimetry are presented in Table 4.1. Each technique samples a different aspects of the pore structure, neverthless all results consistently indicate that the progressive increase in porosity FC>HOSP>AS sprayed at conditions achieving similar particle temperatures, velocities and (T, V) distributions.

Globular Porosity 17.7%	Globular Porosity 23.3%	Globular Porosity 17.9%
Interlamellar Porosity 3.3%	Interlamellar Porosity 1.7%	Interlamellar Porosity 2.1%
HOSP	A&S	F&C

Figure 4.1 Image analysis based discrimination of pore architecture for YSZ coatings made of different morphology powders and similar particle characteristics during spraying

Table 4.1 Total porosity of YSZ coatings made of three morphology powders measured by various techniques

Powder Morphology	Porosity %(IA)	Porosity % (Precision density)	Porosity % (Archimedes')	Porosity % (Pycnometer)	Porosity % (MIP)
HOSP	21%	22.4	18.5	20.8	9.7
A&S	25%	26.3	22	22	13.8
F&C	20%	16.4	16.8	15	5.2

Plasma sprayed TBCs undergo significant microstructural changes upon exposure to a high temperature environment. As such, the dynamic evolution of the microstructure with thermal exposure is of interest.   To understand the effect of thermal exposure on coating microstructure and thermal conductivity, studies were performed for thermally cycled and isothermally aged YSZ coatings made of three different morphology powders. Figure 4.2 compares the effect of thermal cycling at 1100°C (30 minutes heating and 15 minutes cooling for each cycle for a total 20 cycles) and isothermal exposure at 1200 ^{o}C for 225 hrs on the room temperature thermal conductivity of the above three coatings. [*The selection of these thermal aging conditions is based on respective application issues in aeroengine and land-based turbine applications. The land-based turbines experience*

prolonged exposure at high temperatures while the aeroengine turbines experience more cyclic environments].

All three coatings showed substantial increase in thermal conductivity upon exposure. However, the relative changes in thermal conductivity among the three morphology coatings are considerably different. Several notable observations can be made:

- Higher temperature (1200°C) and longer exposure in the isothermal test leads to enhanced sintering compared to lower temperature (1100°C) cyclic exposure.
- The propensity for sintering is higher for denser starting microstructures; the F&C material shows a substantial increase in thermal conductivity reaching values close 2W/mK for both cyclic and isothermal cases.
- The HOSP material with the largest fraction and width of interlamellar pores in the as-sprayed state displayed the least change in both cases. This is consistent with findings by Kulkarni et al. [4] and Wang et al. [5] who have reported larger open dimension of interlamellar pores of HOSP coatings.

<center>(a)   (b)</center>

Figure 4.2 Effect of thermal aging on room temperature thermal conductivity of coatings made of different morphology powders (a) thermal cycled (b) isothermal exposure

These results, which will be discussed below, suggest that the nature of the pores and interfaces play a crucial role in the sintering of the spray deposited layers.

Figure 4.3 compares the temperature dependent thermal conductivity of the three coatings in both as-sprayed and thermally aged conditions. The results once again indicate that the HOSP material displays the lowest thermal conductivity across the entire temperature range and is linked to the presence of larger fraction of interlamellar pores. Thus, the effective starting microstructure determines the thermal conductivity at high temperature.

Upon thermal exposure, under both cyclic and isothermal conditions, an overall increase in the thermal conductivity is observed with the isothermal again displaying a consistently larger change. The temperature is chosen at 1100°C for examining the change of high temperature thermal conductivity after both cyclic and isothermal conditions. A notable observation is that the levels of change at 1100°C are different from those at room temperature.
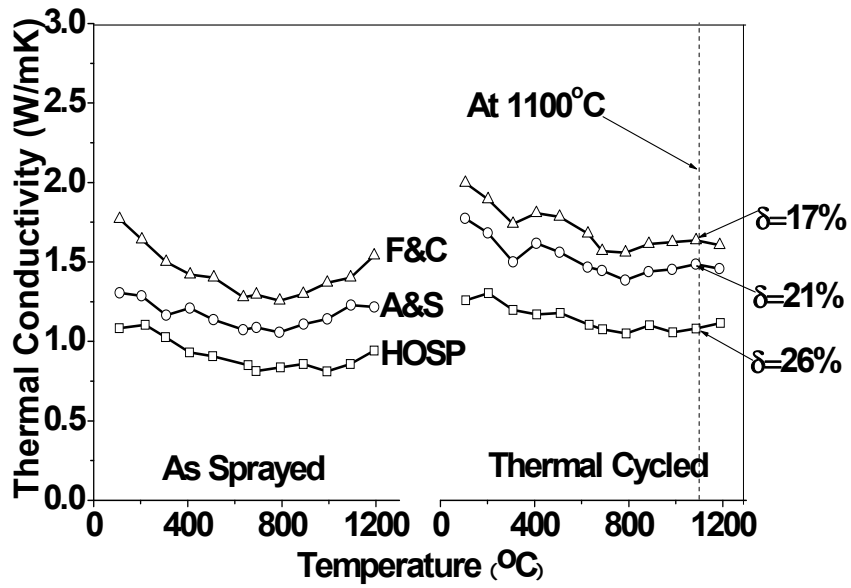
(a)
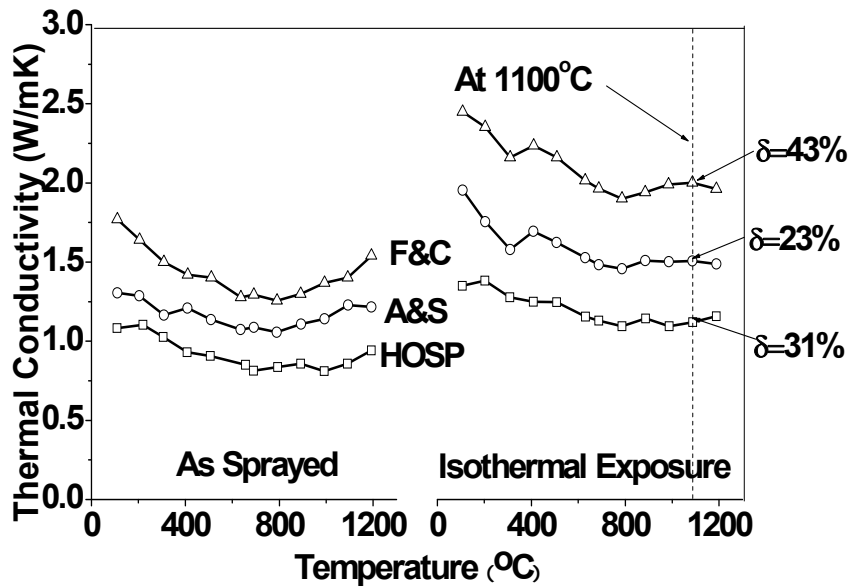
(b)

Figure 4.3 Temperature dependent of thermal conductivity for YSZ coatings made of different morphology powders (a) thermal cycled (b) isothermal exposure

44

4.3.2 Effect of Particle Size Distribution

Particle size distribution affects not only the behavior of the particles in the plasma spray but also influences the individual splat thickness associated with larger or smaller particle volumes. Although it would be ideal to choose narrow distributions to reduce overall process variability, it is impractical and non-economical from an application point of view. However, particle size distribution affects the assemblage of the coatings and the resultant microstructure. To investigate these effects, three sets of coatings were investigated in this study with the F&C powder. Ensemble represents the broad distribution from 10 microns to 75 microns with a mean of 50 microns. The ensemble powder was divided into a coarse and narrow cut with resulting sizes of 45-75 microns and a fine and narrow cut with size of 10-45 microns.

The microstructures of the coatings produced with the three size distributions and the corresponding image analysis results of the pore distributions are shown in Fig. 4.4. The results as expected indicate that the finer powder distribution results in denser coatings compared to coarse and ensemble. However, the effective ratio of interlamellar pores *vs* total porosity is substantially larger in the case of the fine powder. Figure 4.4 provides a breakdown of the pore architecture obtained from image analysis. These results suggest that despite a lower overall porosity the finer powder distribution yields coatings with larger fraction of interlamellar pores and splat interfaces. Porosity results obtained from other measurements are included in Table 4.2 for completeness. The results are consistent with findings from image analysis techniques and indicate that the total porosity becomes lower with the decrease of particle size.
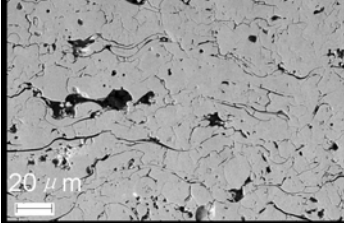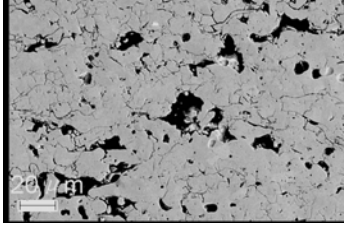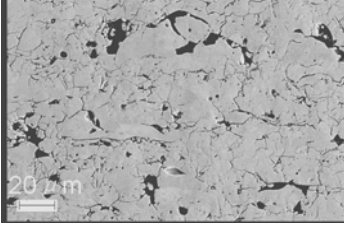

Globular Porosity 18.2% Interlamellar Porosity 3.2%	Globular Porosity 20.5% Interlamellar Porosity 2.6%	Globular Porosity 23.1% Interlamellar Porosity 1.5%
Fine (10-45μm)	Ensemble (10-75μm)	Coarse (45-75μm)
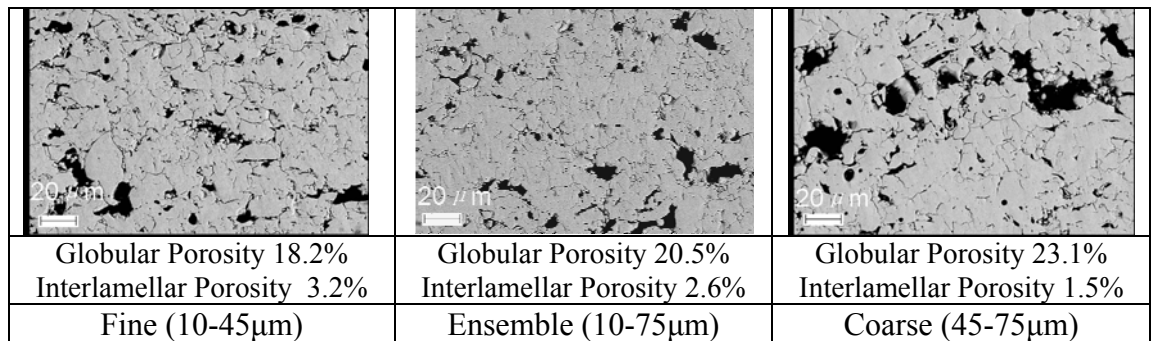
Figure 4.4 Microstructure of cross-sections of coatings made of different size powders for porosity determination

Table 4.2 Percentage porosity of YSZ coatings made by three particle size powders

Powder Morphology	Porosity % (IA)	Porosity % (Precision density)	Porosity % (Archimedes')	Porosity % (Pycnometer)	Porosity % (MIP)
Fine	21.4	21.8	21.6	20.4	5.9
Ensemble	23.1	24.9	22.5	23.1	9
Coarse	24.6	29.7	24.6	26.4	13.2

Fig. 4.5 compares the effect of thermal cycling and isothermal exposure on the room temperature thermal conductivity of the three coatings made from different size powders. [similar exposure conditions were applied as in the powder morphology case]. Here again, the results suggest that despite overall lower porosity in the fine powder, the thermal conductivity is lower indicating that the effective through thickness thermal conductivity is dominated by the interlamellar pores and splat interfaces. The finer powder yields a larger fraction of interlamellar interface for a given unit thickness and as such provides a thermal barrier effect. However, in Fig. 4.5, the increase of thermal conductivity reduces with the increase of particle size for both thermal cycling and isothermal exposure. Kulkarni [17] has observed that the open dimensions of pores and interfaces are larger, which is consistent with the finding from Fig. 4.4. The coarse material is less susceptible to sintering under either thermal cycling or isothermal exposures compared to the ensemble material or the fine materials due to larger open dimensions of pores and interfaces. Again, these results point to similar conclusions as in the powder morphology case, i.e. the nature of the defect structures is critical in determining the as-sprayed thermal conductivity and the stability of the microstructure during thermal aging.
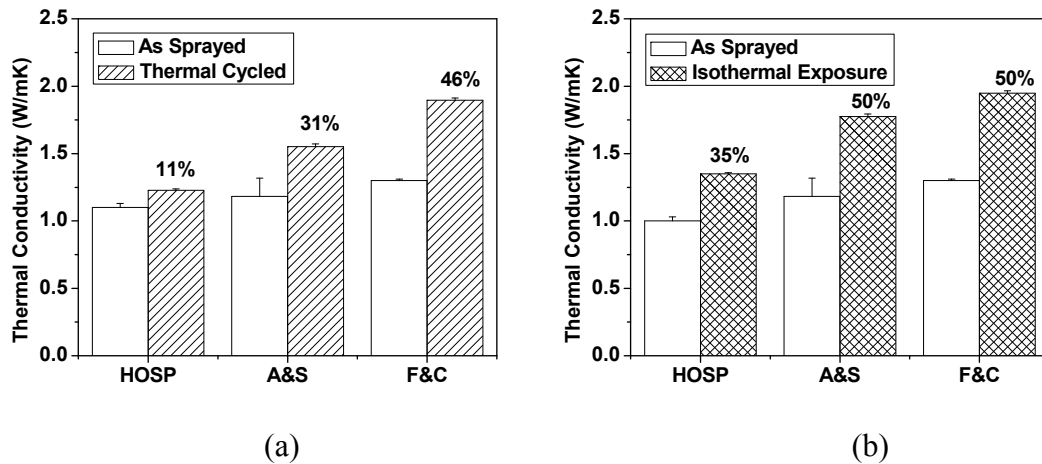

Figure 4.5 Effect of thermal exposure on room temperature thermal conductivities of coatings made of different size powders (a) thermal cycled (b) isothermal exposure

Fig. 4.6 also compares the effect of thermal cycling and isothermal aging on the temperature dependent thermal conductivity. The trends are similar to the powder morphology and particle size study and indicate a significant increase in overall thermal conductivity upon isothermal aging compared to thermal cycling. The effective starting microstructure determines the thermal conductivity at high temperature. The high temperature (1100°C) thermal conductivity has been investigated for the change resulted from thermal cycling and isothermal exposure. The levels of change showed reversed trend to ambient results, except for the similar increase of thermal conductivity for ensemble and coarse coatings in the case of isothermal exposure.
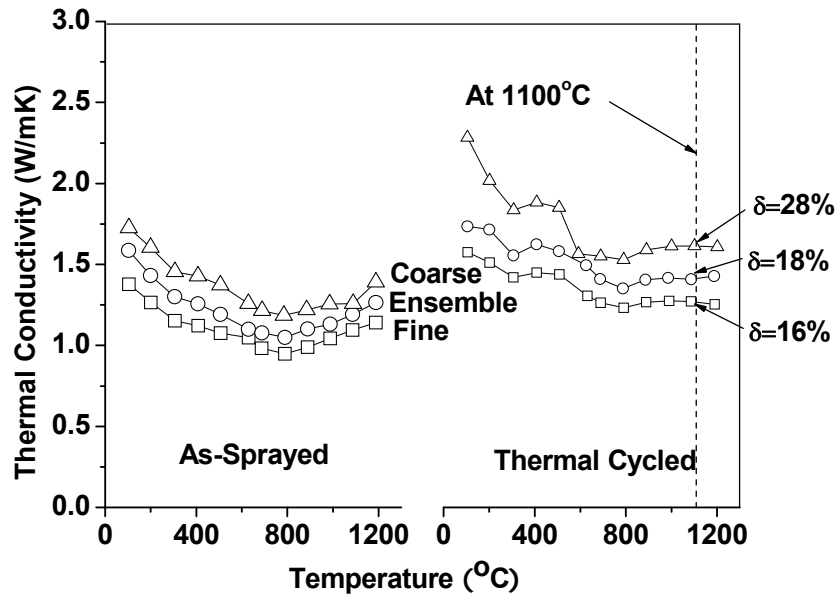
(a)
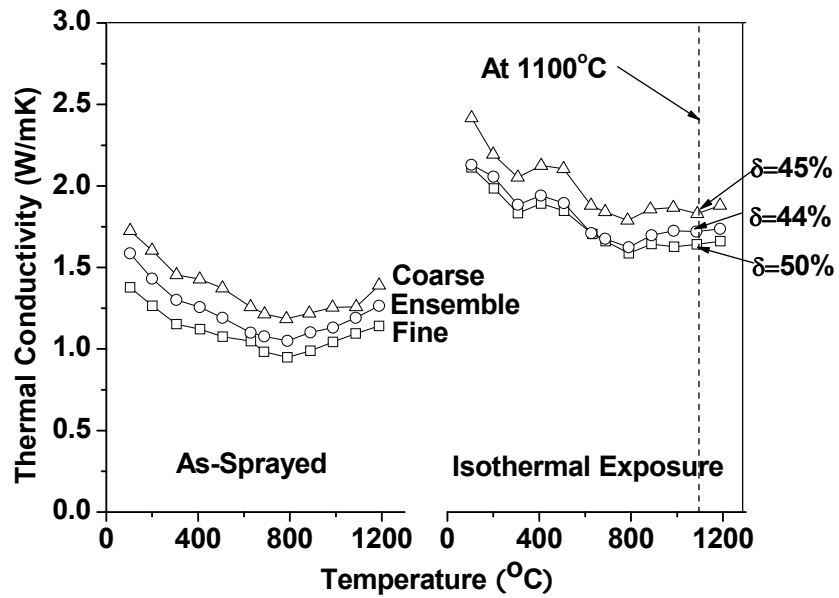
(b)

Figure 4.6 Temperature dependent of thermal conductivity for YSZ coatings made of different size powders. (a) thermal cycled (b) isothermal exposure

4.3.3 Changing Plasma Spray Parameter Space to Alter the Microstructure:

It is well known that the process conditions can affect the particle state and therefore the microstructure and properties of coatings. To critically examine the sensitivity of process conditions on the microstructure-thermal conductivity relationships, three coatings were produced at different conditions. The output of process parameters is reflected in the form of changes to the particle state, namely the particle velocity and particle temperature. The process characteristics used to produce coatings with the ensemble F&C powder, and are described in Table 4.3.

Table 4.3 Process conditions used to achieve different particle states

Process Condition	Particle Temperature (^{o}C)	Particle Velocity (m/s)
Low avg. T-V	2504	80
Medium avg. T-V	2631	103
High avg. T-V	2677	150

The microstructures of the coatings and the corresponding image analysis results of the pore distributions are shown in Fig. 4.7 along with porosity measured by other methods in Table 4.4. The results trend as anticipated, i.e. increasing density with increasing particle temperatures and velocities. The fraction of interlamellar pores is also larger for the low T-V condition and progressively decreasing with increasing T-V parameters. The medium T-V and high T-V sample have similar interlamellar porosity as well as total porosity. This is because the highest velocity reduces the dwell time and melting efficiency, and therefore increases the porosity. The high T-V improves the contact between splats and shortens the length of interlamellar pores. Thinner interfaces can also be observed in Figure 4.7 (c).

Globular Porosity 27.5% Interlamellar Porosity 2.5%	Globular Porosity 18% Interlamellar Porosity 1.8%	Globular Porosity 17.4% Interlamellar Porosity 1.9%
Low T-V	Medium T-V	High T-V
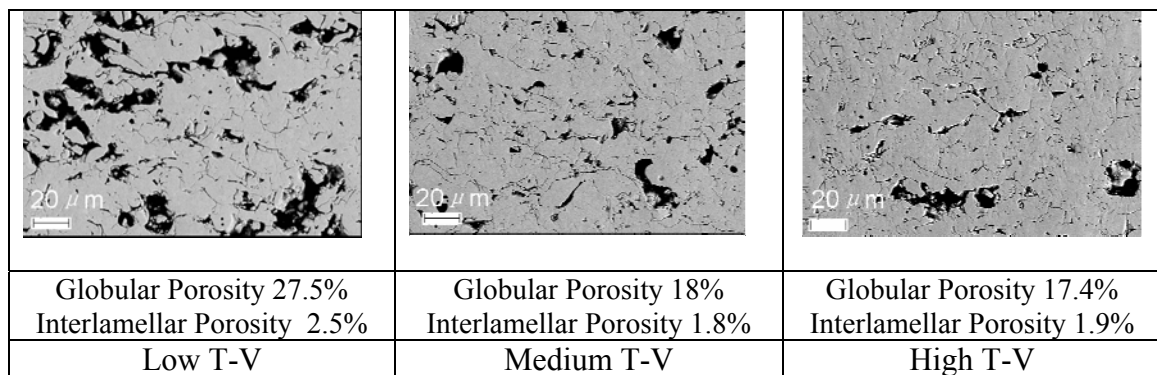
Figure 4.7 Microstructure of cross-sections of coatings made at different particle states

Table 4.4 Percentage porosity of YSZ coatings made at different particle state

Process Condition	Porosity %(IA)	Porosity % (Precision density)	Porosity % (Archimedes')	Porosity % (Pycnometer)	Porosity % (MIP)
Low T-V	30	28.7	25.1	23.7	15.2
Medium T-V	19.8	19.1	17.1	18.3	9.5
High T-V	19.3	18.7	16.3	17.8	3.3

Fig. 4.8 compares the effect of thermal cycling and isothermal exposure on the room temperature thermal conductivity of the coatings made at different particle states. The results suggest that as the particle parameters are increased, the effective contact between splats is improved, resulting in a much more rapid sintering of the coating as evidenced by the medium and high T-V system. But the high thermal conductivity of as-sprayed high T-V coating restricts the amplitude of increase resulted from thermal aging. Figure 4.9 further compares the effect of cyclic and isothermal exposure of the coatings and the increase of thermal conductivity tested at 1100°C are shown for both the thermal cyclic and isothermal exposure conditions. All the coatings show substantial sintering and the effective change is related to amount of starting porosity and the nature of the interfaces. After both thermal cycling and isothermal exposure, the difference of high temperature thermal conductivity change between low T-V and medium T-V coatings becomes smaller compared with that of the room temperature data (Fig. 4.8 and 4.9). The high T-V coating shows the least increase of thermal conductivity. But the three coatings still follow the same sequence of thermal conductivity from the highest to the lowest as the case of room temperature.

(a) (b)
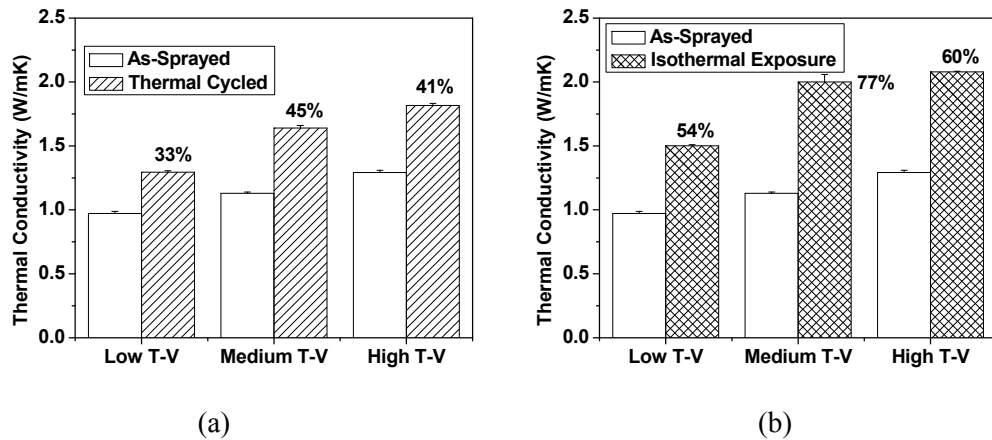
Figure 4.8 Effect of thermal exposure on room temperature thermal conductivities made at different T-V (a) thermal cycled (b) isothermal exposure

All the results illustrate that substantially different thermal conductivities can be attained with changes to process conditions and offer a pathway to the tune the microstructure for optimum performance.
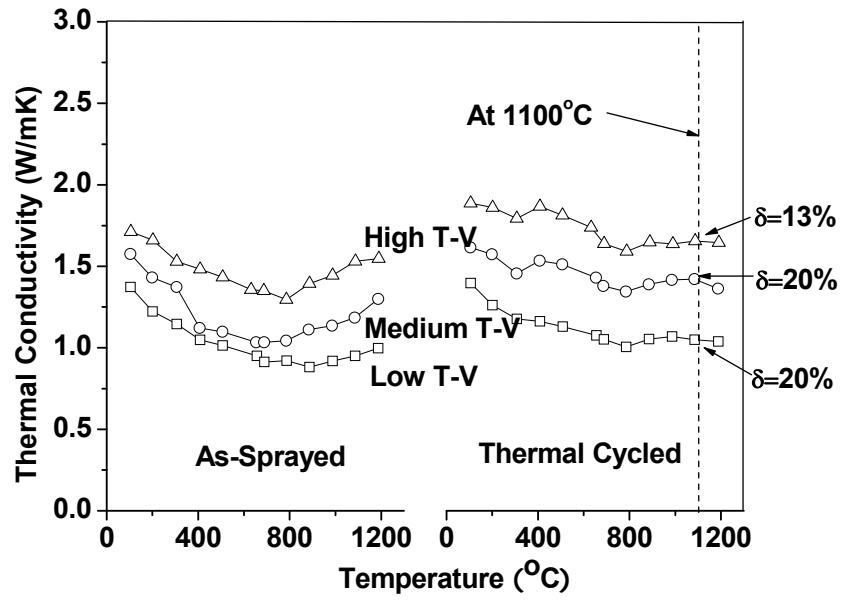
(a)
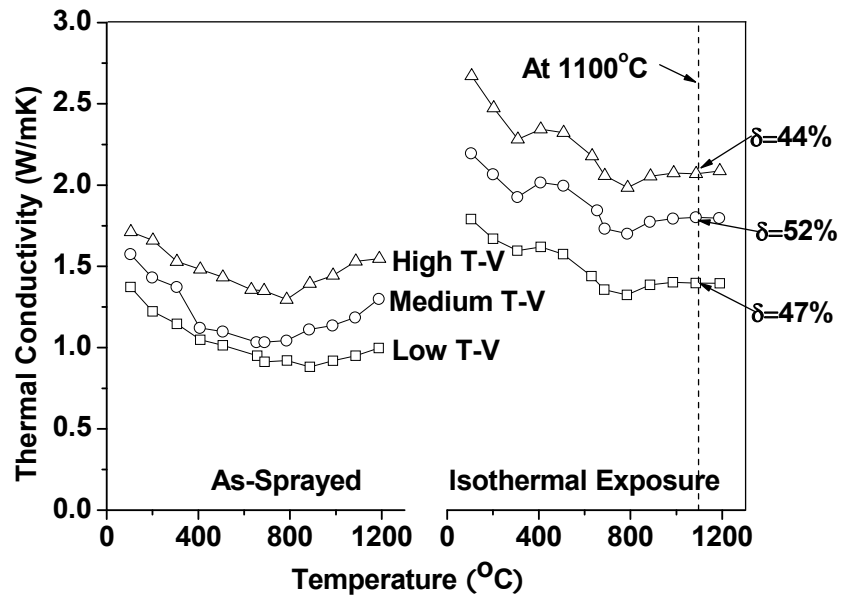
(b)

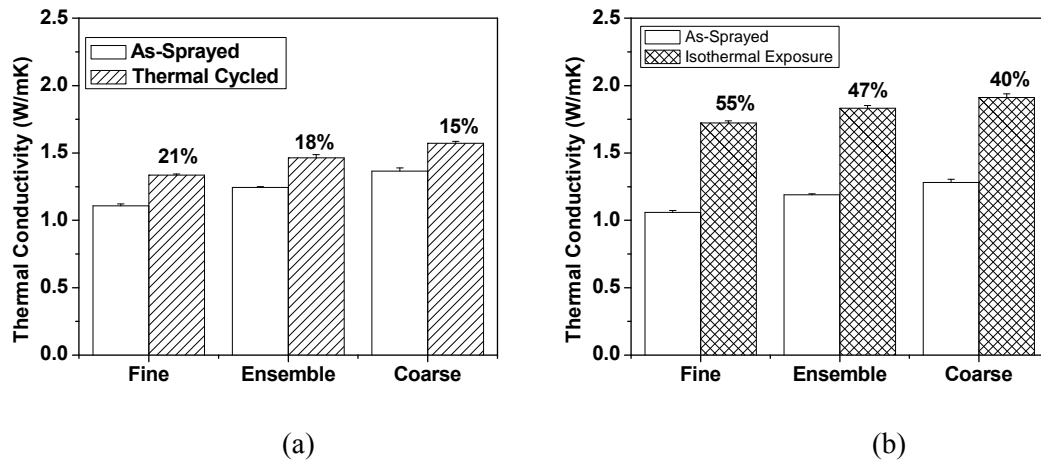Figure 4.9 Effect of thermal exposure on high temperature thermal conductivities of coatings made at different T-V (a) thermal cycled (b) isothermal exposure

4.4 Discussion:

This study systematically examines the thermal conductivity-porosity relationships for a range of plasma sprayed YSZ coatings produced with controlled changes in process conditions and resulting microstructures. Such a systematic approach enables distilling the intrinsic microstructural differences achieved through feedstock and process modifications and enables a critical assessment of the process variables on the resultant thermal properties of the coatings. In the following discussion, we seek to synthesize commonalities in the observed results from the three sets of coatings and establish a mapping strategy to enable future coating design and process optimization.

4.4.1 Porosity - Thermal Conductivity Maps:

As a first step, the through thickness thermal conductivity of the 3 sets of coatings described in the results have been combined into a single graph. The results are shown in Figure 4.10. When initially plotted, the data shows no pattern. However, one can reconcile a portion of the data to follow an inverse linear relationship of thermal conductivity with porosity. This is depicted in Fig. 4.10 as the "expected trend". The origin of such an inverse linear relationship dates back to Maxwell [18] and has been addressed in significant detail in recent years by Klemens [19], Pawlowski and Fauchais [20] and by Schlicting, Klemens and Padture [21]. The basis of this relationship is to treat the porous material as an effective medium comprising of two phases (matrix which in this case is YSZ and air being the other phase). Klemens [19] proposed an initial relation $\frac{Kporous}{Kdense} = 1 - \frac{4}{3}P$ for general porous materials. Pawlowski and Fauchais [20] suggest that the effective thermal conductivity of porous coatings follows Keff/Km = 1-Pc, where Km is the matrix thermal conductivity (in this case zirconia) and Pc is the fraction of sample surface area of pores perpendicular to the thermal flux. It has been suggested that such an approach is valid for low temperature thermal conductivity of plasma sprayed YSZ. Schlicting et al. [21] examined the relationship through experiments for dense and porous YSZ (not specifically for plasma spray) and proposed a relationship $\frac{Kporous}{Kdense} = 1 - \frac{3}{2}P$. The results presented in this work capture the overall inverse-linear trend but none of the coefficients described above matches the results in Fig. 4.10. A number of factors can explain this: not all of the porosity is captured in the measurements and significant anisotropy in pore structure exists in plasma sprayed YSZ which can affect the findings. Nevertheless, the results provide new insight to visualize various coatings.

The results point to two regimes which deviate from the expected trend in Fig. 4.10(a). In general thinner splats produced by the HOSP material and the fine powder as well as made at medium T-V tend to fall substantially below this line. This confirms the role of the larger fraction of interlamellar pores and splat interfaces in this set of coatings which play the dominant role in reducing the effective thermal conductivity. It is somewhat unexpected that the medium T-V condition from the process variation study

falls below the trend line. A closer examination of the microstructure of the medium T-V coating shows higher flattening ratio and longer interlamellar pores with larger open dimension without concomitant compaction by the high velocity impact. The high T-V coating has better contact between splats and shorter interlamellar pores (as discerned from Fig. 4.7) benefiting from the high thermal and kinetic energy during the spraying, which gives rise to higher thermal conductivity than the medium T-V coating despite the similar interlamellar porosity. Thus the thermal conductivity for high T-V sample falls along the trend line. The coarse material as expected falls above the line since despite a larger pore fraction, the coarser material will introduce a smaller number of interlamellar porosity and splat interfaces for given coating thickness.

In order to reconcile the observations in Figure 4.10 (a), the number of interlamellar interfaces in the coating cross-section was calculated via the linear intercept method. Cross-section images of coatings taken at 5000x magnifications were used to observe the splat interfaces and calculate the average of splat thickness. The visible splat interfaces were marked along a line. Thickness for each splat was measured and recorded. Then, the average of splat thickness was obtained. This was performed for the powder size distribution study using F&C powders. The results suggest that the average splat size for the coatings produced from the fine powder is ~ 4 microns while that of ensemble is ~ 5.3 microns and for the coarse 6.6 microns. The smaller splat size would result in a larger number of through thickness interfaces and will effectively reduce the thermal conductivity. Similar observations have been reported in the case of the powder morphology differences by Wang et al. [5]and hence not re-examined here.

The thermal conductivity of interest for TBCs is at the operating temperatures which are in the range of the 1000-1200°C. As such it is relevant to map the microstructural effects on thermal conductivity at this temperature. Figure 4.10 (b) shows the temperature dependent thermal conductivity measured at 1100°C (data are available for continuous range but 1100°C is chosen for representative description). The difference of thermal conductivity between coatings made of HOSP powder and F&C powder is further accentuated at high temperature compared to room temperature. This can be attributed to two effects: (i) the materials undergo localized sintering even during the conductivity measurement as the specimens are held for approximately 30 mins at these elevated temperatures. The larger pore opening dimension of interlamellar pores for HOSP coating reduces the overall conductivity compared to F&C coating. The F&C coating with smaller interlamellar pore opening dimension has a greater propensity for sintering and thus accentuating the observed thermal conductivity differences. (ii) The photon mechanism makes the thermal conductivity proportional to T^3 for bulk materials. The F&C coating has fewer interfaces than does the HOSP coating, resulting in reduced photon scattering. Therefore, high temperature thermal conductivity of F&C coating increases faster with temperature. Both the effects contribute to the accentuation of the difference of thermal conductivity between F&C and HOSP coatings at 1100°C.Other issues of different transport mechanism may also play a role but it is unclear from these results.
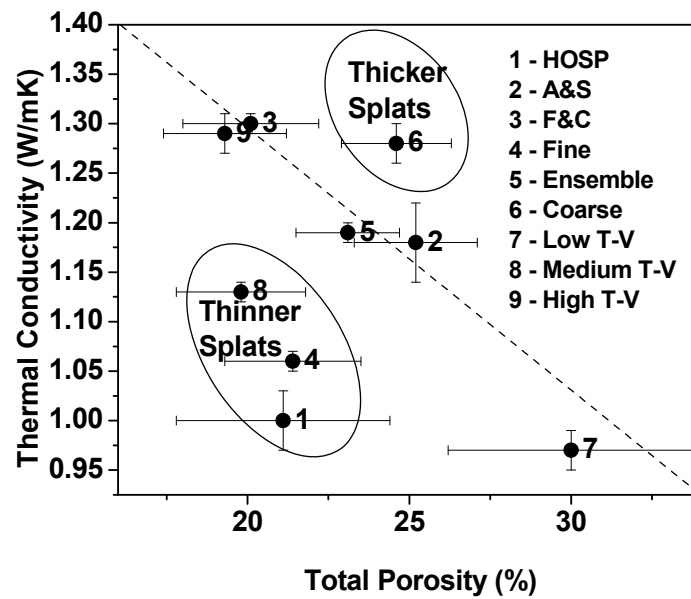
(a)
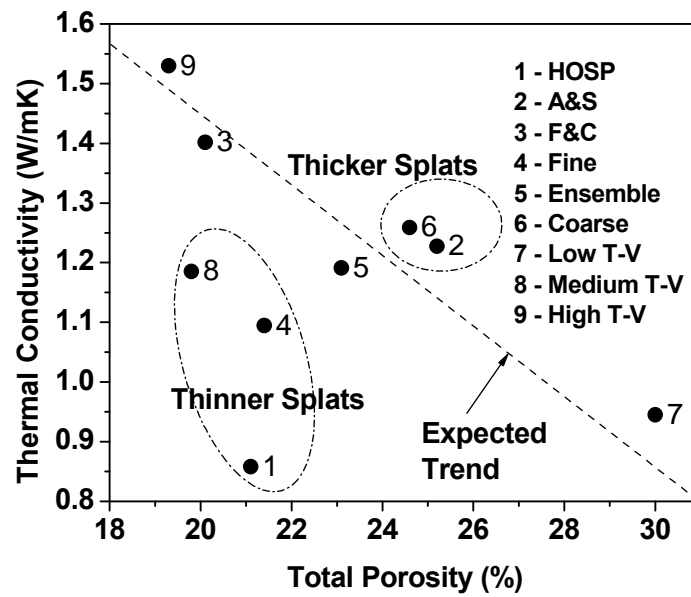
(b)

Figure 4.10 Thermal conductivity-porosity map of YSZ coatings

(a) RT thermal conductivity (b) thermal conductivity measured at 1100°C

4.4.2 Effect of Annealing on Room Temperature Thermal Conductivity

Figure 4.11 shows the thermal conductivity-porosity maps before and after thermal aging (both thermal cycling at $1100^{o}C$ and isothermal exposure at $1200^{o}C$). Although there is a limited decrease in overall porosity with the thermal aging, both types of aging induce considerable increase in thermal conductivity due to sintering of the interlamellar interfaces.

The rapid increase in thermal conductivity of the F&C coatings during isothermal exposure is consistent with prior observations by Trice et al. , who reported a distinct change in the interlamellar pores after the 50-hour/$1200^{o}C$ heat treatment [22]. In the case of thermal cycling, Wang et al. [5] have exploited small angle neutron scattering to characterize the microstructure of YSZ coatings of as-sprayed and 10 cycles at the same heat treatment condition. Here again the results pointed to the elimination of splat-splat interfaces with concomitant increase of thermal conductivity. The disappearance of splat boundaries provided a significant contribution to total reduction in the effective thermal transport property. Ultra small angle x-ray scattering studies carried out by Kulkarni et al. also showed that the larger interlamellar pores tended to decrease the open dimension even if they were not completely closed after thermal cycling [17].

It is clear from Figure 4.11 higher temperature and isothermal exposure cause a substantially larger increase of thermal conductivity for both low porosity and high porosity coatings. In order to clarify the effect of temperature and cycling, an additional experiment was carried out on select samples for the $1100^{o}C$ exposure. A 10 h isothermal exposure at $1100^{o}C$ was conducted to achieve the same "hot time" as the cycling study. Although the thermal conductivity increase was marginally higher after isothermal exposure (10h), there was no significant difference from thermal cycling (20cycles).

It is also found that for both thermal cycling and isothermal exposure, the coatings with higher density sinter more rapidly with a larger amplitude increase of room temperature thermal conductivity, as shown in Fig. 4.11. The coating made of coarse F&C powder has the highest total porosity and results in the lowest increase of thermal conductivity after either thermal cycling or isothermal exposure, whereas the fine powder coating (with lower starting porosity) shows the fastest increase of thermal conductivity despite the lower intrinsic thermal conductivity (Fig. 4.5).

An outlier to this behavior is the HOSP coating displaying the slowest increase of thermal conductivity despite the lower starting porosity (Fig. 4.2). As mentioned earlier and evidenced through neutron scattering studies, the HOSP material has the widest and longest interlamellar pores which reduces the propensity to sintering.

An additional effect to consider in the analysis is saturation effects in terms of thermal conductivity increase. The F&C powder coating is generally more prone to sintering due to smaller pore opening dimension. However, given that the initial conductivity itself is high, the effective increase is smaller particularly for long term isothermal exposure, as evidenced by several coatings described in Fig. 4.2 and Fig. 4.9. Wang et al. [23] found similar saturation effects in that the thermal conductivity increases slowly if it approaches the upper limit (that of fully dense YSZ).
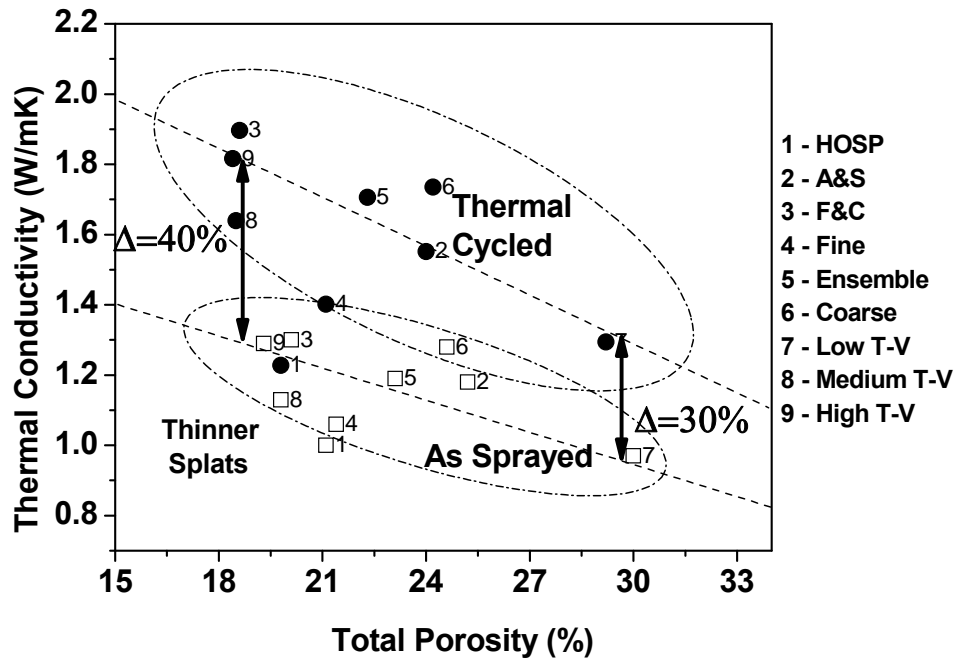
(a)
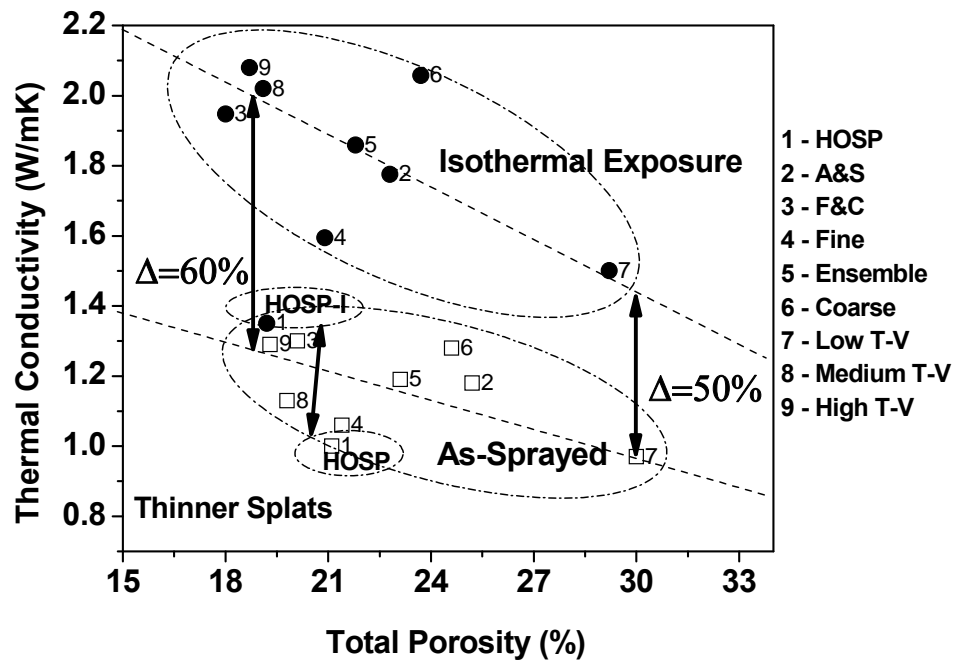
(b)

Figure 4.11 The effect of annealing on porosity and room temperature thermal conductivity of YSZ coatings (a) thermal cycling (b) isothermal exposure

4.4.3 Effect of Annealing on Temperature Dependent Thermal Conductivity

Figure 4.12 is a representation of the thermal conductivity-porosity relations based on the 1100°C thermal conductivity measurements. Results are presented both for thermal cycling at 1100°C and isothermal annealing at 1200°C. Two interesting phenomena can be observed.

- The overall increase in 1100°C thermal conductivity upon thermal cycling is considerably smaller than those observed in the room temperature measurements. Similar results are also observed for the 1200°C isothermal case with considerably longer exposure time.
- The effective increase is similar for both low porosity and high porosity coatings (15% for the cyclic exposure, and 40% for isothermal exposure), which is quite different compared to the changes observed in the room temperature measurements.

The smaller differences in high temperature thermal conductivity of the various microstructure may be related to the enhanced effects of radiation at high temperatures [20] and possibly also due to insitu sintering of the as-sprayed coating during measurement [23]. This requires further fundamental analysis in the future.
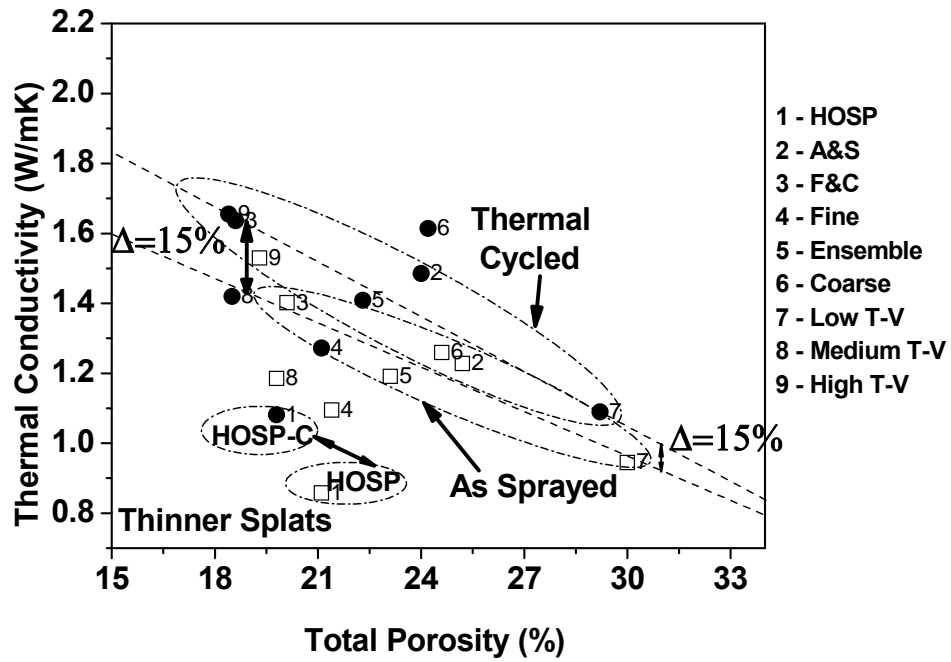
(a)
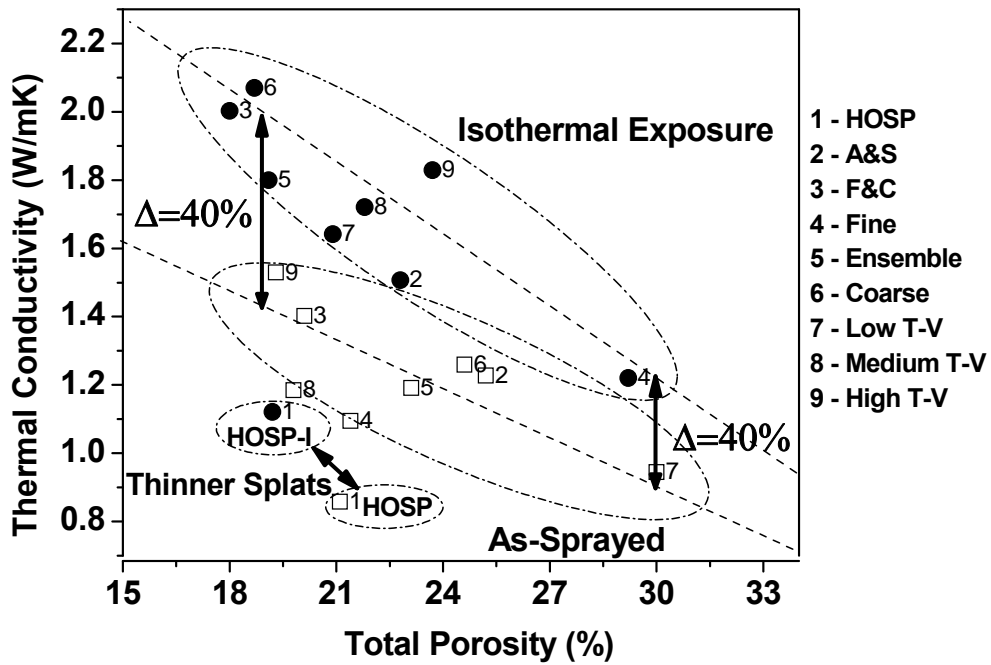
(b)

Figure 4.12 Temperature dependent thermal conductivity at 1100°C-porosity map of YSZ coatings (a) thermal cycling (b) isothermal exposure

4.5 Conclusions

The room temperature and temperature dependent thermal conductivities have been investigated for three coating systems and the thermal conductivity-porosity map was established to access the microstructure- thermal transport property relationship. It is found that the effective starting microstructure determines both the room temperature and temperature dependent thermal conductivity. The important role of interlamellar porosity in both room temperature and temperature dependent thermal conductivity has been pointed out. The difference of splat thickness results in different amount of interfaces and therefore makes the thermal conductivity deviate from the trend line.

The effects of thermal cycles and isothermal annealing on both room temperature and high temperature thermal conductivity were examined. The thermal conductivity increases significantly after thermal cycling and isothermal exposure due to the closure of interfaces despite of a limited decrease in overall porosity.

It is found that the open dimension of interlamellar pores plays a significant role in sintering and therefore the change of thermal conductivity. The larger open dimension of interlamellar pores is unfavorable of sintering and reduces the percentage increase of thermal conductivity. It is also found that the F&C material with low porosity has the smallest potential of thermal conductivity increase due to the saturation effects.

Another notable observation is that the levels of change at $1100^{o}C$ are different from those at room temperature.   This phenomenon maybe results from the enhanced effects of radiation at high temperatures and the sintering only for as-sprayed coating during measurement. More investigations are required to explore the mechanism that causes the difference.

This study gives the clue to choose materials and spraying parameters for the design of coating microstructure and property. It also offers the understanding of the relationship between microstructural defects and thermal conductivity as well as the assessment of the dynamic behavior during service and the life time prediction for application.

References

1.   D. R. Clarke and C. G. Levi, Materials design for the next generation thermal barrier coatings, *Annual Review of Materials Research*, Vol. 33, 2003, p. 383-417.

2.   J. Ilavsky, G. G. Long, A. J. Allen and C. C. Berndt, Evolution of the void structure in plasma-sprayed YSZ deposits during heating, *Materials Science and Engineering a-Structural Materials Properties Microstructure and Processing*, Vol. 272, No.1, 1999, p. 215-221.

3.   J. Ilavsky, G. G. Long, A. J. Allen, H. Herman and C. C. Berndt, Use of small-angle neutron scattering for the characterization of anisotropic structures produced by thermal spraying, *Ceramics-Silikaty*, Vol. 42, No.3, 1998, p. 81-89.

4.   A. Kulkarni, Z. Wang, T. Nakamura, S. Sampath, A. Goland, H. Herman, J. Allen, J. Ilavsky, G. Long, J. Frahm and R. W. Steinbrech, Comprehensive microstructural characterization and predictive property modeling of plasma-sprayed zirconia coatings, *Acta Materialia*, Vol. 51, No.9, 2003, p. 2457-2475.

5.   Z. Wang, A. Kulkarni, S. Deshpande, T. Nakamura and H. Herman, Effects of pores and interfaces on effective properties of plasma sprayed zirconia coatings, *Acta Materialia*, Vol. 51, No.18, 2003, p. 5319-5334.

6.   S. Deshpande, A. Kulkarni, S. Sampath and H. Herman, Application of image analysis for characterization of porosity in thermal spray coatings and correlation with small angle neutron scattering, *Surface & Coatings Technology*, Vol. 187, No.1, 2004, p. 6-16.

7.   A. Vaidya, Process Maps for Thermal Spray: A Fundamental Approach to Process Property Relationships *Ph. D Thesis, State University of New York at Stony Brook*, 2004.

8.   A. Vaidya, T. Streibl, L. Li, S. Sampath, O. Kovarik and R. Greenlaw, An integrated study of thermal spray process-structure-property correlations: A case study for plasma sprayed molybdenum coatings, *Materials Science and Engineering a-Structural Materials Properties Microstructure and Processing*, Vol. 403, No.1-2, 2005, p. 191-204.

9.   T. Streibl, A. Vaidya, M. Friis, V. Srinivasan and S. Sampath, A critical assessment of particle temperature distributions during plasma spraying: Experimental results for YSZ, *Plasma Chemistry and Plasma Processing*, Vol. 26, No.1, 2006, p. 73-102.

10.   V. Srinivasan, A. Vaidya, T. Streibl, M. Friis and S. Sampath, On the reproducibility of air plasma spray process and control of particle state, *Journal of Thermal Spray Technology*, Vol. 15, No.4, 2006, p. 739-743.

11.   S. Sampath, V. Srinivasan, A. Vaidya, A. Gouldstone, Y. Liu and T. Nakamura, Sensing, Control, and Insitu Extraction of Coating Properties: An Integrated Approach towards Establishing Process Maps, *Thermal Spray Conference & Expositions (ITSC) Seattle, Washington, Electronic Proceedings.*, 2006.

12.   A. Vaidya, T. Streibl, S. Sampath and H. Zhang, A Comparative Diagnostic Analysis of Morphologically Different YSZ Powders, *Thermal Spray Solutions: Advances in Technology and application (ITSC 2004), Osaka, Japan, Proceedings of ASM Electronic Proc.*, 2004.

13.   A. Kulkarni, A. Vaidya, A. Goland, S. Sampath and H. Herman, Processing effects on porosity-property correlations in plasma sprayed yttria-stabilized zirconia coatings, *Materials Science and Engineering a-Structural Materials Properties Microstructure and Processing*, Vol. 359, No.1-2, 2003, p. 100-111.

14.   O. Lavigne, Y. Renollet, M. Poulain, C. Rio, P. Moretto, P. Brannvall and J. Wigren, Microstructural characterization of plasma sprayed thermal barrier coatings by quantitative image analysis, *Quantitative microscopy of high temperature materials conference, Sheffield, UK*, 1999.

15.   E. Turunen, T. Varis, S. P. Hannula, A. Vaidya, A. Kulkarni, J. Gutleber, S. Sampath and H. Herman, On the role of particle state and deposition procedure on mechanical, tribological and dielectric response of high velocity oxy-fuel sprayed alumina coatings, *Materials Science and Engineering a-Structural Materials Properties Microstructure and Processing*, Vol. 415, No.1-2, 2006, p. 1-11.

16.   V. Srinivasan, A Critical Assessment of In-Flight Particle State During Plasma Spraying of YSZ and its Implications on Coating Properties and Process Reliability, *Ph. D Thesis, State University of New York at Stony Brook*, 2007.

17.   A. Kulkarni, On the Porosity-Property Correlations in Thermal-Structural Coatings:Towards an Intergrated Approach, *Ph. D Thesis, State University of New York at Stony Brook*, 2002.
vanced Engineering Materials, Vol. 3, No.7, 2001, p. 465-468.

18.   J. C. Maxwell, A treatise on electricity and magnetism, Dover, New York, 3rd edn, Chap.9, 1954, p. 1.

19.   P. G. Klemens, *High Temps. - High Press.*, Vol. 23, 1991, p. 241.

20.   L. Pawlowski and P. Fauchais, Thermal transport properties of thermally sprayed coatings, *International Materials Reviews*, Vol. 37, No.6, 1992, p. 271-290.

21.   K. W. Schlichting, N. P. Padture and P. G. Klemens, Thermal conductivity of dense and porous yttria-stabilized zirconia, *Journal of Materials Science*, Vol. 36, No.12, 2001, p. 3003-3010.

22.	R. W. Trice, Y. J. Su, J. R. Mawdsley, K. T. Faber, A. R. De Arellano-Lopez, H. Wang and W. D. Porter, Effect of heat treatment on phase stability, microstructure, and thermal conductivity of plasma-sprayed YSZ, *Journal of Materials Science*, Vol. 37, No.11, 2002, p. 2359-2365.

23.	H. Wang and R. B. Dinwiddie, Characterization of thermal barrier coatings using thermal methods, *Advanced Engineering Materials*, Vol. 3, No.7, 2001, p. 465-468.

Chapter 5.

Development in Microstructural Characterization of Plasma Sprayed Coatings as well as its Application to Microstructure and Thermal Transport Property Correlations of As-Sprayed and Thermal Aged YSZ Coatings

5.1 Introduction

YSZ coatings, due to the lower thermal conductivity, have long been used as insulation to metallic components, which increase the operating temperature with consequent improvements in efficiency or reduce requirement of cooling and prolong the component durability and life extension [1, 2]. It is difficult to establish structure–property relationships in plasma sprayed coatings because of the unique and intermingled splat microstructures, namely, the incorporating networks of various intrinsic process-dependent micro-defects. Quantitative microstructure characterization for better understanding of microstructure-property correlations is of considerable interest in plasma sprayed coating research.

There have been many studies aimed at understanding the effect of these microstructural defects, porosity in particular, on the thermal conductivity of plasma sprayed YSZ coatings [3]. Some early theoretical treatment was given by Maxwell [4], which related effective conductivity of the porous materials to total porosity. However, total porosity does not fully capture the anisotropic pore features and associated abnormal variations of the thermal transport property by using this Maxwell Model. Recent development of microstructure characterization promoted the qualitative and quantitative investigation of microstructure features (surface area, porosity, pore morphology and orientation) as well as the relation of each microstructural feature to thermal transport property of coatings [5, 6]. The important role of interlamellar porosity in both room temperate and temperature dependent thermal conductivity was pointed out and the effective contribution of different morphology pores on thermal conductivity was also investigated [7-9]. Despite the long observation and concern regarding porosity issues,

the variation of the thermal conductivity still needs to be interpreted from many aspects, such as the morphology and amount of pores, which brings out the difficulty of establishing microstructure-property relationships. There appears to be no unified, yet practical, parameter that is suitable to be used to define microstructural defects just as a second phase regardless of their geometry features to determine the effects on thermal physical properties. It becomes necessary to determine or establish such a microstructural parameter. In this dissertation, all the various morphology porosities are unified to one single microstructural parameter named "effective porosity" for better understanding of microstructure-thermal transport property relationships according to the heat resistance principle since all the different morphology pores play the role in essence as a second phase.

Besides the complexity of coating microstructure, the dynamic evolution of microstructure and property during service offers a significant challenge in the microstructural characterization and the investigation of structure-property relationship as well as the life prediction. The application temperatures of YSZ coatings used as thermal barrier coatings (TBCs) are generally above 1000^oC. [10]. Such high temperature leads to the sintering and densification, which will further change the microstructure and thermal transport property [10]. Consequently, the effectiveness of the TBCs is reduced. This decreasing thermal protection of the TBCs mainly results from two factors: a time-at-temperature component and a cycle-frequency component. Both components give rise to significant microstructural changes [11-14] and thus the thermal conductivity variations. Substantive studies simulating the mechanical system in operation have been performed to understand the effects of these two components. Wang et al. [8] and Trice et al. [15] have found that both of the components can improve the splats contact and result in the closure of interlamellar pores, which elevates thermal conductivity [7, 8]. Unfortunately, quantitative correlation between thermal conductivity and microstructural defects for annealed coatings is still limited. Thus, many questions remain unanswered.

This dissertation attempts to unify all the various morphology porosities to one single microstructural parameter named "effective porosity" for better understanding of microstructure-thermal transport property relationships according to the heat resistance principle. This new microstructural parameter is used for microstructural characterization of both as-sprayed and thermal aged YSZ coatings. The measured microstructural defects (i.e. total porosity and interlamellar porosity) are compared with the effective porosity for examining the effectiveness of this new parameter on microstructure-property relationship. The thermal cycling and isothermal annealing are also studied to observe their effects on microstructure and thus thermal conductivity. An inverse linear model and a percolation model are established to predict the microstructure-thermal conductivity relationship for as-sprayed and thermal aged coatings. These investigations would improve our current understanding of the microstructure-thermal transport property relationship.

5.2 Experiment

YSZ feedstock powders of three morphologies nominally with similar size were used to make TBCs: hollow sphere (HOSP, 27-95μm, d50=60μm), agglomerated and sintered (AS, 27-97μm, d50=55μm) and fused and crushed (FC, 31-97 μm, d50=64 μm). 20 images of each sample were taken by Nikon Epiphot 200 optical microscopy at 200x (1315×1013 pixels). The microstructure was quantified using image analysis and complemented with Archimedes' method. By choosing a suitable threshold in a region where a small variation of that value generates large variations of the porosity, the gray scale (0-255 gray scales) images were converted into binary images, which give an indication of the total pores. Based on aspect ratio and direction, the total pores were categorized into interlamellar pores (aspect ratio less than 1/6, angle between this pore and horizontal line less than 45°) and globular pores (all the others). Free standing coating was obtained by grinding the substrate away to be 100~300μm and then bending substrate to detach the coating from it. Subsequently, the coating was rounded to be a disk with diameter 12.7mm and coated with graphite. Room temperature thermal conductivity through thickness was measured by Holometrix Laser Flash Instrument.

5.3 Results and Discussions

5.3.1 The Establishment of a New Microstructural Parameter "Effective Porosity"

The microstructure constituents of YSZ coatings include three types of pores: interlamellar pores (resulting from splat based layered coating build-up), microcracks (associated with relief of quenching stresses) and globular pores (arising from lack of complete filling) [7]. The dimension and morphology of these three components are different, which results in different role in heat conduction. Deshpande et al [8] analyzed the YSZ coating microstructure and obtained the thickness of globular pores in the size range 3-10μm, interlamellar pores 0.1-3 μm, and crack 0.01-0.5 μm. However, all the different morphology pores play the role as a second phase-air in essence. Sharma et al. [16] have successfully established highly simplified two-phase representation of the coating by treating the coating as *matrix-air composite* to study the microstructure-electrical property relationship. In this study, the two phase model is developed to reexamine the microstructure-thermal transport property relationship. The role of different morphology pores in thermal conductivity decrease is explained from the different heat transport mechanism arising from the geometry shape. To analyze the effect of pore morphology on thermal conductivity, the different morphology pores are modeled as simple geometric figures. All the globular pores are described as spheres with diameter of D_g (Fig.5.1.(a)). Considering that it is not completely empty between two

splats and there is imperfect contact, the disk model is not suitable for interlamellar pores here. The interlamellar pore is approximated as a roll of cylinders (roller model). The diameter of the unit cylinder is D_{inter} and the length is L_{inter} (Fig.5.1. (b)). The vertical cracks are treated as disks with diameter of Dc and length of Lc (Fig.5.1. (c)). The direction of heat flux is perpendicular to the cylinder axes for both interlamellar pores and vertical cracks.

(a)   (b)   (c)
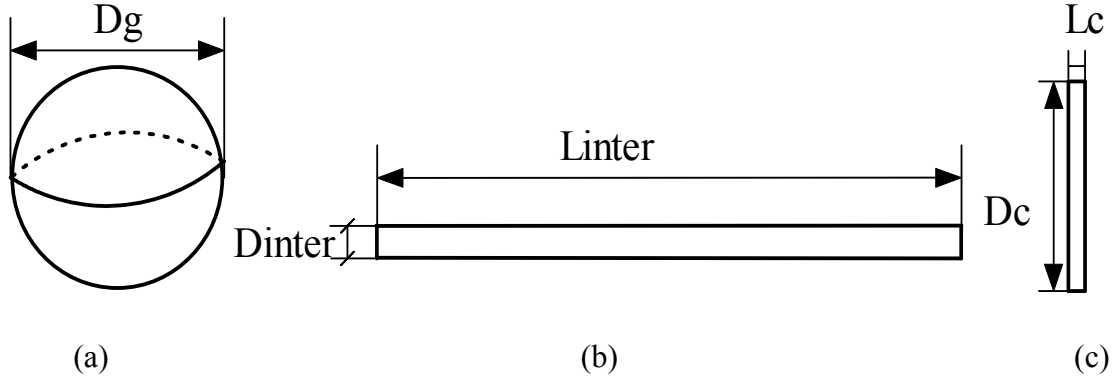
Figure 5.1 The shape approximation of the different morphology pores in plasma sprayed YSZ coatings (a) globular pores (b) interlamellar pores (c) vertical cracks

Loeb [17] investigated the effective thermal conductivity of porous materials and a theory was presented relating the effective conductivity to the amount, size and shape of pores. It was assumed that the heat flow is unidirectional and the pores do not disturb the unidirectionality. According to this theory, the thermal conductivity of globular pores (Kg), interlamelar pores (Kinter), and vertical cracks (Kc) can be expressed as:

$$Kg = \frac{8}{3} D_g \varepsilon \sigma T^3 \tag{1}$$

$$K_{inter} = \pi D_{inter} \varepsilon \sigma T^3 \tag{2}$$

$$Kc = \pi D_c \varepsilon \sigma T^3 \tag{3}$$

ε-emissivity, σ-Boltzmann constant, T-temperature

The volumes of these three morphology pores are:

$$Vg = \frac{4}{3} \pi (\frac{Dg}{2})^3 \tag{4}$$

$$V_{inter} = \pi (\frac{D_{inter}}{2})^2 L_{inter} \; (\text{Generally, Dinter=1/500~1/5Linter}) \tag{5}$$

$$Vc = \pi (\frac{Dc}{2})^2 Lc \; (\text{Generally, Dc=10~50Lc}) \tag{6}$$

65

If the three morphology pores have the same volume, the relationships between the diameters of different morphology pores should be

$$D_{inter} = 0.1 \sim 0.5\ D_g \tag{7}$$
$$D_c = 1.9 \sim 3.2\ D_g \tag{8}$$

And the relationships between thermal conductivities of different morphology pores are

$$K_{inter} = 0.12 \sim 0.6 K_g \tag{9}$$
$$K_g/K_{inter} = 1.7 \sim 8.3 \tag{10}$$
$$K_c = 2.2 \sim 3.8 K_g \tag{11}$$

The vertical cracks inside the splats have a minor influence on the effective thermal conductivity as the direction goes roughly parallel to the heat flow line and only a relatively small number of flow lines pass through the vertical cracks [17]. In this study, the effect of vertical cracks on thermal conductivity through thickness is simplified by treating cracks as globular pores. This consideration is also due to the limited resolution of images underestimated the amount of cracks. Interlamellar pores and globular pores have different magnitude of effect on thermal conductivity. The interlamellar pores which are mostly oriented perpendicular to the thermal gradient can significantly lower the heat flow through thickness than globular pores. The reason is that the heat flow must pass through the pore plane and therefore the effect of interlamellar pores is much greater. Despite the larger decrease of thermal conductivity resulting from the same volume interlamellar pores, the globular pores [9] account for the substantive fraction of microstructural defects in YSZ coatings. Therefore, both interlamellar pores and globular pores are the main factors of thermal conductivity reduction.

Complex relationship between thermal conductivity and different morphology porosities was observed [9], which is consistent with the model above. However, we were not able to simply use these component porosities to determine their relation to thermal conductivity in the previous study. The continuous needs for microstructural definition and microstructure-property relationship are desirable. A factor is demanded to combine the different morphology pores. Accordingly, a new parameter P_E, "effective porosity", is introduced to characterize the microstrutural defects and establish the relationship to the thermal transport property. The new parameter is a function of interlamellar porosity and globular porosity. The definition of P_E is shown as

$$P_E = A*I + G \tag{12}$$

where P_E is effective porosity, I is interlamellar porosity, G is globular porosity and A is a weighting coefficient. It is assumed that thermal conductivity is inversely linear to effective porosity as $K = b - c\ (A*I + G)$. By inputting the thermal conductivity, interlamellar porosity and globular porosity of the YSZ coatings made of three morphology powders, we get

$$1 = b - c\ (3.3A + 17.7) \tag{13}$$
$$1.18 = b - c\ (1.7A + 23.3) \tag{14}$$
$$1.3 = b - c\ (2.1A + 17.9) \tag{15}$$

From these relationships, it is found that the weighting coefficient A ~ 4, which means the same volume interlamellar pores play as a role in heat impedance four times as high as the globular pores. Compared with the equation (10), the value of A is in the range.

The equivalent porosities calculated using A=4 and the thermal conductivities of YSZ coatings made of three different morphology powders are used to develop relationship among them. Figure 5.2 shows the relation between thermal conductivity vs. interlamellar, total and equivalent porosities. The relation between thermal conductivity and total porosity as well as interlamelllar porosity appears complex in Fig. 5.2. However, inverse linear dependence of thermal conductivity is observed with respect to the effective porosity. The adoption of effective porosity simplifies the characterization of microstructural defects and the microstructure-thermal conductivity relationship appears clear. Therefore, the effective porosity is a suitable parameter to link the microstructural defects and thermal conductivity for these YSZ coatings with complex microstructure.
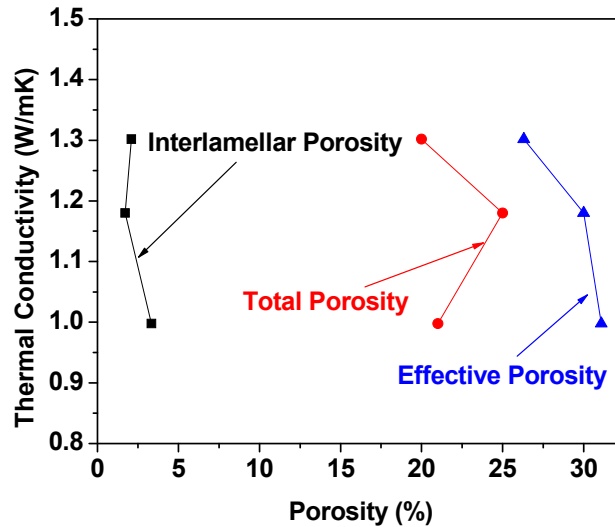
Figure 5.2 Relation between thermal conductivity and different porosities

5.3.2 The Application of Effective Porosity for Thermal Aged Samples

Plasma sprayed YSZ coatings have long been used in high temperature environment as TBCs. The complex changes in their structure and properties occur under operation condition and lead to their failure. This failure of the TBCs mainly results from two factors: a time-at-temperature component and a cycle-frequency component. In order to understand the effect of these two components on coating microstructure and thermal conductivity, studies were performed for thermal cycled and isothermal annealed YSZ coatings made of three different morphology powders. The thermal cycling experiments involved subjecting freestanding deposits to 20 cycles of heating at 1100 °C

for 30 minutes followed by cooling at room temperature for 15 minutes. The isothermal exposure of APS coatings at 1200°C for 200h was carried out in collaboration with Siemens Westinghouse Powder Corporation (SWPC), Orlando, FL. The quantitative information of thermal conductivity increase is shown in Fig. 5.3. The effects of thermal aging on thermal conductivity in principle are quantified by comparing the results of as-sprayed, thermal cycled and isothermal annealing coatings. The higher thermal conductivity of as-sprayed coatings results in higher thermal conductivity of thermal aged coatings. The increases in the thermal conductivity after thermal cycling and isothermal annealing result from the change in shape of planar pores and reduced porosity due to sintering. For the effect of isothermal annealing, Trice et al. [69] also observed a distinct change in the interlamellar pores by TEM analysis for the coatings after the 50-hour/1200°C heat treatment, which conforms to our results. For the effect of thermal cycyling, Z. Wang et al[8] have exploited SANS to characterize the microstructure of as-sprayed and thermal cycled (10 cycles) YSZ coatings at the same thermal cycling condition as that of this study. The consistent results were found for the elimination of splat-splat interfaces and the increase of thermal conductivity. The USAXS studies [18] were carried out and they showed that the larger interlamellar pores tended to decrease open dimension even if they were not completely closed after thermal cycling. Kulkarni et al [18] observed the evidence of sintering of globular pores for thermal cycled coatings using XMT.

In this study, IA and Archimedes' method are adopted and the porosities obtained by these two methods for as sprayed and thermal aged coatings are shown in Table 5.1. The total porosities measured by IA and Archimedes' method are very close, which confirms the reliability of the microstructural characterization. To examine the effect of the sintering quantitatively, the new parameter "effective porosity" is introduced. The effective porosity is obtained according to A=4. The increase of thermal conductivity of YSZ coatings can be interpreted by the decrease of effective porosity. Compared with thermal cycling, isothermal annealing has more contribution to thermal conductivity increase. This is because isothermal annealing has higher temperature (1200°C) and longer time (200h) than thermal cycling with total 10 hours heating for 20 cycles at 1100°C. More change of effective porosity happens after isothermal annealing than thermal cycling. The two thermal aged conditions simulate the mechanical system in operations although the factors of temperature and time are different. The same heating temperature-time thermal aging for thermal cycling and isothermal annealing is underway and will be discussed in the Chapter 6. The thermal conductivities and calculated equivalent porosities of as-sprayed and thermal aged YSZ coatings are used to plot as shown in Fig. 5.4. Linear fit is performed and a linear equation is obtained

$$K=3.95-0.099P_e \tag{16}$$

From Fig. 5.4, it can be observed that the deviations from the expected trend line are significant for some points. From the equation 16 obtained from the linear fit, we are able to predict that the thermal conductivity should be zero when P_e=40%. But the experimental results show that the thermal conductivity is around 0.7W/mK for the YSZ coatings with P_e=40%. The inverse linear model is not perfect to describe the microstructure-thermal conductivity relationship. This model only can quantitatively clarify the relationship between microstrutural defects and thermal conductivity well in a certain range due to the limitation of the inverse linear assumption.

It is widely appreciated that percolation theory has been successful in interpreting the conductor-insulator networks of porous materials. The percolation theory is used to elucidate the microstructure-thermal conductivity relationship of both as-sprayed and thermal aged TBCs since the main role of sintering is to open new percolation paths which make heat flow easier. This is the first time to introduce percolation theory for the study of microstructure-thermal conductivity relationship and sintering effect of TBCs. After the thermal aging, the islands were formed to generate more true contacts between splats and therefore shorten the length of interlamellar pores, which increases the thermal conductivity significantly. By using percolation theory, we have observed that the normalized thermal conductivity obeys a power law relationship to equivalent YSZ volume fraction ($V = 1 - P_E$) as shown in Fig. 5.5

$$Kc/Kb = a(V - Vc)^n \qquad\qquad\qquad (17)$$

Kc and Kb are thermal conductivity of coating and bulk. The value of the critical exponent obtained in this case is $n = 4.5$ and the percolation threshold is $Vc = 0.03$. The critical exponent $n = 4.5$ is larger than the universal critical exponent (1.1~2.1 for 2D and 1~4 for 3D) due to the anisotropy. The behavior of the conductance as a function of percent conductor appears qualitatively changed. For two-dimensional conductor-insulator networks, Lobb, Skocpol , and Tinkham [19] and Tinkham [20] have reported electrical-receptivity measurements on a system consisting of superconducting niobium filaments imbedded in a copper matrix, and obtained a critical exponent $s = 1.05$, which is higher than the value $0.5 < s < 0.9$ [21] due to the highly anisotropic nature of their system. Experimental work on 3D continuum systems, however, often results in values for critical exponent higher than those obtained from numerical simulation of lattice networks. Deptuck et al [22] found that the percolation threshold of volume fraction is at 0.062 ± 0.01. The critical exponents for a three-dimensional percolation system comprised of sintered, submicron, silver power are 2.15 ± 0.25 and $T = 3.8 \pm 0.5$, in agreement with recent theories and numerical simulations that show $T > t$, $1.65 < t < 2.2$, and $T > 3.55$.
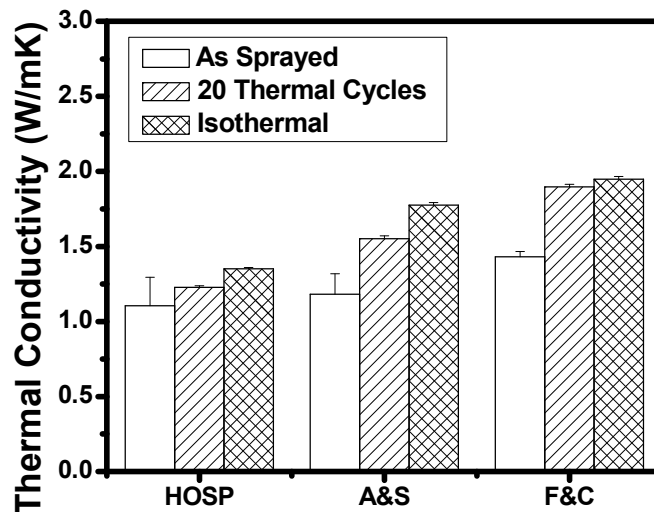
Figure 5.3 Effect of thermal aging on room temperature thermal conductivities of coatings made of different morphology powders

Table 5.1 Porosities of YSZ Coatings

Techniques	Archimedes' Method	Image Analysis			
Coatings	Total Porosity (%)	Total Porosity (%)	Interlamellar Porosity (%)	Globular Porosity (%)	Effective Porosity (%)
HOSP-as sprayed	18.5	21	3.3	17.7	31
HOSP-20 thermal cycles	17.9	18.8	3.1	15.7	28.1
HOSP-isothermal annealing	16.7	17.2	2.9	14.3	25.9
A&S-as sprayed	22	25	1.7	23.3	30
A&S-20 thermal cycles	20	20.8	1.6	19.2	25.6
A&S-isothermal annealing	18.9	18.0	1.5	16.5	22.5
F&C-as sprayed	16.8	20	2.1	17.9	26.3
F&C-20 thermal cycles	16.2	15.9	1.8	14.1	21.3
F&C-isothermal annealing	14.9	15.3	1.8	13.5	20.7

$K=3.95-0.099Pe$
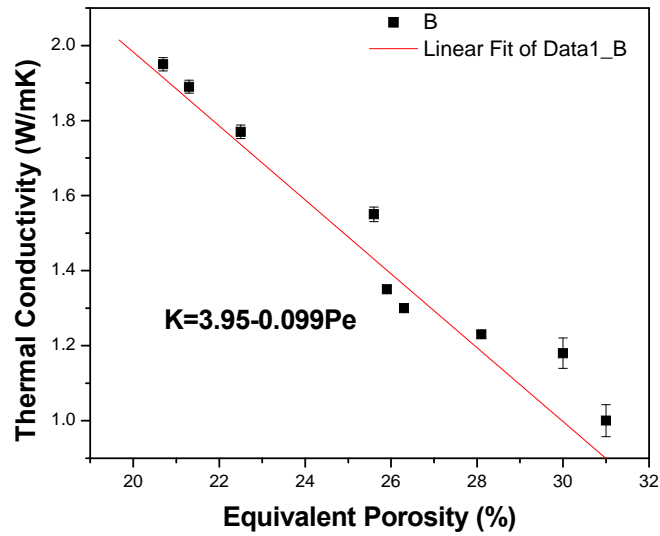
Figure 5.4 Relation between thermal conductivity and effective porosity

In order to confirm the validity of the models for as-sprayed and thermal aged YSZ coatings, the P_E are calculated using the equation 16 and 17 as well as compared with the

P_E obtained from definition (A=4). All the results are listed in Table 5.2. The equivalent porosities obtained from linear fit (P_{EL}) and percolation model (P_{EP}) both are close to the one calculated from definition (P_E). However, P_{EP} shows better match with P_E than P_{EL}. This indicates the prediction fidelity of percolation model for the relationship between the microstructural defects and thermal conductivity, which is suitable to be extended to the application of general YSZ coatings. This percolation model offers a new way to understand the microstructure-property relationship and determine the favorable structure for durability to design coatings.
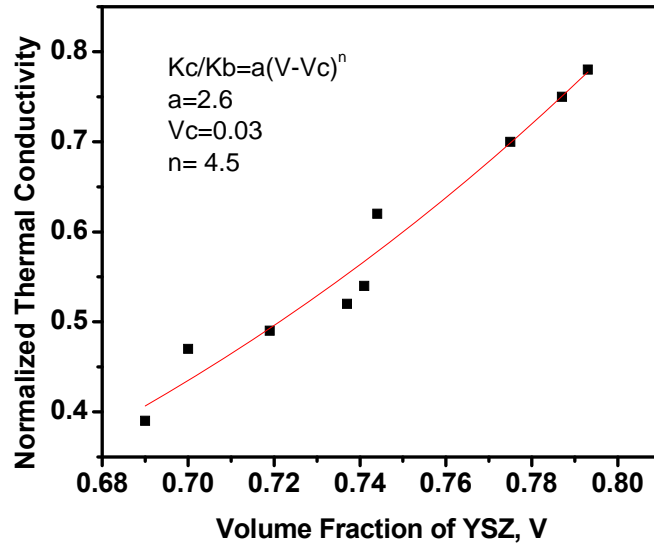
Figure 5.5 Normalized thermal conductivity as a function of volume fraction of YSZ

Table 5.2 Effective porosity of Coatings

Coating	P_E from definition (%)	P_{EL} (%)	P_{EP} (%)
HOSP-as sprayed	31	29.8	31
HOSP-20 thermal cycles	28.1	27.5	28
HOSP-isothermal annealing	25.9	26.3	26.5
A&S-as sprayed	30	28.0	28.6
A&S-20 thermal cycles	25.6	24.3	24.3
A&S-isothermal annealing	22.5	22.0	22.1
F&C-as sprayed	26.3	26.8	27
F&C-20 thermal cycles	21.3	20.8	21
F&C-isothermal annealing	20.7	20.2	20.5

5.4 Conclusions

This study quantifies, by means of image analysis, microstructural features (porosity and morphologies) of plasma sprayed YSZ coatings. The most important contribution is the establishment of the correlation between thermal conductivity and one single microstructural parameter "effective porosity", which combines the thermal impedance effects of pores with different shapes. This new parameter is applied to both as-sprayed and thermal aged coatings. Preliminary results show promise to interpret the relationship between microstructural defects and thermal conductivity using effective porosity with linear fit and percolation model. This study provides a framework to understand and control thermal transport properties of plasma sprayed TBCs with complex microstructure as well as explore the high temperature stability and sintering effects. The two proposed models can be used as predictive tools in industrial applications for quantitative estimate of the thermal conductivity change and failure after service. They potentially offer insights to improve engine durability, reliability and performance along with optimization of processing and maintance economics.

Some uncertainties about Loeb Theory are still not clear. The assumption for Loeb Theory is that the contribution of thermal conductance to thermal conductivity is zero through the pores. Thus, radiation becomes important. But it is well known that thermal conductivity of air at room temperature, 1atm is around 0.024W/mK. The thermal conductivity arising from radiation is only around $10^{-4} \sim 10^{-6}$W/mK, which can be neglected as compared to that arising from thermal conductance. There are some possible reasons: one is that the heat has a propensity to pass through the YSZ matrix, which has much higher thermal conductivity 2.5W/mK than air and decreases the air thermal conductivity further; the other is the thermal conductivity of air, 0.024W/mK, is not suitable to be used for the pores of coatings due to interface scattering. It is unclear as to the quantitative reduction of thermal conductance for the pores as compared to air at room temperature, 1atm. This requires further fundamental analysis in the future.

The proposed parameter "effective porosity" is still work in progress. Some microstructure features, i.e. directions of interlamellar pore and cracks, have not been considered. More detailed works are required to examine, confirm and improve this new concept.

References

1.   S. M. Meier and D. K. Gupta, The Evolution of Thermal Barrier Coatings in Gas-Turbine Engine Applications, *Journal of Engineering for Gas Turbines and Power-Transactions of the Asme*, Vol. 116, No.1, 1994, p. 250-257.

2.   R. A. Miller, Current Status of Thermal Barrier Coatings - an Overview, *Surface & Coatings Technology*, Vol. 30, No.1, 1987, p. 1-11.

3.   R. Mcpherson, A Model for the Thermal-Conductivity of Plasma-Sprayed Ceramic Coatings, *Thin Solid Films*, Vol. 112, No.1, 1984, p. 89-95.

4.   J. C. Maxwell, A treatise on electricity and magnetism, Dover, New York, 3rd edn, Chap.9, 1954, p. 1.

5.   J. Ilavsky, G. G. Long, A. J. Allen, H. Herman and C. C. Berndt, Use of small-angle neutron scattering for the characterization of anisotropic structures produced by thermal spraying, *Ceramics-Silikaty*, Vol. 42, No.3, 1998, p. 81-89.

6.   S. Sampath, X. Y. Jiang, J. Matejicek, L. Prchlik, A. Kulkarni and A. Vaidya, Role of thermal spray processing method on the microstructure, residual stress and properties of coatings: an integrated study for Ni-5 wt.%Al bond coats, *Materials Science and Engineering a-Structural Materials Properties Microstructure and Processing*, Vol. 364, No.1-2, 2004, p. 216-231.

7.   A. Kulkarni, Z. Wang, T. Nakamura, S. Sampath, A. Goland, H. Herman, J. Allen, J. Ilavsky, G. Long, J. Frahm and R. W. Steinbrech, Comprehensive microstructural characterization and predictive property modeling of plasma-sprayed zirconia coatings, *Acta Materialia*, Vol. 51, No.9, 2003, p. 2457-2475.

8.   Z. Wang, A. Kulkarni, S. Deshpande, T. Nakamura and H. Herman, Effects of pores and interfaces on effective properties of plasma sprayed zirconia coatings, *Acta Materialia*, Vol. 51, No.18, 2003, p. 5319-5334.

9.   W. Chi, S. Sampath and H. Wang, Ambient and High Temperature Thermal Conducitivity of Thermal Sprayed Coatings, *Proceedings of the 2006 International Thermal Spray Conference*, 2006, p. May 15-18,Seattle,WA,USA.

10.   H. Wang and R. B. Dinwiddie, Characterization of thermal barrier coatings using thermal methods, *Advanced Engineering Materials*, Vol. 3, No.7, 2001, p. 465-468.

11.   J. Gutleber, S. Usmani and S. Sampath, Processing and Thermal Cycling Effects on the Erosion Behavior of Thermal Barrier Coatings, *Thermal Spray: A United Forum for Scientific and Technological Advances, Ed: C. C. Berndt, ASM Int.*, 1997, p. 285-289.

12.   G. McDonald and R. C. Hendricks, Effect of Thermal Cycling on ZrO2-Y2O3 Thermal Barrier Coatings, *Thin Solid Films*, Vol. 73, 1980, p. 491-496.

13.   B. C. Wu, E. Chang, S. F. Chang and C. H. Chao, Thermal Cycling Response of yttria Stabilized Zirconia/CoNiCrAlY Thermal Barrier Coatings, *Thin Solid Films*, Vol. 172, 1989, p. 185-196.

14.   C. C. Berndt and H. Herman, Failure during Thermal Cycling of Plasma Sprayed Thermal Barrier Coatings, *Thin Solid Films*, Vol. 108, 1983, p. 427-437.

15.   R. W. Trice, Y. J. Su, J. R. Mawdsley, K. T. Faber, A. R. De Arellano-Lopez, H. Wang and W. D. Porter, Effect of heat treatment on phase stability, microstructure, and thermal conductivity of plasma-sprayed YSZ, *Journal of Materials Science*, Vol. 37, No.11, 2002, p. 2359-2365.

16.   A. Sharma, R. J. Gambino and S. Sampath, Electrical Conduction in Thermally Sprayed Thin Metallic Coatings, *in Surface Engineering for Manufacturing Applications, edited by W.J.Meng, R.Maboudian,S.C.Chen,S.J.Bull,P.R.Chalker,Mat.Res.Symp.Proc. 890*, 2006.

17.   A. L. Loeb, Thermal Conductivity .8. A Theory of Thermal Conductivity of Porous Materials, *Journal of the American Ceramic Society*, Vol. 37, No.2, 1954, p. 96-99.

18.   A. Kulkarni, On the Porosity-Property Correlations in Thermal-Structural Coatings:Towards an Intergrated Approach, *Ph. D Thesis, State University of New York at Stony Brook*, 2002.

19.   C. J. Lobb, M. Tinkham and W. J. Skocpol, Percolation in Inhomogeneous Superconducting Composite Wires, *Solid State Communications*, Vol. 27, No.12, 1978, p. 1273-1275.

20.   M. Tinkham, Electrical Transport and Optical Properties of Inhomgeneous Media, *edited by J.C. Garland and D.B. Tanner, AIP Conf. Proc.*, Vol. 40 (AIP, New York), 1978, p. 130.

21.   J. Bernasconi, Real-Space Renormalization of Bond-Disordered Conductance Lattices, *Physical Review B*, Vol. 18, No.5, 1978, p. 2185-2191.

22.   D. Deptuck, J. P. Harrison and P. Zawadzki, Measurement of Elasticity and Conductivity of a 3-Dimensional Percolation System, *Physical Review Letters*, Vol. 54, No.9, 1985, p. 913-916.

Chapter 6.

Microstructures and Properties of Metal, Alloy, Cermet and Ceramic Coatings Produced by Various Thermal Spray Processes

6.1 Introduction

The thermal transport properties of thermally sprayed coatings are dependent on both the nature of sprayed material and the defected microstructure (pores, cracks and interfaces). A range of materials are used to make coatings by the thermal spray technique to fulfill variegated functions such as corrosion resistance, wear resistance, thermal barriers, electrical insulation or conductive contact, and restoration. Besides intrinsic characteristics of the coating material, the performance of the coating is related to the type of thermal spray process and related parametric/deposition conditions. It is widely appreciated that the various available thermal spray techniques allow for tailoring coating microstructure, composition and thus the properties of coatings. In essence this represents the flexibility and expanded applicability of the process.

In this study, a range of materials are adopted for spraying coatings to examine their processing effects on coating microstructure and properties. They include single element metallic coatings (Ag, Cu, Al, Mo), Ni/Co based alloy coatings (Ni, Ni5Al, Ni20Cr, CoNiCrAlY, Inconel CoMoCrSi based Tribaloy^{TM} T-800) and cermet coatings (WC-Co, Mo-Mo$_2$C), functionally graded materials - FGM (NiCrAlY+YSZ, Ni+Al$_2$O$_3$), and ceramic coatings (Al$_2$O$_3$, YSZ). Their thermal transport properties are examined with considerations to process induced oxidation (in metals), phase structure (equilibrium or metastable), extrinsic microstructural defects (pores, cracks, interfaces) as well as intrinsic considerations such as valence electron, atomic structure and crystal structure. The effect of thermal spray techniques are also investigated for certain coating systems. All the fundamental studies for the above-mentioned coating systems are listed in Fig. 6.1.

Such an investigation will not only provide insights on the process-materials interactions but also so provide valuable information about the selection of materials for coating design.
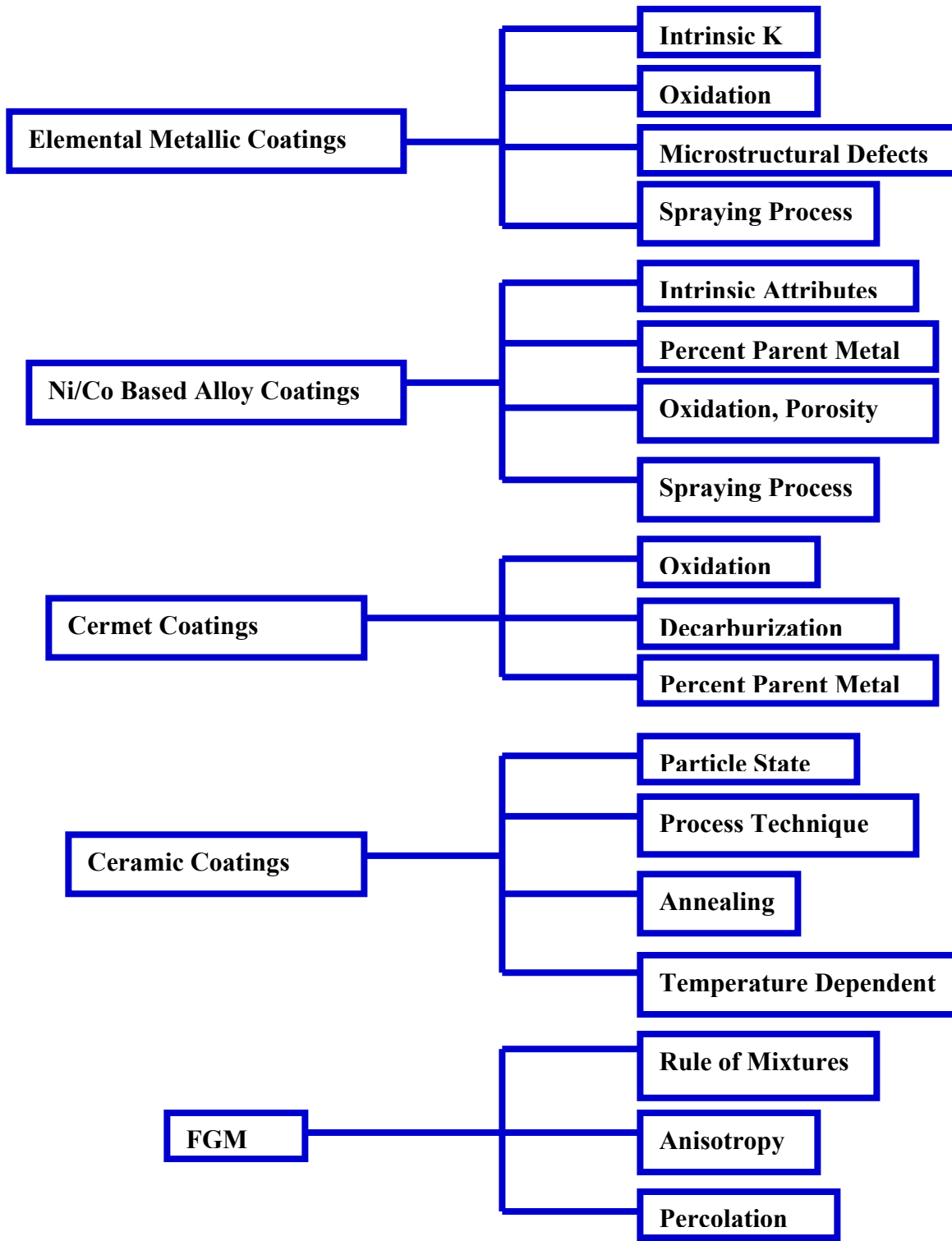
Figure 6.1 Fundamental study of different coating systems

6.2 Results and Discussion

6.2.1 Elemental Metallic Coatings

As a first step, a variety of single elemental metals (Ag, Cu, Al, Mo) have been selected to make coatings by different thermal spray technique (APS, HVOF and CS). The thermal conductivities were measured by laser flash techniques and the results are shown in Table 6.1. The table also shows the corresponding thermal conductivity of respective bulk alloy and the conductivity ratio. It can be seen that the thermal conductivity of bulk materials from the highest to the lowest is Ag>Cu>Al>Mo. The intrinsic attributes of materials will be introduced into coating systems.

Table 6.1 Thermal conductivity of single element metal bulks and coatings

Samples	Spray Technique	$K_{coating}$ (W/mK)	K_{bulk} (W/mK) (from Metals Handbook)	$K_{coating}/K_{bulk}$ (%)
Ag	APS	325 ± 15	430	75
Cu	HVOF	200 ± 10	400	50
Al	APS	96 ± 4	235	40
Al	HVOF	112 ± 3	235	50
Al	CS	170 ± 5	235	70
Mo	APS	14 ± 1	140	10

Figure 6.2 shows the effect of intrinsic attributes of single elemental metals on coating thermal conductivity. The thermally sprayed coatings made of these four metals follow the same sequence Ag>Cu>Al>Mo (Fig. 6.2 (a)) even though they have different decreased magnitudes compared to bulk values (Fig.6.2 (b)). Intrinsic thermal conductivity of bulk metal determines the coating thermal conductivity. In Fig. 6.2 (b), the thermal conductivity of Ag coating is reduced by 25% from bulk value, which is the smallest change compared with other metallic coatings. This is due to significantly reduced oxidation of this noble metal and also high effective coating density. The thermal conductivity of Mo coating is reduced by 90% from that of bulk despite the same process. This can be explained from the point of view of microstructure. Figure 6.3 shows the SEM images of the coating cross sections for APS Ag and Mo coatings. The bottom of the image is the section attached to the substrate. It can be clearly observed that the Ag coating displays a few short and small interlamellar pores only in the top section and some small globular pores distributed in the whole image whereas the Mo coating shows long and large interlamellar pores in the top section and long and small interlamellar pores in the bottom section. The higher ductility (44% EL in 50mm) of Ag also is favorable to reduce defects and form good contact between splats considering some incomplete melting particles. The Ag coating is densified by droplet impaction from the top except the section near the top, which leads to a little change of thermal conductivity from the bulk value. Compared with the Ag coating, the Mo coating has higher magnitude of disorder. On the top of cross-section of Mo coating, longer and larger

interlamellar pores exhibit and the splats have higher thickness; on the bottom of cross-section of image, the Mo coating includes interlamellar pores with smaller open dimension and therefore more interface number per unit thickness. This distribution of microstructural defects gives rise to the heterogeneous and disorder microstructure. Such a microstructure of APS Mo coating can cause significant phonon scattering in addition to electron scattering. The long interlamellar pores of the Mo coating also results in large depolarization factor of the slits. In addition, Mo coating experiences a significant oxidation during the spraying process. These combined effects can lead to a substantial reduction in effective thermal conductivity of Mo coating compared with bulk.
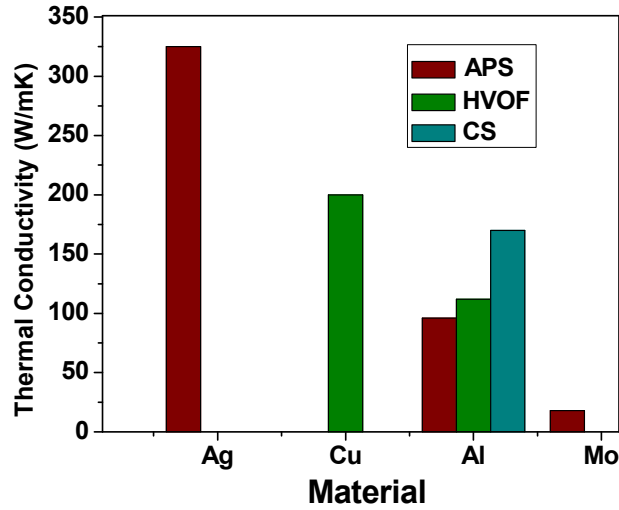
(a)
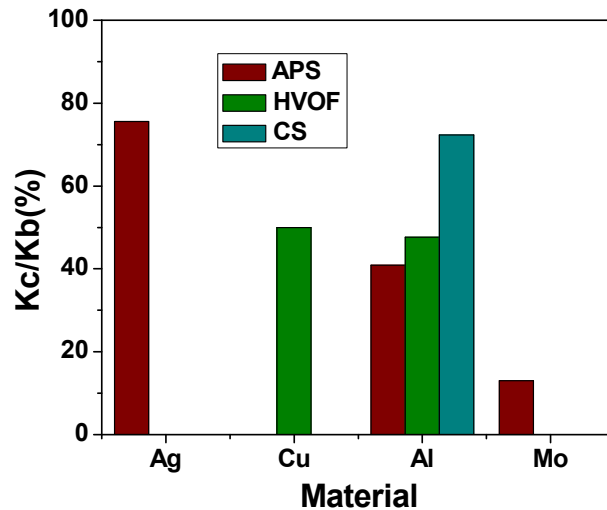
(b)

Figure 6.2 Effect of intrinsic attributes of materials on thermal transport property

(a) thermal conductivity (b) Kc/Kb
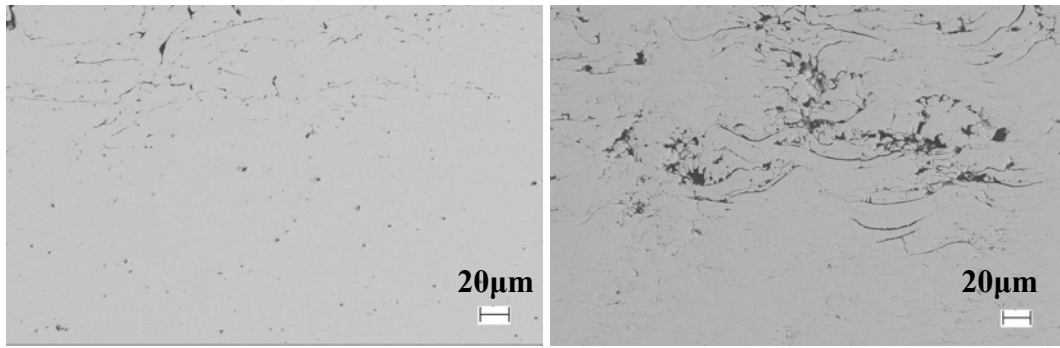
(a)	(b)

Figure 6.3 Images of cross-sections of elemental metallic coatings (a) Ag (b) Mo

Various thermal spray processes introduce different extent of chemical changes to the metallic material due to oxidation and also contribute to different extrinsic microstructural features (defects). Figure 6.4 focuses on examining the effect of spraying process on thermal conductivity of Al coatings. APS process has the highest particle temperature and the lowest particle velocity among the three processes (CS, HVOF and APS). The high particle temperature during APS promotes the oxidation and the lack of high velocity introduces significant porosity. The low particle velocity prolongs the dwell time of particle and also enhances the oxidation. The APS Al coating has lower thermal conductivity (therefore lower ratio of coating to bulk thermal conductivity) than the CS and HVOF Al coatings. The HVOF process has much higher temperature than the CS process. The higher temperature leads to more oxidation and lower thermal conductivity for the HVOF coatings. The thermal conductivity of CS Al coating is higher than that of HVOF Al coatings. Therefore, the thermal conductivity from highest to lowest is CS>HVOF>APS.

Another interesting observation about the important role of spraying possess is that the HVOF Cu coating has lower ratio of coating to bulk thermal conductivity despite higher absolute value of thermal conductivity than the CS Al coating, as shown in Fig. 6.2. This is also due to the much lower particle temperature in CS process and less oxidation. Thus, the CS Al coating has lower percentage reduction in thermal conductivity than the HVOF Cu coating. However, the lower intrinsic thermal conductivity of Al leads to lower absolute value of thermal conductivity of the CS Al coating.

The microstructural defects and oxidation arising from spraying process change the metallic coating density. Therefore, the thermal transport property of metallic coatings should be intimately related to their density. To examine the effect of the density change on thermal conductivity, preliminary study has been carried out for single elemental metallic coatings and the results are shown in Fig. 6.5. It can be observed that thermal conductivity linearly decreases with the reduction of coating density from the bulk density. Although the Ni-coatings were not discussed above, they follow the linear decrease well with the change of density. Details about process-microstructure-property relationship will be interpreted in the following section.

Figure 6.4 Effect of process on thermal conductivity of Al coatings

Figure 6.5 Thermal conductivity vs. density for various metal bulks and coatings

6.2.2 Ni and Co Based Alloy Coatings

Thermally sprayed Ni-based and Co-based alloy coatings are widely used for providing oxidation protection or in the form of bond coats serving as part of a duplex thermal barrier coating and other wear-, high temperature- a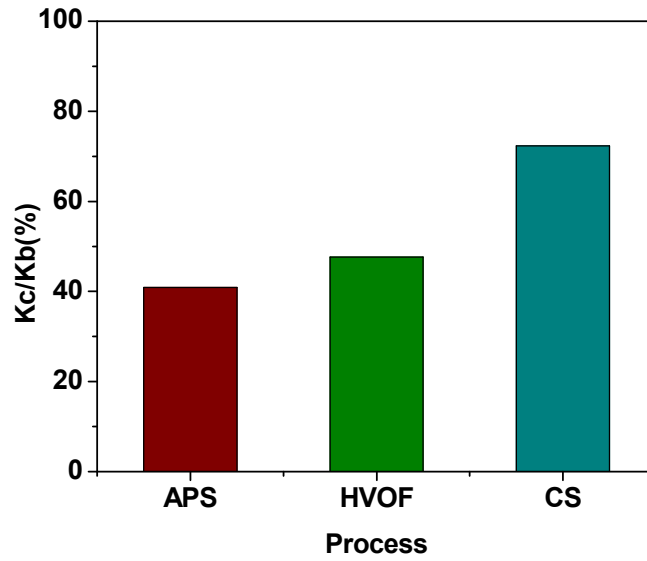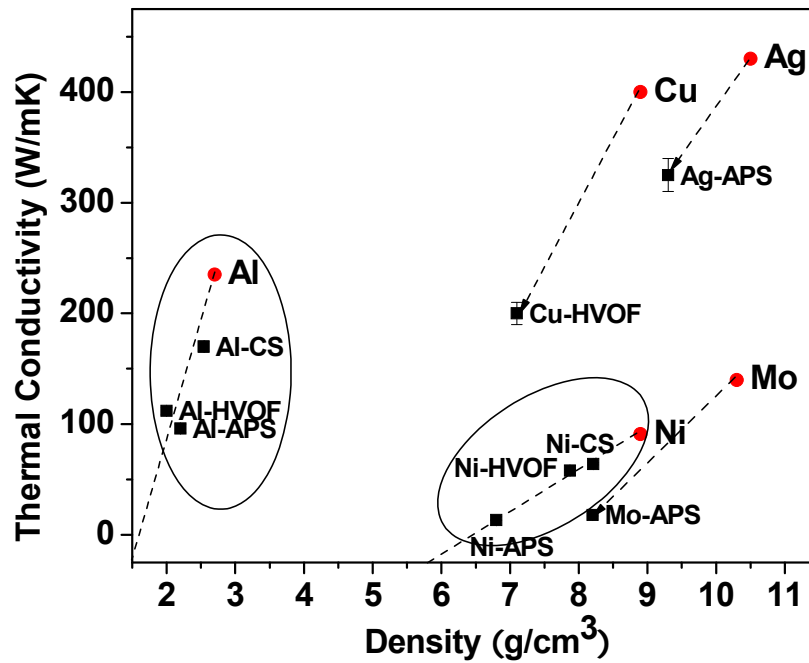nd corrosion-resistant surfaces [1]. Experiments have been carried out to examine the thermal transport properties of Ni, Ni-5Al, Ni20Cr and CoNiCrAlY coatings made by APS, HVOF and CS. In addition, inconel 718 coating and Tribaloy T-800 coatings (low oxide and high oxide) made by liquid fuel HVOF process (Praxair / Tafa JP 5000) were also explored.

6.2.2.1 Effect of alloy content on thermal conductivity

All the thermal conductivity results of these alloy coatings measured by the laser flash technique are listed in Table 6.2. The thermal conductivity values of the single element metals present in the above-mentioned coating systems are shown in Table 6.3. The thermal conductivities of bulk alloys were obtained from Metals Handbook.

It is observed that the APS Ni-5wt%Al coating has higher thermal conductivity than APS Ni coating. This is because the high particle temperature in APS process results in significant oxidation of Ni in Ni coating but less oxidation of Ni in Ni-5wt%Al coating since Al acts as a sacrificial getter for the oxygen and most Ni escapes from oxidation and the Ni-5wt%Al coating retains significant free electrons. Hence, the thermal conductivity of APS Ni-5wt% Al alloy coating is higher than that of APS Ni coating.

However, the thermal conductivity of HVOF Ni coating is much higher than that of HVOF Ni5Al coating. The HVOF process has lower particle temperature and reduces the oxidation of Ni significantly. Thus, HVOF Ni coating preserves a great deal of metallic phase. But in HVOF Ni-5wt% Al alloy, Al is still susceptible to oxidation. A significant amount of Al_2O_3 generates at the interfaces between the splats and thus the HVOF Ni5Al coating is still a composite coating. The Al_2O_3 has much lower thermal conductivity than Al and also acts as impurity atoms and thereby scattering centers in HVOF Ni-5wt% Al. The impurity atoms lower the efficiency of electron motion because they are not identical to the host atoms and result in a local distortion of the crystal lattice, either by pushing the host atoms farther away or pulling them in. The electrons are subject to a force $F = \dfrac{-d(PE)}{dx}$ due to a sharp variation of potential energy in the distorted region. Thus, the impurity atoms induce the discontinuity in the crystal orientation, extend a number of atomic distances, scatter the electron motion and decrease the conductivity.

The thermal conductivity of Cr is close to that of Ni. But the APS NiCr coating has a somewhat lower thermal conductivity than the APS Ni coating whereas the thermal conductivity of the HVOF NiCr coating is significantly lower than that of the HVOF Ni coating. There are two important reasons for the discrepancy. On the one hand, the Cr atoms distort the crystal lattice, hinder the electrons motion, reduce the mean free path from 10^{-7}m in pure metal to atomic dimension (10^{-10}m) and reduce the thermal conductivity for both APS and HVOF coatings. On the other hand, the HVOF Ni coating includes a little oxide whereas much more oxide exhibits in the APS Ni coating (confirmed by EDS analysis). However, the oxide in the HVOF NiCr coating is not trivial

due to selective oxidation of Cr and formation of Cr_2O_3 at the interfaces although the HVOF NiCr coating has less oxide than the APS NiCr coating. Therefore, thermal conductivity of the APS NiCr coating is a somewhat lower than that of the APS Ni coating and the HVOF NiCr coating has much lower thermal conductivity than the HVOF Ni coating

With the further alloying with more elements (CoNiCrAlY), the thermal conductivity of coatings trends lower. In Fig. 6.6 (a), for HVOF coatings, the thermal conductivity from the highest to the lowest is Ni> Ni5Al> Ni20Cr> CoNiCrAlY; for APS coatings, the thermal conductivity from the highest to the lowest is Ni5Al> Ni > Ni20Cr> CoNiCrAlY. To understand the reason for the sequences, the percentage of parent metal (Ni for Ni, NiAl and NiCr coatings and Ni+Co for CoNiCrAlY coatings) of powders was calculated and plotted against thermal conductivity for both HVOF and APS coatings in Fig. 6.6 (b) and (c), respectively. It is observed in Fig. 6.6 (b) that with the increase of the types of alloying elements, the percentage of parent metal decreases significantly and therefore the thermal conductivity of HVOF coatings drops sharply. In Fig. 6.6 (c), the change of thermal conductivity of APS coatings with parent metal percent is similar to that of HVOF coatings except that the Ni5Al APS coating has higher thermal conductivity than the Ni APS coating owing to the role of Al as a sacrificial getter for the oxygen. However, most coatings display the reduction with the decrease of parent metal percent. The starting percentage of parent metal significantly affects the thermal conductivity of thermally sprayed coatings. And the HVOF Ni-based alloy coatings have less oxidation as compared to the APS coatings, therefore, the effect of starting percentage of parent metal on thermal conductivity are more dominant in the case of HVOF Ni-based alloy coatings. That is, in the case of HVOF coatings, the thermal conductivity is dominated by intrinsic differences since the density of the coating is near theoretical value; in the case of APS coatings, the heterogeneous structure having many morphological defects as well as oxidation results in much more complex thermal transport mechanism.

Table 6.2 Thermal conductivity of Ni-based and Co-based thermally sprayed coatings

Samples	Spray Technique	$K_{coating}$ (W/mK)	K_{bulk}(W/mK) (Metal Handbook)	Kc/Kb (%)
Ni	APS	13.3±0.1	91	15
Ni	HVOF	58±1	91	64
Ni	CS	64±1	91	70
Ni-5wt%Al	APS	17.1±0.2	45	38
Ni-5wt%Al	HVOF	22.2±0.2	45	49
Ni-5wt%Al	CS	11	45	24
Ni-20wt%Cr	APS	12±1	18	67
Ni-20wt%Cr	HVOF	9±0.5	18	50
CoNiCrAlY	APS	3.4±0.1	15	22
CoNiCrAlY	HVOF	7.8±0.1	15	52
T-800 Low Oxide	Liquid Fuel HVOF	3.80±0.06	14.3	27
T-800 High Oxide	Liquid Fuel HVOF	2.53±0.04	14.3	18
In 718	Liquid Fuel HVOF	6.1±0.1	11.4	54

Table 6.3 Thermal conductivity of elements

Elements	K (W/mK) (from Metals Handbook)	Elements	K (W/mK) (from Metals Handbook)
Ni	91	Fe	80
Cr	94	Mo	140
Al	235	Nb	54
Y	17	Ti	22
Co	100	Si	150

The data for the effect of alloy elements on the coating thermal conductivity
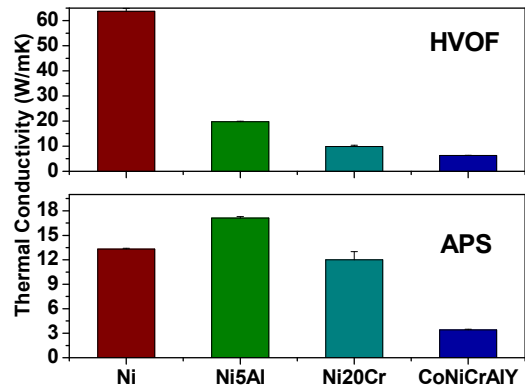
(a)
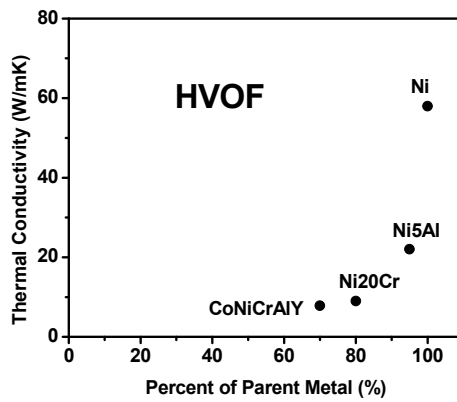
(b)
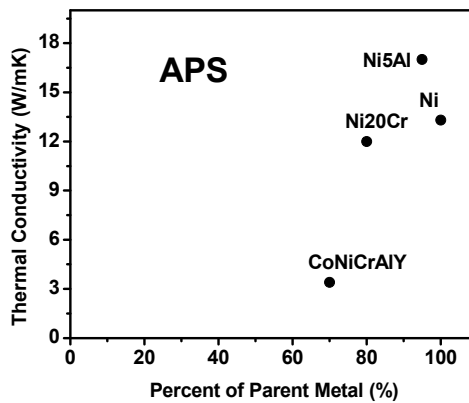
(c)

Figure 6.6 (a) The effect of intrinsic characteristics of materials on thermal conductivity (b) Thermal conductivity vs. percent parent metal of HVOF coatings (c)Thermal conductivity vs. percent parent metal of APS coatings

6.2.2.2 Effect of process on thermal conductivity of Ni and Co based alloy coatings

The characteristics of different spraying process determine the thermal conductivity of Ni and Co based alloy coatings. The process effect on thermal conductivity of Ni, Ni5Al, Ni20Cr and CoNiCrAlY coatings are examined in this study.

Figure 6.7 shows the cross-sections of Ni coatings made by APS, HVOF and CS. The thermal conductivity of the three coatings is displayed in Fig. 6.8. For Ni coatings, thermal conductivity follows APS<HVOF<CS. This is consistent with earlier findings about the single elemental metallic Al coatings made by APS, HVOF and CS. The more microstructural defects observed in the APS Ni coating (Fig. 6.7 (a)) and the more oxidation generated from APS process lead to much lower thermal conductivity. The extremely high velocities of CS and HVOF shorten the dwell time of particle, reduce the oxidation and decrease the porosity. The lower particle temperature of CS process reduces more oxidation than HVOF and results in higher coating thermal conductivity.

| (a) | (b) | (c) |

Figure 6.7 Images of cross-sections of Ni coatings made by different spraying techniques

(a) APS (b) HVOF (c) CS
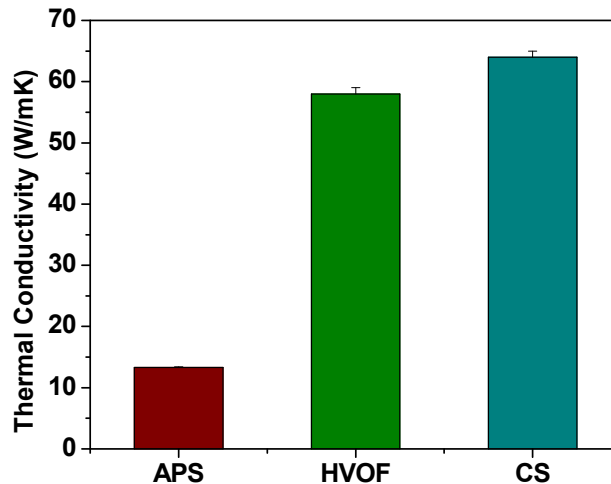
Figure 6.8 Thermal conductivity of Ni coatings made by different spraying techniques

The cross-section images and thermal conductivity for Ni5Al coatings made by APS, HVOF and CS are shown in Fig. 6.9 and 6.10. The high oxidation of APS Ni5Al coating leads to lower thermal conductivity as compared to HVOF Ni5Al coating. The CS Ni5Al coating has the lowest thermal conductivity, which shows an interesting abnormality. This is because the Ni5Al powder includes some oxide and the true contact between intersplats has a low degree. Thus, the CS Ni5Al coating consists of a network of fine interconnected inter-particle separations and the thermal conductivity is dramatically reduced despite low porosity and small oxide content.

(a)   (b)
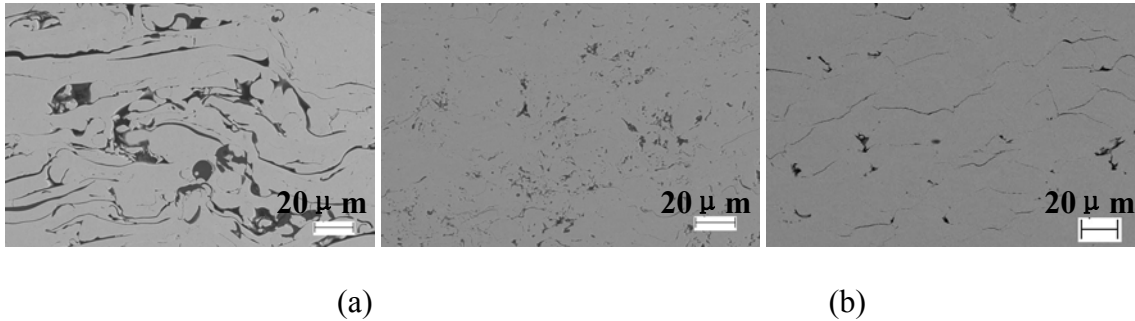
Figure 6.9 Cross-sections of Ni5Al coatings made by different spraying techniques

(a) APS (b) HVOF (c) CS
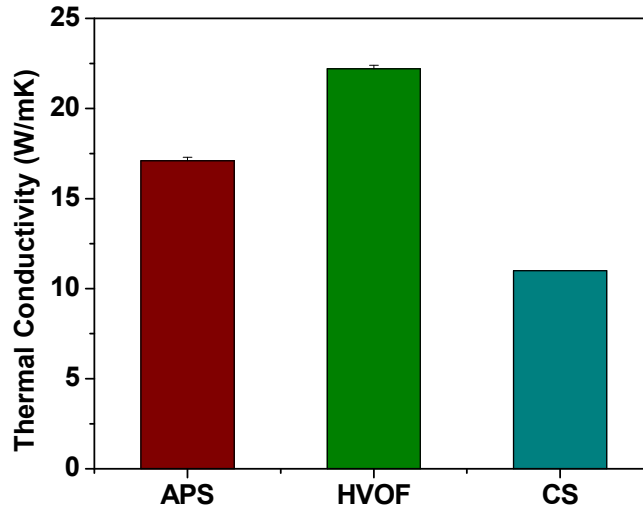
Figure 6.10 Thermal conductivity of Ni5Al coatings made by APS and HVOF

The cross-section images and thermal conductivity for Ni20Cr coatings and CoNiCrAlY coatings made by APS and HVOF are shown in Fig. 6.11, 6.12, 6.13 and 6.14. In the case of NiCr coatings, the HVOF process produces lower thermal conductivity coating than the APS process. The difference mainly is from microstructure. From the cross-section images, it can be observed that HVOF NiCr coating has more

interfaces per unit thickness. The multilayer insulations give rise to lower thermal conductivity of the whole HVOF NiCr coating. Kulkarni et al. [2] had found the same abnormality in the case of the APS and HVOF Al_2O_3 coatings and ascribed the lower thermal conductivity of HVOF Al_2O_3 coating to the higher flattening ratio and more interfaces. The effect of oxidation is not dominant here since thermal conductivity of Cr_2O_3 (20~30W/mK) is close to that of NiCr (18W/mK), even a little higher. Therefore, the interfaces determine the coating thermal conductivity.

(a)   (b)
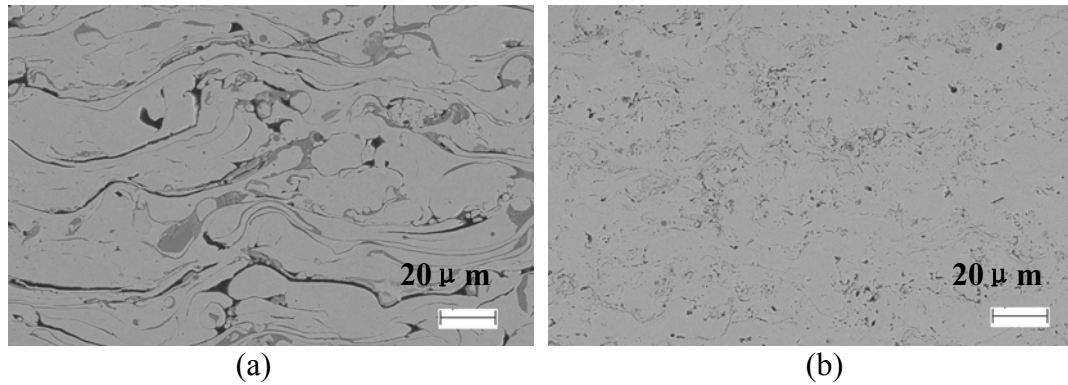
Figure 6.11 Cross-sections of Ni20Cr coatings made by different spraying techniques

(a) APS (b) HVOF
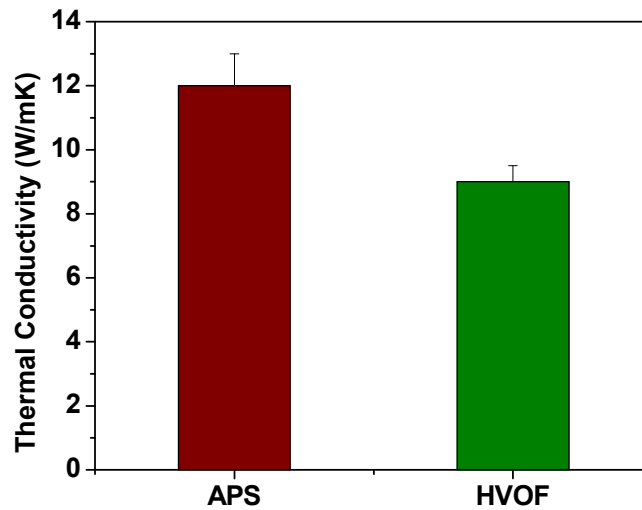
Figure 6.12 Thermal conductivity of Ni20Cr coatings made by APS and HVOF

For CoNiCrAlY coatings, the HVOF process produces higher thermal conductivity coatings than the APS process. From Fig. 6.13, it can be observed that the APS Ni5Al and CoNiCrAlY coatings have longer and larger interfaces than HVOF Ni5Al and CoNiCrAlY coatings. The longer and larger interfaces combined with the more oxidation in APS process give rise to lower thermal conductivity of APS CoNiCrAlY coatings (Fig. 6.14).
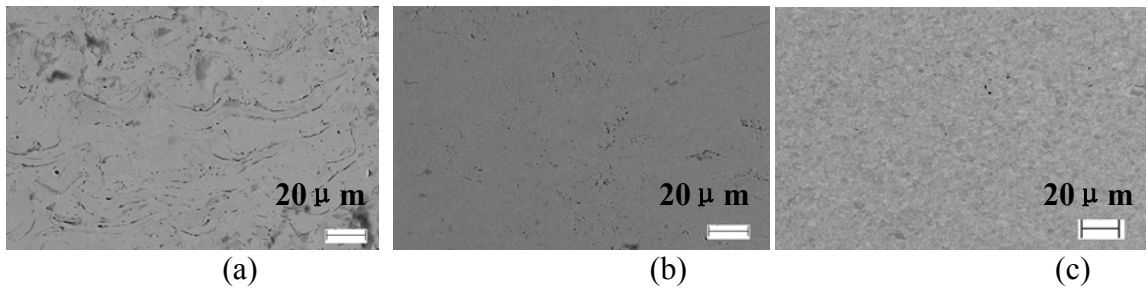

(a)   (b)
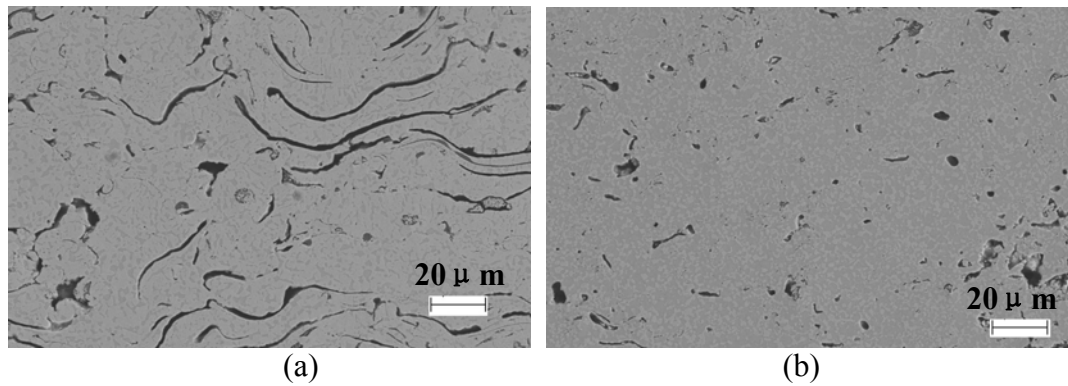
Figure 6.13 Cross-section of CoNiCrAlY coatings made by different spraying techniques

(a) APS (b) HVOF
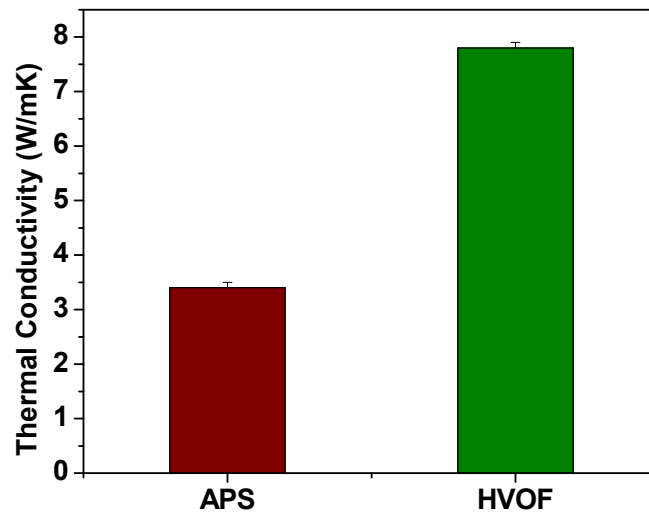
Figure 6.14 Thermal conductivity of CoNiCrAlY coatings made by APS and HVOF

The investigation of IN 718 and T-800 coatings was carried out in collaboration with Engelhard Corporation, East Windsor, CT. IN 718 and T-800 coatings were made by Praxair / Tafa JP 5000. The nominal composition of Inconel 718 is Ni, 52.4%, Cr

18.6%, Fe 18.9%, Mo 3.19% Ti 0.91%, and Nb (niobium) 5.1%. The nominal composition of T-800 is Cr-17%, Mo-28%, Si-3%, and balance Co.

Figure 6.15 shows the thermal conductivity of inconel 718 and T-800 coatings. The inconel coating has higher thermal conductivity than both low oxide and high oxide T-800 coatings. This can be explained from the coating microstructure. The SEM images of the inconel coating and T-800 coatings are shown in Fig. 6.16. The In 718 coating displays a dense microstructure which gives rise to higher thermal conductivity, whereas lamellar structures with long and fine layers and interfaces are observed in both the low oxide T-800 and high oxide T-800 coatings. The lower thermal conductivities of the T-800 coatings are attributed to the interfaces. The low oxide T-800 coating has sparser and thinner interlamellar pores than the high oxide T-800 coating. That is, the number of interfaces per unit thickness is higher in the high oxide T-800 coating. Both the more effective effect of microstructural defects and the more percentage of low thermal conductivity phase in high oxide T-800 results in lower thermal conductivity. Therefore, the thermal conductivity of the high oxide T-800 coating is the lowest among the In 718 coating and the two T-800 coatings.

The thermal conductivities of Inconel 718, T-800 are in the range from 2.5-6W/mK, the same range as Al_2O_3 coatings. It can be predicted that these coatings are potential substitute of Al_2O_3 and maybe even suitable to some cases better than Al_2O_3. For the T-800 coating, the high oxide decreases the thermal conductivity by 33% and makes its thermal conductivity even close to the value of bulk YSZ. All the information gives a clue to the development of materials for coating fabrication.
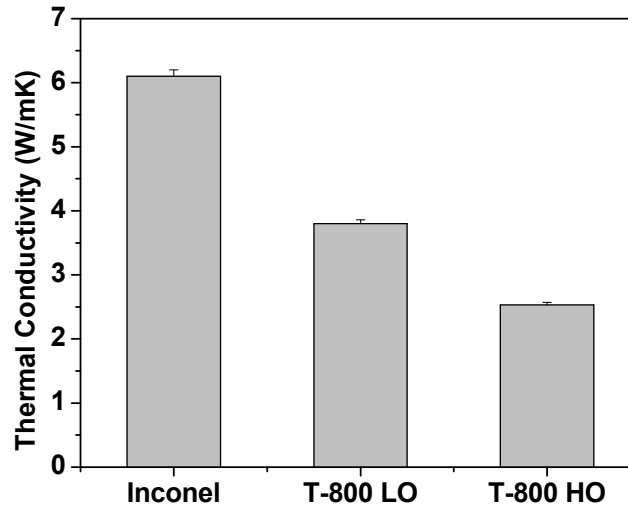
Figure 6.15 Thermal conductivity of inconel 718 and tribaloy coatings

<div align="center">(a)   (b)   (c)</div>
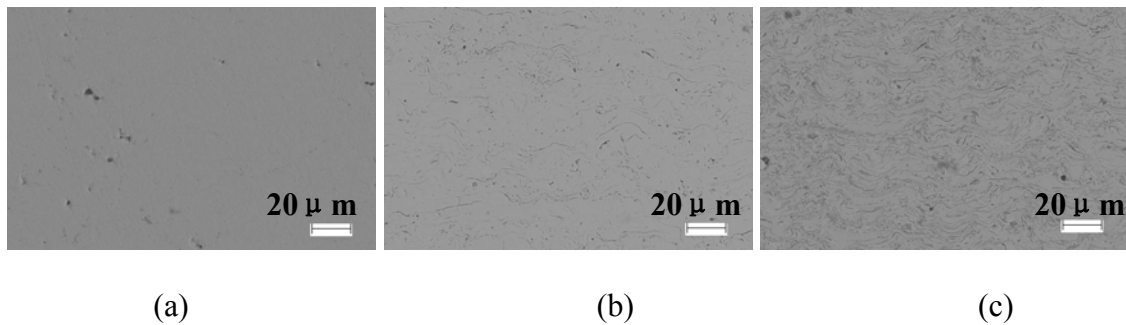
Figure 6.16 Images of cross-sections of inconel 718 and tribaloy coatings

(a)In 718 JP 5000 (b) T-800 Low Oxide JP 5000 (c) T-800 High Oxide JP 5000

6.2.2.3 Synthesis of density-thermal conductivity map

Both the introduction of oxide and microstructure defects from various spraying processes leads to the change of coating density. In the following discussion, we seek to synthesize commonalities in the observed results from all the above-mentioned Ni and Co based coatings and establish a mapping strategy to understand the dominant mechanism for the change of coating thermal conductivity and enable future coating design. The coating/bulk thermal conductivity is plotted against the coating/bulk density in Fig. 6.17. The alloy coatings fall into four zones where the thermal transport property is controlled by different mechanisms.

The CS Ni, HVOF Ni and HVOF CoNiCrAlY coatings are included in Zone I. In this zone, the coating has high density and high thermal conductivity. Due to less oxidation and lower porosity, the thermal conductivity is dominated by the intrinsic attributes of materials.

All the other HVOF coatings fall into Zone II where the interfaces control the thermal transport property. The HVOF process achieves dense coatings but low thermal conductivity for Ni5Al and Ni20Cr. So does the liquid fuel HVOF process (JP 5000) for In 718 and T-800 coatings. This is attributed to the numerous interfaces arising from the HVOF process.

The APS Ni-based coatings exhibit in Zone III and Zone V. The APS process produces medium density and low thermal conductivity coatings for Ni, Ni5Al and CoNiCrAlY but low density and low thermal conductivity Ni20Cr coating. The high particle temperature and low velocity in APS process increase the oxidation of powders and generate numerous microstructural defects. As such, the porous microstructure combined with the significant oxidation leads to low thermal conductivity for APS coatings. However, the oxidation or microstructural defect or both affects thermal

conductivity to different extent for different cases. Therefore, APS Ni, Ni5Al and CoNiCrAlY coatings drop into Zone III where thermal conductivity is dominated by oxide whereas APS Ni20Cr presents in Zone IV where both oxide and microstructural defects control thermal conductivity. The thermal conductivities of coatings made by APS process generally are lower than those made by HVOF process, which makes the APS coating a better thermal resistance surface at the expense of easier penetration of oxygen due to its porous network.
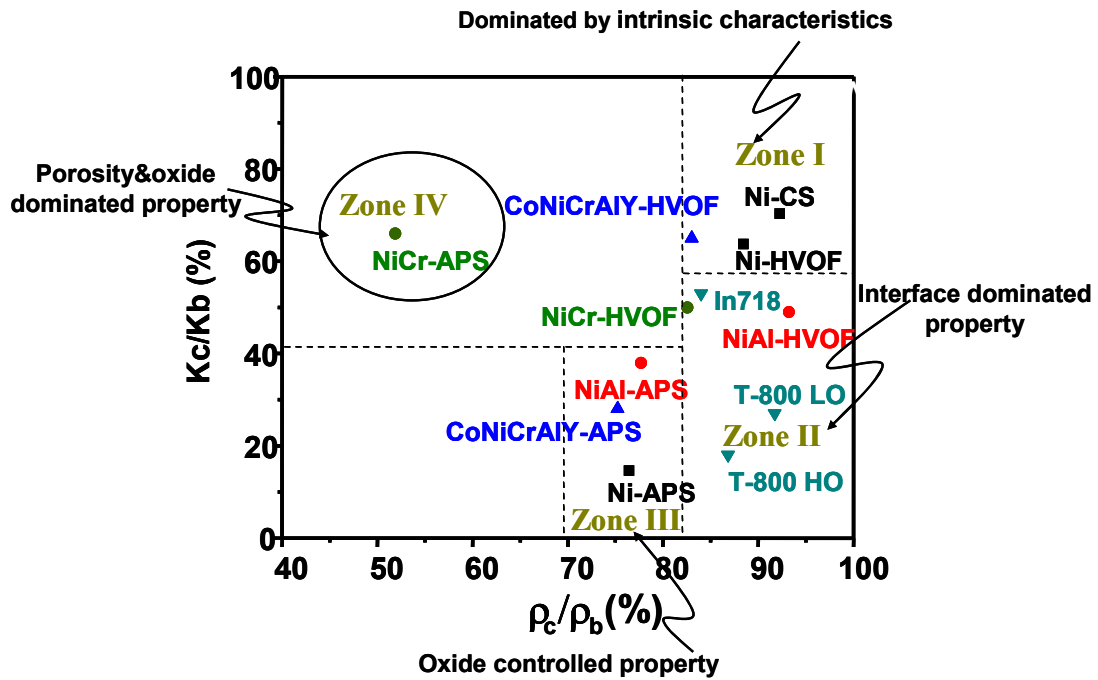
Figure 6.17 Thermal conductivity ratio-density ratio map of Ni/Co based alloy coatings

6.2.3 Cermet Coatings

Mo$_2$C has been used as a strengthening dispersion for Mo coatings to improve hardness and wear resistance [3, 4]. Although tribological characteristic was one of the major reasons for the development of Mo-Mo$_2$C coatings, thermal properties are often considered crucial to satisfy the demands of multifunctional materials. For instance Mo based coatings are used in paper drying industry in which the coating performs a combination of functions, wear and corrosion resistance as well as a thermally conducting surface for extracting the heat during the process of paper drying. However, limited investigation focuses on their thermal transport property.

Mo-35%Mo$_2$C (1.75wt% C) and Mo-60% Mo$_2$C (3.5wt% C) composite powders were selected to make coatings using essentially the same processing parameters (table 6.4). The same processing parameters were chosen given a minor change in chemistry of the material. The optical images of Mo-Mo$_2$C coatings are shown in Fig. 6.18 compared with Mo coating. Figure 6.19 displays the corresponding XRD analysis for phase and thermal conductivity of the Mo and Mo-Mo$_2$C coatings. The Mo coating in Fig. 6.18(a)

has long interfaces and high flattening ratio of splats. This is because Mo has low hardness and plasma sprayed Mo coating is relatively soft. Fewer gray areas are observed in the image of Mo-35%Mo_2C coating (Fig. 6.18(b)) than that of Mo-60%Mo_2C coating (Fig. 6.18 (c)). These gray areas represent the Mo_2C phase. This is confirmed by XRD in figure 6.19 (a). Mo-60%Mo_2C coating clearly shows Mo_2C peaks which are not visible in the diffraction pattern of Mo-35%Mo_2C coating. Both Mo-35%Mo_2C and Mo-60%Mo_2C powders show a similar percentage of carbon loss. The staring carbide content in the powder does not influence the extent of decarburization. The larger the starting carbide content in the powder, the greater the amount of carbide retained in the coating. The retention of carbon in the coating is dependent on the starting carbon content in the powder. In figure 6.19 (b), the thermal conductivity of Mo-35%Mo_2C coating doubles that of Mo coating although the porosities are similar for the two coatings. The reason is that Mo_2C acts as a sacrificial getter for the oxygen and considerable decarburization was observed during spraying [5].

Sampath et al. [3] reported that pure Mo undergoes considerable oxidation during APS and displays greater than 1wt% O_2 in the coating. The oxidation leads to lower thermal conductivity phase (MoO_2) and worse interlamellar bond between the layers. The introduction of carbon reduces the extent of Mo oxidation in the Mo-35%Mo_2C coating and yields larger metallic phase content in the composite. Furthermore, the decarburization consumes the carbon and results in little Mo_2C observed on the peripheral regions of the splat. The absence of oxides and carbides on the surface enables a more chemically clean surface and significantly improves the interlamellar bond between the layers. Thus, adding 35% Mo_2C into Mo increases the thermal conductivity extremely. However, in the case of 60wt% carbide system the thermal conductivity is halved by despite similar total porosity. This is due to higher carbide retention in Mo-60%Mo_2C coating. The retention of carbon in the coating is proportional to the starting carbide content in the powder. The Mo-60wt%Mo_2C coating remains much more carbon than the Mo-35wt%Mo_2C coating. XRD studies and lattice parameter measurements suggest that all the carbon in the powder is accounted for as Mo_2C and do not indicate any free carbon or carbon dissolved in Mo in the powder [3]. But in the coating, the excess carbon is supersaturated in the Mo lattice and distorts the lattice structure. A linear relation was found between the change in the lattice parameter and the extent of carbon in the solid solution [3]. Therefore, the retained carbon in Mo-60%Mo_2C coating acts as impurity in the Mo, results in increased scattering and thus reduces thermal conductivity.

Table 6.4   Process parameters for Mo-Mo$_2$C coatings with different fraction of Mo$_2$C

Material	Secondary Gas H$_2$ (SLM)	Primary Gas N$_2$ (SLM)	Carrier Gas N$_2$ (SLM)	Current (A)	Voltage (V)	Standoff (mm)	Feed rate (g/min)
Mo+35%Mo$_2$C	5.6	47.6	3.7	550	72	130	30
Mo+60%Mo$_2$C	5.6	47.6	3.7	550	73	130	29

(a)   (b)   (c)
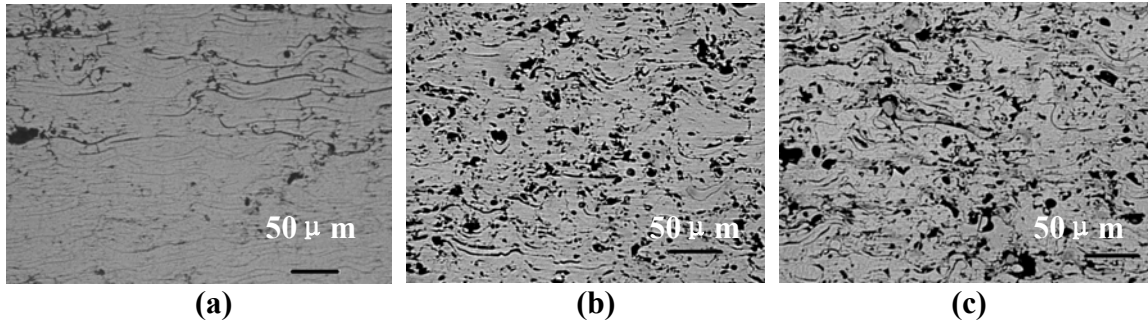
Figure 6.18 Optical images of Mo and Mo-Mo$_2$C coatings

(a)Mo (b) Mo-35%Mo$_2$C (c) Mo-60%Mo$_2$C
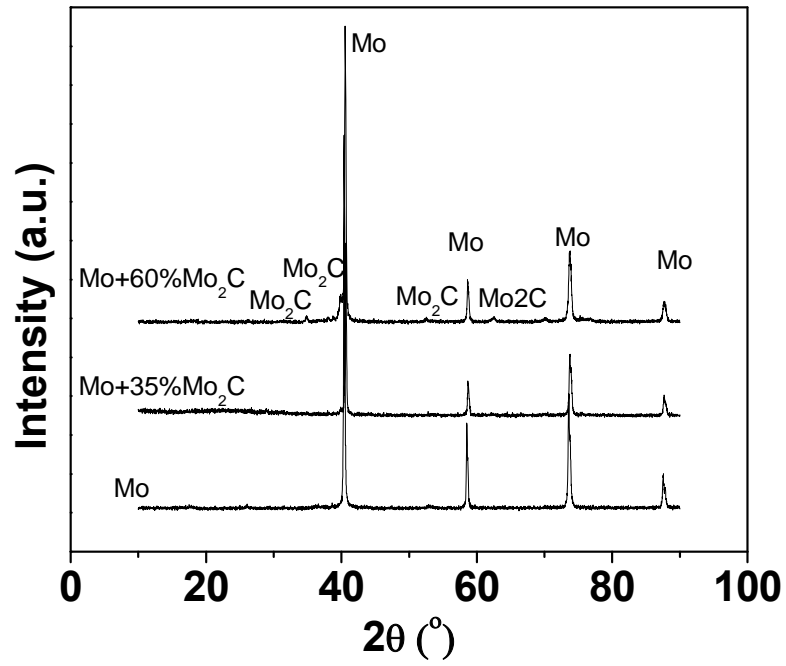
(a)
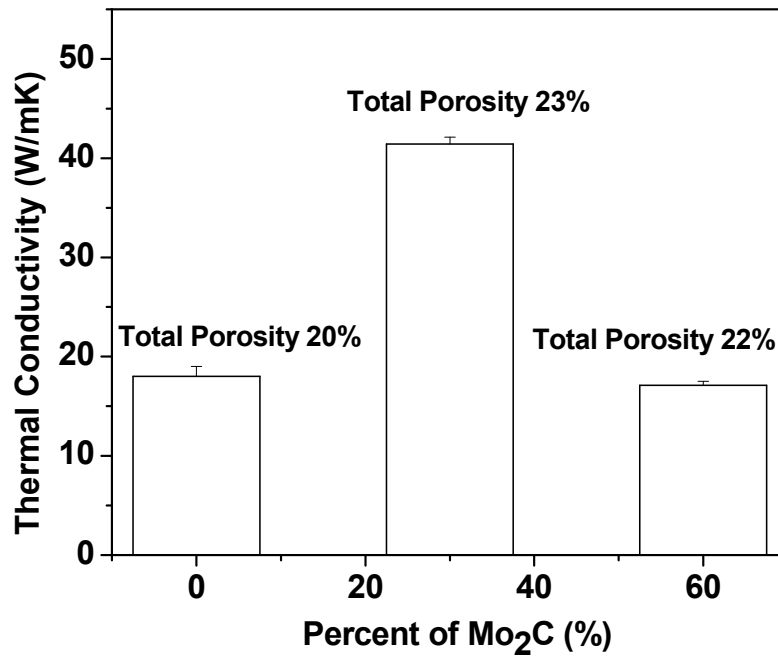
(b)

Figure 6.19. Effect of content of Mo_2C on the phase and thermal conductivity

(a) XRD (b) thermal conductivity

6.2.4 Ceramic Coatings

6.2.4.1 Al$_2$O$_3$

Thermally sprayed Al$_2$O$_3$ coatings are good protective coatings for abrasion and corrosion resistance. It is widely appreciated that the thermal spray techniques have the capability of tailoring the particle velocity and temperature [6], which yield different microstructure of coatings and final properties. The reason is that the coating is built up from splats and the splat formation is dependent on its melting state and kinetic state. The different particle states lead to a wide range of morphologies of splats– from highly fragmented to contiguous [7, 8]. In chapter 4, a single YSZ powder feedstock was chosen and process parameters were varied to achieve 3 distinct sets of coatings resulting from different average particle temperatures and velocities in order to develop process-microstructure-property relationships through the establishment of process maps. The method of process map is applied to Al$_2$O$_3$ coating here. To explore the effects of particle state on Al$_2$O$_3$ coating thermal transport property, different process parameters were combined to generate a range temperature and velocity of particles and therefore the various thermal conductivities as shown in Fig. 6.20. The temperatures and velocities were measured at the maximum flux location of the spray stream using the "Tecnar DPV 2000" (St-Bruno, QC, Canada) [9]. The variation velocity contributes more to the change of thermal conductivity than the alteration of temperature. The melting point of Al$_2$O$_3$ is 2054°C and all the particle temperatures in Fig 6.20 are higher than the melting temperature. The melting states of all the four states do not have a significant different. The higher velocity provides the larger impaction force, causes wider spread of the droplet, reduces more microstructural defects and achieves better contact between splats. The images of cross-sections are shown in Fig 6.20. The porosity decreases with the increase of particle velocity. The reduced porosity achieved denser microstructure and therefore higher thermal conductivity.
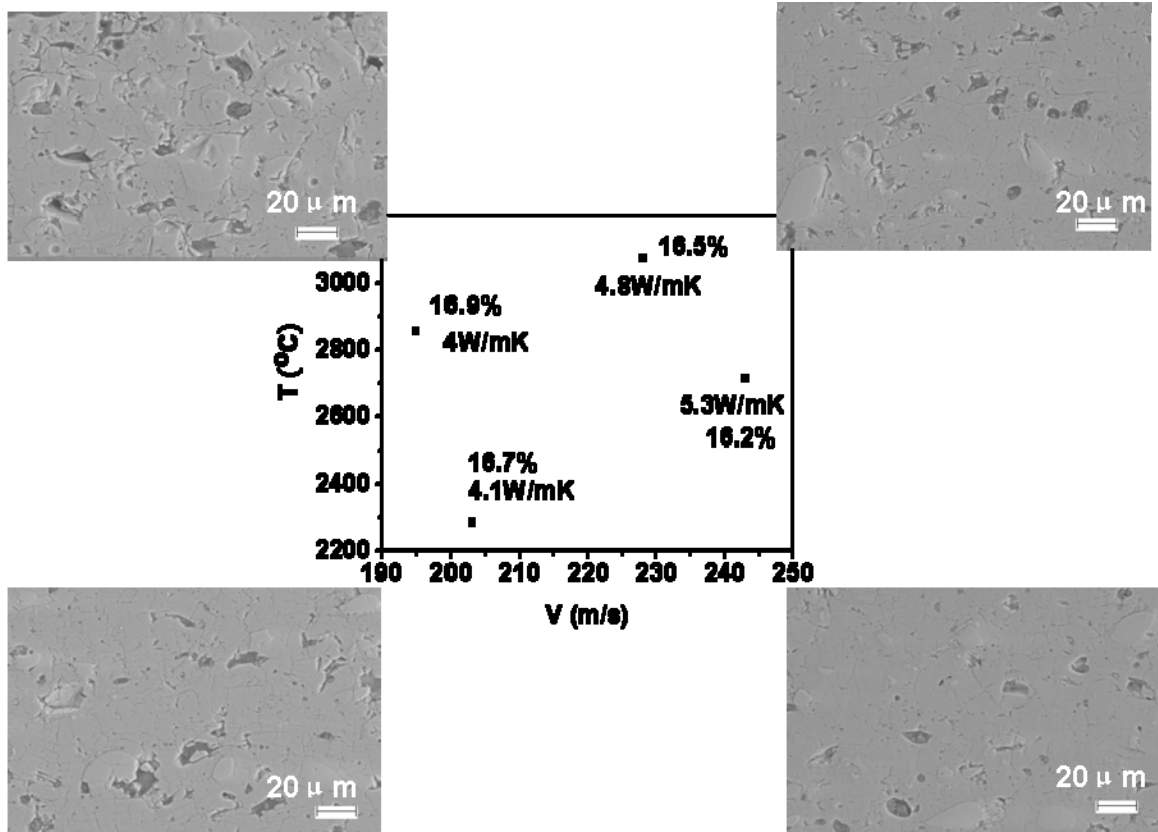
Figure 6.20 Process map of Al$_2$O$_3$ coatings

The effects of thermal spray technique and thermal cycling on thermal conductivity have also been examined. The thermal spray techniques that were adopted to make Al$_2$O$_3$ coatings include APS, HVOF and Flame Spray. The SEM images of Al$_2$O$_3$ coatings made by these three processes are shown in Fig. 6.21. The porosity from highest to lowest is Flame Spray (30%)>HVOF (24%)> APS (16%).

All the Al$_2$O$_3$ coatings made by these three techniques were subject to 20 cycles at 1100°C for 30 minutes, followed by cooling in air for 15min. The thermal conductivity results are listed in Table 6.5 for both as-sprayed and thermal cycled coatings. The relationship between thermal conductivity and porosity has been established for the Al$_2$O$_3$ coatings and the quantitative analysis about the increase of the thermal conductivity after thermal cycling was carried out and shown in Fig. 6.22. The APS process produces the lowest porosity for as-sprayed Al$_2$O$_3$ coating and therefore the highest thermal conductivity. This is due to the high particle temperature in APS process and the complete melting of Al$_2$O$_3$ powder. The porosity of the flame spray coating is the highest, which results in the lowest thermal conductivity. The HVOF coating has the medium porosity and thereby the thermal conductivity between those of APS and flame spray coatings. Kulkarni et al. [2] has found that the HVOF Al$_2$O$_3$ coating has lower porosity but lower thermal conductivity compared with the APS one. The difference of the microstructure in HVOF coatings results from the HVOF process, as we know that the

96

microstructure and property can be tailored by designing different particle states from process map.

Thermal cycling leads to sintering of Al_2O_3 coatings and necks form along the contact regions between adjacent splats. The pores become smaller and more spherical in shape. The driving force for sintering is the reduction in total surface area. The sintering progresses below the melting point and therefore no liquid phase can be observed. In Fig. 6.22, the thermal conductivities of Al_2O_3 coatings sprayed by different techniques show the elevation to different extents after sintering. The thermal conductivity of the flame spray Al_2O_3 coating only increases by 43%, the lowest among the three Al_2O_3 coatings, owing to its very high porosity and therefore a loose structure. The larger amount and dimension of pores in the flame spray Al_2O_3 coating require more surface energy for sintering and bring forth slow rising of thermal conductivity after thermal cycling. However, both APS and HVOF Al_2O_3 coatings attain more than 200% increase of thermal conductivity in virtue of thermal cycling. The increased extent of thermal conductivity of APS Al_2O_3 coating is smaller than that of HVOF Al_2O_3 coating despite of the denser structure of APS Al_2O_3 coating. This is because the thermal conductivity increases slowly if it approaches the upper limit (the thermal conductivity of bulk Al_2O_3 is 25W/mK) and the saturation leads to the smallest potential of thermal conductivity increase for APS Al_2O_3 coating. The same saturation phenomenon has been found in the case of F&C YSZ coating. In addition, it can be observed that the thermal conductivities of thermal cycled coatings follow the same sequence (APS>HVOF>Flame) as those of as-sprayed Al_2O_3 coatings, consistent with the finding of the annealed YSZ coatings in Chapter 4. The starting microstructures of as-sprayed Al_2O_3 coatings determine the thermal transport property after thermal cycling.

(a)   (b)   (c)
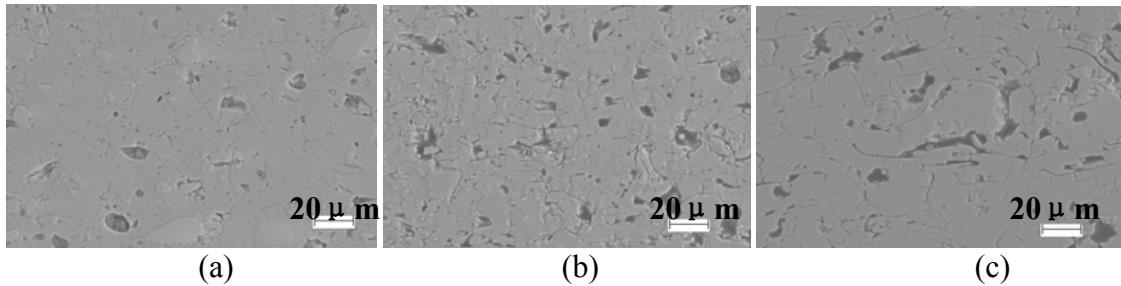
Figure 6.21 Images of cross-sections of Al_2O_3 coatings made by different processes

(a) APS (b) HVOF (c) Flame

Table 6.5 Thermal conductivity of Al_2O_3 coatings

Samples	Spray Technique	Thermal Conductivity As-Sprayed	Thermal conductivity 20 Thermal Cycled
Al_2O_3	APS	5.3±0.04	16.8±0.1
Al_2O_3	HVOF	3.98±0.01	14.26±0.03
Al_2O_3	Flame	3.38±0.10	4.82±0.05
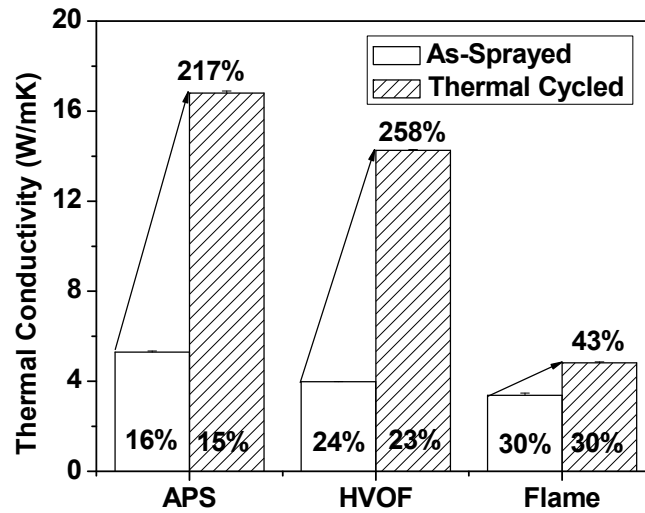
Figure 6.22 The effect of thermal cycling on room temperature thermal conductivity

The temperature dependent thermal conductivities of Al_2O_3 coatings have also been measured by Anter Flashline 5000 system at the Oak Ridge National Lab. The results on the thermal transport properties before and after thermal cycling are presented in Fig. 6.23. The high temperature thermal conductivity from the highest to the lowest is APS>HVOF>Flame. This is due to their different features of microstructural defects. The microstructural defects in the Al_2O_3 coating results in the scattering, reflection and absorption of photons at high temperatures. Therefore, the high temperature thermal conductivity is influenced by pore features, such as porosity. The lowest porosity of APS Al_2O_3 coating gives rise to the highest high temperature thermal conductivity and the highest porosity of flame spray Al_2O_3 coating leads to the lowest high temperature thermal conductivity. It is also observed that for all the as-sprayed Al_2O_3 coatings, thermal conductivity monotonically decreases from room temperature to $800^{\circ}C$ or so because scattering of lattice vibration becomes more pronounced with rising temperature. The shape of the thermal conductivity curves indicates a phonon conduction mechanism up to $800^{\circ}C$. The thermal conductivity is limited by intrinsic phonon scattering scales as $1/T$ [10]. The thermal conductivities of Al_2O_3 coatings begin to increase above $800^{\circ}C$, which is due to radiant heat transfer and sintering. At higher temperatures the photon conduction becomes increasingly important and sintering/densification of the materials begins to occur even during the measurement process [11]. For the three Al_2O_3 coatings after thermal cycling, the thermal conductivity monotonically decreases over the whole measuring range of temperature. The concrete quantitative change of thermal conductivity after thermal cycling has been examined by choosing the temperature at $1100^{\circ}C$. The increased extent of high temperature thermal conductivity from the highest to the lowest is consistent with the case of room temperature thermal conductivity. The HVOF Al_2O_3 coating has the largest increase of high temperature ($1100^{\circ}C$) thermal conductivity (68%) and the increase of high temperature ($1100^{\circ}C$) thermal conductivity

(0%) for the flame Al_2O_3 coating is the smallest. All the increased extents of high temperature (1100°C) thermal conductivity are lower than the corresponding increase of room temperature thermal conductivity. The reason is that the densification resulting from thermal cycling eliminates the sintering during the measurements of the thermal cycled Al_2O_3 coatings. Furthermore, the increased radiation with temperature is counteracted by the absorption, reflection and refraction of photons in the coatings. The radiation experiences the absorption, reflection, refraction and transmission when it proceeds from the coatings. Within solid materials, interactions generate between the electromagnetic radiation and atoms, ions, and/or electrons, such as electronic polarization and electron energy transitions. The polarization would result in the absorption of the radiation energy and the reduction of velocity (refraction). During the propagation of radiation from air to Al_2O_3, reflection also happens at the interface owing to the different index of refraction between air and Al_2O_3. The index of refraction affects the optical path of radiation and the fraction of radiation that is reflected at the surface. The more microstructural defects bring on more opportunities for the propagation of the radiation between the two phases (air and Al_2O_3) and greater reflectivity. In addition, the absorption and emission of radiation give rise to the electron transitions from one energy state to another. The photon energy is absorbed in each excited event. But the stimulated electron cannot stay in the excited state indefinitely and decays back into the ground state after a short time. There is a conservation of energy for absorption and emission electron transitions. Hence, the high temperature thermal conductivity appears very complex for as-sprayed and thermal cycled coatings.

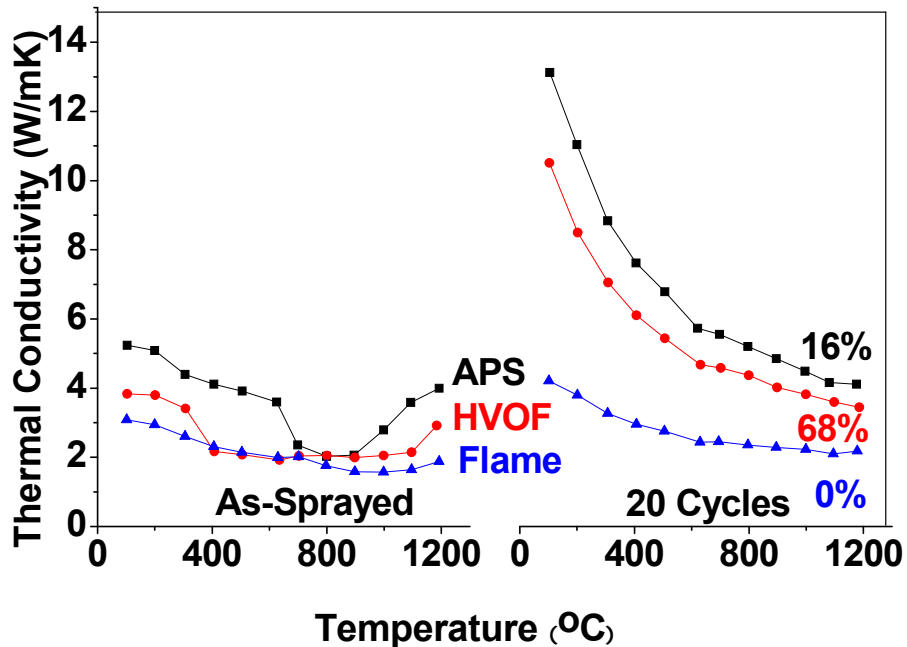
Figure 6.23 The effect of thermal cycling on temperature dependent thermal conductivity

6.2.4.2 HOSP YSZ Coatings- Process Map

The distinctive hollow morphology of HOSP YSZ powder brings on high interlamellar porosity and low thermal conductivity. The HOSP YSZ powder is an ideal material as thermal barrier coating. In chapter 4, the microstructure and thermal conductivity of F&C YSZ coatings were tailored by adjusting the particle state using process map. In this section, the process map method is applied to HOSP YSZ in order to examine the performance of coatings. The microstructure was examined somewhere else. Figure 6.24 shows the porosity calculated by precision density method and thermal conductivity values of coatings obtained at different particle states. Both the particle temperature and velocity of the coating R588 are the lowest, which leads to the highest porosity and the lowest thermal conductivity. The coating R591 has the same particle temperature as the coating R588 but higher velocity. The various velocities play an important role in the difference of microstructure and property between R588 and R591. On the one hand, the higher velocity for R591 results in a significant impact of droplets and produces more fragmental splats. On the other hand, the higher velocity shortens the dwell time of particles and thus some incompletely melted particles are observed. Therefore, more microstructural defects are brought into the coating R591 and results in a little higher porosity compared to coating R588. However, the thermal conductivity of the coating R591 is a little higher than that of R588 although R 591 has higher porosity. This is because R588 has large and long interlamellar pores whereas a great number of globular pores are present in R591 with small and short interlamellar pores, as observed from the microstructures of the coatings R588 and R591.Based on R591, the particle temperature and velocity are both increased significantly for spraying coating R592. The increase of the particle temperature improves the melting state of particles to a great extent, and produces dense and well adhered deposit. The porosity drops dramatically and therefore the thermal conductivity has a great increase. With further enhancing the particle temperature and velocity for making the coating R587, the melting state is only improved a little since the benefit from increased temperature is counteracted by the increased velocity which shortens the dwell time. Hence, there is only a small decrease of porosity for R587 and its thermal conductivity increases trivially. The lowest porosity and the highest thermal conductivity are achieved by the coating R 593. The particle temperature of R593 is only a little lower than that of R587. But R593 has much slower particle velocity than R587, which is favorable to the improvement of melting state due to long dwell time in the flame.
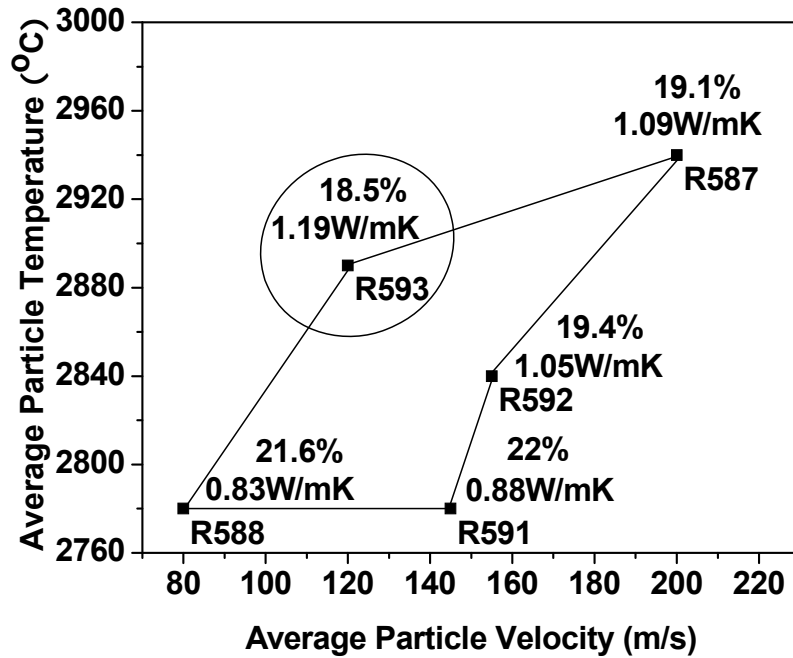
Figure 6.24 Process for YSZ coatings made of HOSP powders

All the coatings in Figure 6.24 experience 20 thermal cycles (30 minutes heating and 15 minutes cooling for each cycle) and 10h isothermal exposure at 1100°C. The two annealing processes are carried out at the same temperature and have the same total heating time. The results of thermal conductivities before and after annealing as well the percentage increases of thermal conductivities resulting from annealing are shown in Fig. 6.25. For all the coatings, the percentage increases of thermal conductivities after 10h isothermal exposure are a little higher than those after thermal cycling (20cycle). The differences are not significant. The same heating time at the same temperature leads to similar sintering and change of thermal conductivity. This is at least true for a short annealing time like 10h.
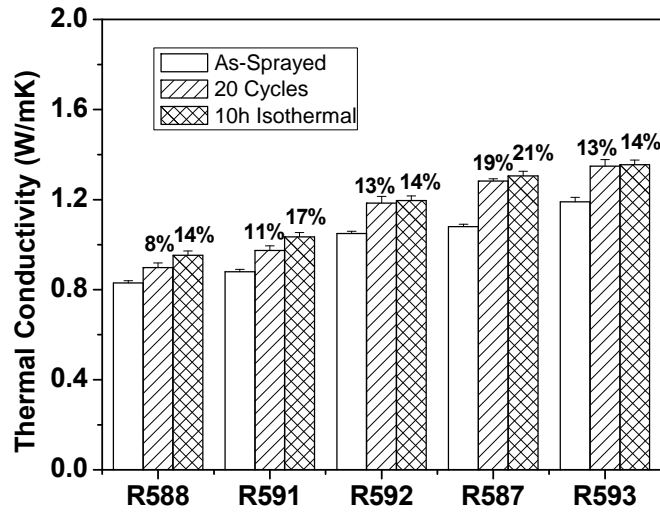
Figure 6.25 The effect of thermal cycling and isothermal exposure on room temperature
thermal conductivity

Figure 6.26 shows the temperature dependent thermal conductivities of the HOSP
YSZ coatings before and after annealing. The thermal cycling and isothermal exposure at
the same temperature after the same heating time give rise to the similar increase of high
temperature thermal conductivity for all the coatings. This is consistent with the case of
room temperature thermal conductivity change. In Figure 6.26, there is a sharp increase
of thermal conductivity from R591 to R 592, even after both thermal cycling and
isothermal exposure. The slight change of particle state from R591 to R 592 leads to a
significant change of microstructure and property. This gives a valuable clue to design
coatings. In Fig. 6.26, it can be observed that the five coatings crowd into two zones: one
is low TV zone and the other is high TV zone, as shown in the two ellipses. The three
coatings in the high TV zone have small difference and show similar performance in the
application circumstance. So do the two coatings in the low TV zone. This allows a great
range of process parameters for coating design and provides a framework to improve the
coating reliability and performance.
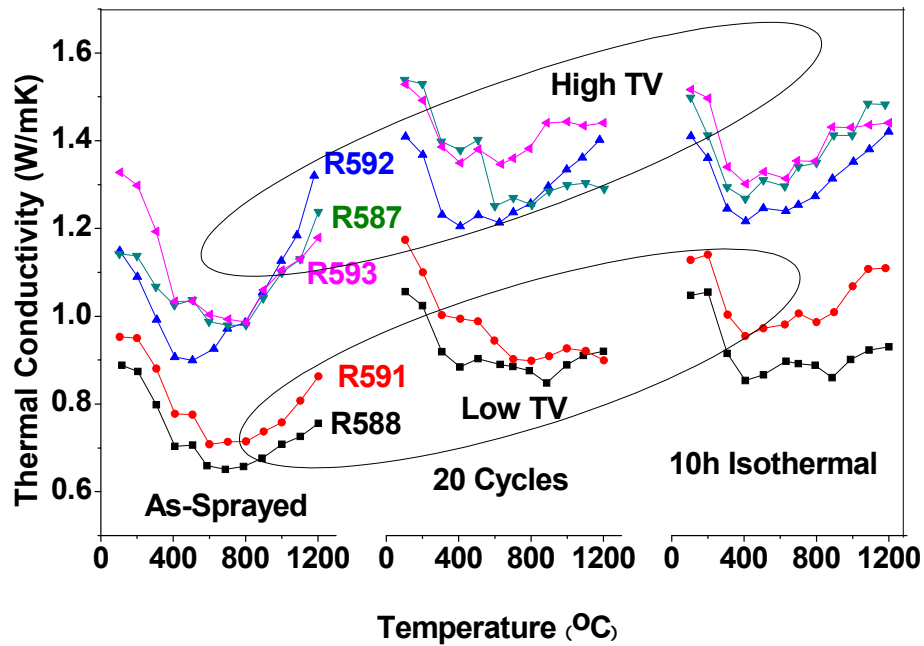
Figure 6.26 The effect of thermal cycling and isothermal exposure on thermal conductivity on high temperature thermal conductivity

6.2.5 FGMs

Low thermal conductivity ceramic coatings are applied as thermal insulation of metallic components in turbine engines, aircraft propulsion, power generation and marine propulsion [12]. The significant difference in thermo-mechanical properties of metals and ceramics leads to thermal mismatch related failure, and reduces the life time of components. Functionally graded materials (FGMs) can gradually change the composition between metal and ceramic phases over definable geometrical orientations and distance[13]. Thus, the FGMs reduce discontinuities in physical, mechanical and thermal properties and avoid mismatch-related failure in service [13]. Plasma sprayed processing offers a flexible and inherently economic means for producing FGMs [14]. The detailed review of the contribution of plasma spray on manufacturing FGM is discussed in reference [14]. In this study, the plasma spraying parameters (Table 6.6) are extensively optimized using in-flight diagnostics to assure both species molten in-flight at the intended spray distance.

Table 6.6   Processing parameters for NiCrAlY-YSZ composite coatings

Parameter	Secondary Gas H$_2$ (SLM)	Primary Gas N$_2$ (SLM)	Carrier Gas N$_2$ (SLM)	Current (A)	Standoff (mm)	Metal Feed rate (g/min)	Ceramic Feed rate (g/min)
Value	10	40	2.5	600-650	100	7.5-0	0-30

The microstructure of different content NiCrAlY-YSZ coatings was analyzed elsewhere [13] and the higher ceramic content composites generally show higher porosity. The thermal conductivity of NiCrAlY-YSZ composite as a function of YSZ percent is plotted in Fig. 6.27 and the phase change is characterized by XRD (distinct peak height variation with composition) shown in Fig. 6.28. Mixing has a marked effect on thermal conductivity of the FGMs. The thermal conductivity decreases sharply up to 40% YSZ and then transits to a more gradual change with further increase of YSZ content. The thermal conductivity results are lower than those obtained from rule of mixtures (the dotted line in Fig. 6.27). The anisotropic microstructures of different content NiCrAlY-YSZ coatings result in nonlinear behavior of thermal conductivity with respect to YSZ content. With the increase in ceramic phase, the reducing trend of thermal conductivity still remains. The stepped composition design achieves graded microstructure and property of coatings and mitigates the discontinuities in physical, mechanical and thermal properties.
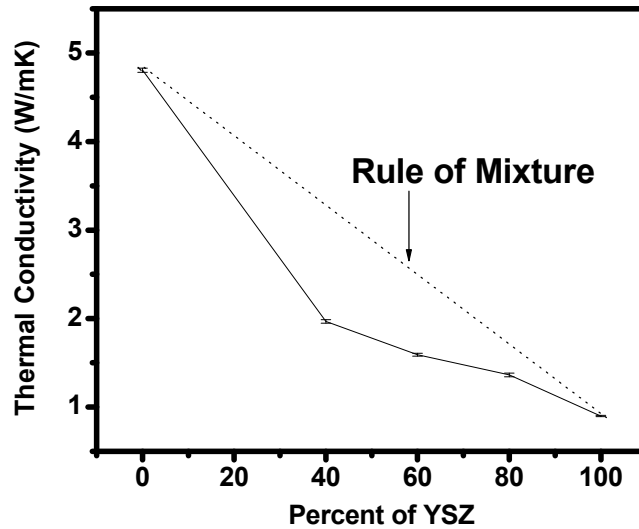
Figure 6.27 Effect of YSZ content on thermal conductivity of NiCrAlY-YSZ composites
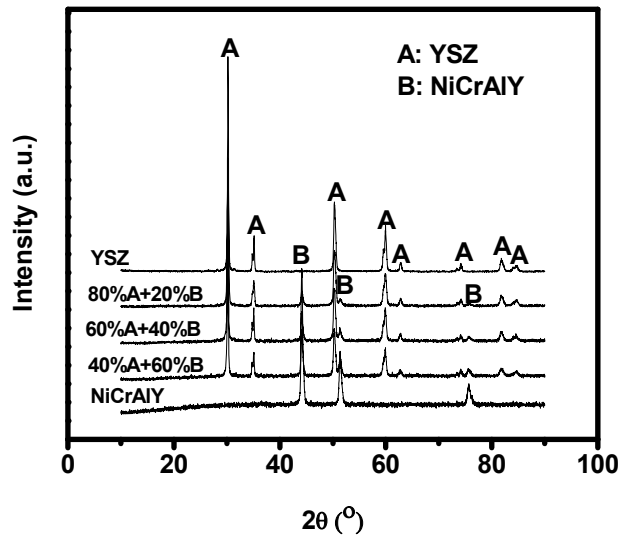
Figure 6.28 XRD of NiCrAlY-YSZ coatings including different content of YSZ

Fig. 6.29 shows the thermal conductivity of Ni-Al$_2$O$_3$ composite coatings. The trend of thermal conductivity change of Ni-Al$_2$O$_3$ coating is the same as that of NiCrAlY-YSZ coating although the thermal conductivity of pure Ni coating is around 9 W/mK, higher than pure NiCrAlY coating.
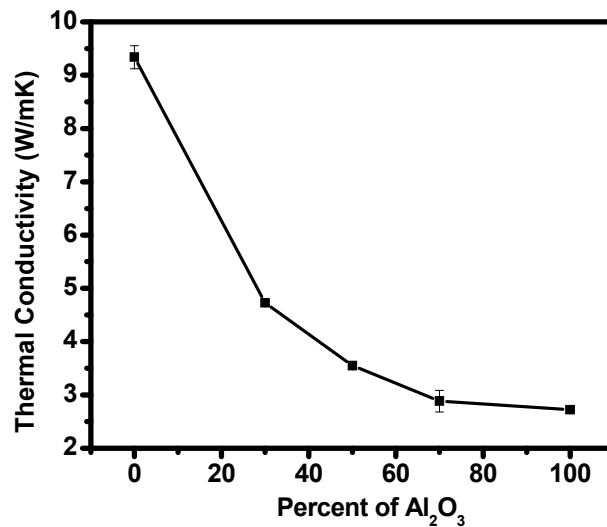
Figure 6.29 Thermal conductivity of Ni-Al$_2$O$_3$ composite coatings

6. 3 Conclusions

A systematic assessment of thermal transport property of wide range materials was carried out to achieve more functions of thermally sprayed coatings.

For single elemental metallic coatings, the intrinsic attributes of materials determine the thermal transport property. The extrinsic effects arising from process also significantly affect coating thermal conductivity, such as oxidation and microstructure defects. Owing to distinct intrinsic parameters, different spraying processes lead to different oxidation and microstructure defects and therefore different coating thermal conductivity. The high particle temperature of the APS process results in numerous oxidation and low thermal conductivity. The high velocity of the HVOF and CS processes reduces the dwell time of particles and achieves high thermal conductivity. The low particle temperature in CS process significantly mitigates the oxidation and thermal conductivity reduction. The effect of process has also been extended to Ni and Co based alloy coatings, and the same trend has been observed. In the case of Ni and Co based alloy coatings, it is also found that the coating thermal conductivity decreases with the increase of alloying elements because the different metal elements act as impurities which distort the crystal lattice, scatter the electron motion and decrease the conductivity. The combination of the intrinsic and extrinsic effects makes the alloy coatings fall into different zones where the thermal conductivity is dominated by distinct mechanisms. Generally, CS coatings present in the zone where intrinsic attributes dominate the property, HVOF coatings drop into the interface dominant zone and APS coatings fall into the zone where oxide and microstructural defects are important.

For ceramics, the process map method was successfully applied to Al_2O_3 and HOSP YSZ. For Al_2O_3, the higher velocity provides the larger impaction force, causes wider spread of the droplet, reduces more defects, achieves better contact between splats, and gives rise to high thermal conductivity. For HOSP YSZ, low velocity increases the dwell time in the flame. Therefore, the combination of low velocity and high temperature fulfills the best melting state and produces the coating with the lowest porosity and highest thermal conductivity. Another interesting finding is that the thermal cycling and isothermal exposure at the same temperature 1100^oC after the same heating time 10h lead to the similar increase of thermal conductivity for the HOSP YSZ coatings. The examination of the NiCrAlY-YSZ FGMs displays that the anisotropic microstructures result in lower thermal conductivities than obtained by rule-of-mixtures and therefore nonlinear behavior of thermal conductivity with respect to YSZ content.

References

1.   S. Sampath, X. Y. Jiang, J. Matejicek, L. Prchlik, A. Kulkarni and A. Vaidya, Role of thermal spray processing method on the microstructure, residual stress and properties of coatings: an integrated study for Ni-5 wt.%Al bond coats, *Materials Science and Engineering a-Structural Materials Properties Microstructure and Processing*, Vol. 364, No.1-2, 2004, p. 216-231.

2.   A. Kulkarni, S. Sampath, A. Goland, H. Herman and B. Dowd, Computed microtomography studies to characterize microstructure-property correlations in thermal sprayed alumina deposits, *Scripta Materialia*, Vol. 43, No.5, 2000, p. 471-476.

3.   S. Sampath and S. F. Wayne, Microstructure and Properties of Plasma-Sprayed Mo-Mo$_2$C Composites, *Journal of Thermal Spray Technology*, Vol. 3, No.3, 1994, p. 282-288.

4.   L. Prchlik, S. Sampath, J. Gutleber, G. Bancke and A. W. Ruff, Friction and wear properties of WC-Co and Mo-Mo2C based functionally graded materials, *Wear*, Vol. 249, No.12, 2001, p. 1103-1115.

5.   L. N. Smith and C. J. Lobb, Percolation in 2-Dimensional Conductor-Insulator Networks with Controllable Anisotropy, *Physical Review B*, Vol. 20, No.9, 1979, p. 3653-3658.

6.   S. Sampath and X. Jiang, Splat formation and microstructure development during plasma spraying: deposition temperature effects, *Materials Science and Engineering a-Structural Materials Properties Microstructure and Processing*, Vol. 304, 2001, p. 144-150.

7.   A. Kulkarni, A. Vaidya, A. Goland, S. Sampath and H. Herman, Processing effects on porosity-property correlations in plasma sprayed yttria-stabilized zirconia coatings, *Materials Science and Engineering a-Structural Materials Properties Microstructure and Processing*, Vol. 359, No.1-2, 2003, p. 100-111.

8.   M. Friis, P. Nylen, C. Persson and J. Wigren, Investigation of particle in-flight characteristics during atmospheric plasma spraying of yttria-stabilized ZrO2: Part 1. Experimental, *Journal of Thermal Spray Technology*, Vol. 10, No.2, 2001, p. 301-310.

9.   A. Vaidya, T. Streibl, L. Li, S. Sampath, O. Kovarik and R. Greenlaw, An integrated study of thermal spray process-structure-property correlations: A case study for plasma sprayed molybdenum coatings, *Materials Science and Engineering a-Structural Materials Properties Microstructure and Processing*, Vol. 403, No.1-2, 2005, p. 191-204.

10.   N. P. Padture and P. G. Klemens, Low thermal conductivity in garnets, *Journal of the American Ceramic Society*, Vol. 80, No.4, 1997, p. 1018-1020.

11.   L. Pawlowski and P. Fauchais, Thermal transport properties of thermally sprayed coatings, *International Materials Reviews*, Vol. 37, No.6, 1992, p. 271-290.

12.   N. P. Padture, M. Gell and E. H. Jordan, Materials science - Thermal barrier coatings for gas-turbine engine apptications, *Science*, Vol. 296, No.5566, 2002, p. 280-284.

13.   S. Sampath, W. C. Smith, T. J. Jewett and H. Kim, Synthesis and Charaterization of Grading Profiles in Plasma Sprayed NiCrAlY-zirconia FGMs, *Materials Science Forum*, Vol. 308-311, 1999, p. 383-388.

14.   S. Sampath, H. Herman, N. Shimoda and T. Saito, Thermal Spray Processing of FGMs, *Mrs Bulletin*, Vol. 20, No.1, 1995, p. 27-31.

Chapter 7.

Processing-Microstructure-Property Relations in Anisotropic Thermal Sprayed Coatings

7.1 Introduction

Thermal spray technique was introduced by Schoop in the early 1900s [1] and used to produce protective coatings. The high velocity impingement of molten droplets on the substrate during thermal spray process produces layered structure and thus anisotropic microstructure of coatings. The anisotropic microstructure is very sensitive to processing conditions and has significant influence on the properties. A fundamental understanding of the effect of anisotropy is essential for optimizing process and tailoring microstructural as well as establishing process-microstructure-property relations.

In this study, a systematic assessment for the effect of porosity, powder morphology and particle state on the anisotropy of YSZ coating, the effect of spray techniques on the anisotropy of Al_2O_3 coating and the anisotropic thermal transport property of metallic coatings has been carried out in order to understand the effect of anisotropic microstructure on the thermal transport property and establish the processing-microstructure-property relationships. Two techniques are adopted and compared for the in plane thermal conductivity measurements of a variety of thermally sprayed coatings: the scanning-laser-heating AC method using LaserPIT Thermal Diffusivity Meter (Ulvac-Riko, Inc.) and the laser flash method using the Holometrix laser flash instrument (HLF). The percolation theory is applied for interpreting the effect of anisotropic microstructural defects on thermal conductivity.

7.2 Experimental Details

In this study, two methods are used to measure in-plane room temperature thermal conductivity of thermally sprayed coatings: one is the scanning-laser-heating AC method using LaserPIT Thermal Diffusivity Meter (Ulvac-Riko, Inc.); the other is the laser flash method using the Holometrix laser flash instrument (HLF).

LaserPIT Thermal Diffusivity Meter can measure thermal diffusivity and conductivity of a free-standing for wide variety of materials from CVD diamonds to polymer and is operated in a vacuum mode. The sample for LaserPIT Thermal Diffusivity Meter is about 30mm long and 2.5~5mm wide. One surface of the sample is coated with dry-graphite-film. A pare of pieces of the silicone gel sheet about 2.5mm wide and 5~7 mm long adhere to the sample holder on the positions where the ends of the sample are located. The non-coated side of the sample is attached on the junction point of the thermal couple using a small amount of silver paste to achieve a good thermal contact. Data of amplitude and phase are recorded as function of count of time, which is proportional to the spatial distance. The amplitude and phase are shown in logarithmic and expected to give straight lines. The thermal diffusivity and conductivity can be determined from the slope of the logarithmic amplitude and phase vs. spatial distance.

Holometrix laser flash instrument can be used to measure in plane thermal diffusivity and conductivity by using a radial heat flow method. This method removes the steady-state condition at the expense of measuring temperature as a varying function of time. The sample size for HLF is 1 inch by 1 inch. Both sides of the sample are coated with graphite. The laser beam is collimated or focused on the front face of the sample, and the distance that heat must flow is significantly greater. A mask with a circular pinhole concentric with the beam axis is used to define the viewing radius of the IR detector. The heat flow has two components: one through the sample and one in the plane of sample. Heat that flows directly through the samples will be blocked by the mask [2]. It is assumed that the measured materials are isotropic in the plane. The radial, in-plane measurement does not constrain the heat flow to one or even two dimensions. The half time can be obtained by detecting the temperature rise at a radius greater than the beam radius in the center area on the rear face.

The in-plane thermal conductivities of five YSZ coatings obtained by both HLF and Laser PIT instruments are listed in Table 7.1 as well as the standard deviations. The coefficient variation (CV) is the ratio of the standard deviation to the mean. The thermal conductivity values obtained by these two methods are close for each sample. But the accuracy of HLF for in plane thermal conductivity measurements is $\pm15\%$ whereas that of PIT is $\pm3\%$. Each sample was measured 6 times to determine the accuracy. The PIT achieves much better accuracy of in-plane thermal conductivity than HLF and therefore can be considered a more reliable result.

Table 7.1 In-plane thermal conductivity measurements (Holometrix and Laser PIT)

Sample	Holometrix	SD	CV(%)	Laser PIT	SD	CV(%)
HOSP	0.99	0.07	7	1.04	0.01	1
A&S	1.1	0.15	14	1.07	0.01	1
F&C	1.02	0.12	12	0.85	0.03	3
Low TV	0.91	0.10	11	0.84	0.01	1
High TV	0.93	0.05	5	0.96	0.01	1

The unit of thermal conductivity and SD obtained by Holometrix and Laser PIT is W/mK.

The through thickness thermal conductivities of all the material systems were measured by Holometrix Laser Flash Instrument. The free standing sample was rounded

to a disk with diameter of 12.7mm and coated with graphite. The thermal diffusivity was determined by subjecting one side to a short laser pulse and recording the temperature rise on the opposite side [3]. The specific heat was calculated from the same data of temperature rise recorded in thermal diffusivity measurement with a suitable calibration by comparing to the temperature rise of a reference sample of known specific heat. With an additional measurement of bulk density, thermal conductivity was calculated. The through thickness thermal conductivity will not be affected by the in plane thermal conductivity since the whole area of the sample is irradiated.

7.3 Discussion

7.3.1 YSZ Coatings

YSZ is a widely used material for thermal barrier coatings (TBCs) on heat engine parts to impart protection to components against failure under excessive heat loads, to increase inlet temperatures with consequent improvements in efficiency, and to reduce requirements for cooling. Plasma spray technique is the traditional method used to make YSZ coatings as TBCs. The plasma sprayed process involves melting of feedstock materials in a plasma plume and rapidly transporting these molten particles to the substrate, where rapid solidification of individual particle occurs upon impingement. Successive build-up of these "splats" results in a layered arrangement in the coating, analogous to a brick-wall-like structure where the splats are entwined in complex arrays [4, 5]. This splat-based layered microstructure leads to an intrinsic anisotropy of the coating in the direction perpendicular to the spray direction. Thus, microstructural anisotropy results in anisotropy of coating property. Kulkarni et al [6] quantified microstructure (porosity, opening dimension, orientation and morphology) in plasma sprayed YSZ coatings by means of small angle neutron scattering and used image based finite element analysis to extract thermal conductivities in both through thickness and in-plane orientations. The results were assembled to explain the anisotropy of coating nature by the orientation of the cracks and interlamellar pores.

7.3.1.1 Effect of porosity on anisotropy of YSZ

Porosity is a key variable in substantially reducing the thermal conductivity from intrinsic value of 2.5W/mK to about 1W/mK in the plasma sprayed samples. In this study, a preliminary design of experiments made it possible to select 4 sets of processing parameters (Table 7.2) bringing out different microstructure, notably in the form of porosity and pore architecture. The achieved temperature and velocity are listed in Table 7.3. The high TV inclines the YSZ coatings to low porosity, which is consistent with the finding in Chapter 4. The microstructures of all the samples were quantitatively characterized via image analysis (IA) and the preparation of the samples followed a procedure described in reference[7]. To account for variability, 20 images of each sample were taken at different locations in the coating cross section by Nikon Epiphot 200 optical microscopy at 200x (1315×1013 pixels) after polishing. By setting a suitable

threshold, the gray scale (0-255 gray scales) images were converted to binary images, which give an indication of the total pores and are used to obtain average of porosity. The comparison with measurements performed using water immersion technique showed systematical mean deviation of 2% units.

Table 7.2   Processing parameters for YSZ coatings with different porosity

Material	Secondary Gas H_2 (SLM)	Primary Gas N_2 (SLM)	Carrier Gas N_2 (SLM)	Current (A)	Voltage (V)	Standoff (mm)	Feed rate (g/min)
YSZ1 (20%)	6.9	45.3	4.8	675	73	130	30
YSZ2 (25%)	6.9	51.7	6.0	548	76	130	20
YSZ3 (30%)	1.7	31.9	3.2	466	66	130	30
YSZ4 (35%)	5.6	47.6	4.6	550	71	130	30

Table 7.3 Particle states for YSZ coatings with different porosity

Material	Particle Temperature (^{o}C)	Particle Velocity (m/s)
YSZ1 (20%)	2631	119
YSZ2 (25%)	2519	114
YSZ3 (30%)	2507	79
YSZ4 (35%)	2443	93

Figure 7.1 shows the cross section images of these coatings. In this case we treat the coating as YSZ-air (pores) composite and thus the change of porosity represents the variation of the fraction of a second dispersed phase-air. The coatings made by varying processing parameters achieved 20%, 25%, 30% and 35% porosity levels. The introduction of air phase causes the decrease of through thickness thermal conductivity from bulk value of 2.5 W/mK (figure 7.2(a)) to a range 0.7-1.3W/mK. In YSZ-air composite, phonons play the dominant role in heat conduction and the air phase has very low thermal conductivity 0.024W/mK, only around 1% of that of YSZ.   The interfaces as well as the presence of air significantly increase scattering and thus reduce thermal conductivity. Recent investigations examine the effect of pore morphology on thermal conductivity and point out the important role of interlamellar pores [3, 6, 8]. Although this is a dominant effect in the YSZ system, in our present study, the samples were chosen with sufficient differences in total porosity so as to dominate the trends. As seen in Figure 7. 2 (a), a linear rule of mixtures type effect can be observed with respect to the porosity-thermal conductivity relationship. The thermal conductivities of these four conductor-insulator composites are below the dotted rule-of-mixtures line. This is due to the existence of a sharp transition at which the long-range connectivity of the composite system suddenly disappears. This sharp transition constitutes the percolation threshold, which is between 0 and 1. The percolation threshold corresponds to the onset/ disappearance of thermal conduction and results in the thermal conductivity below the rule-of- mixtures line [9]. Further examination of the thermal conductivity anisotropy was conducted. The in-plane thermal conductivity was measured by HLF. The result suggested that the increase of porosity decreased the anisotropy (the ratio of through thickness thermal conductivity K_{tt} to in plane K_{ip}), as shown in figure 7.2 (b).

This is due to the fact that the increase of porosity is associated with reduced flattening ratio of splats and more randomized pore orientation. In figure 7.2 (a), the four solid lines linking the point of bulk YSZ and the points of YSZ coatings have four intersections A, B, C and D with the horizontal line K_{tt}=0, which approximately shows the trend of percolation threshold with the anisotropy. The increase of anisotropy lowers the percolation threshold and decreases the thermal conductivity through thickness further if it is assumed that the anisotropic systems have the same critical exponent and the same asymptotic extent [9].

The four coatings were subject to 20 cycles at 1100°C for 30 minutes, followed by cooling in air for 15min. The temperature dependent though-thickness thermal conductivities for both as-sprayed and thermal cycled coatings were measured and the results are shown in Figure 7.3. The starting microstructure determined the change of temperature dependent thermal conductivity. The higher porosity leads to lower thermal conductivity for both as-sprayed and thermal cycled coatings. A graded thermal conductivity is achieved by tailoring the graded porosity. In addition, the temperature dependent thermal conductivity increases after thermal cycling, consistent with the previous study of annealed YSZ coatings in Chapter 4.

(a)   (b)

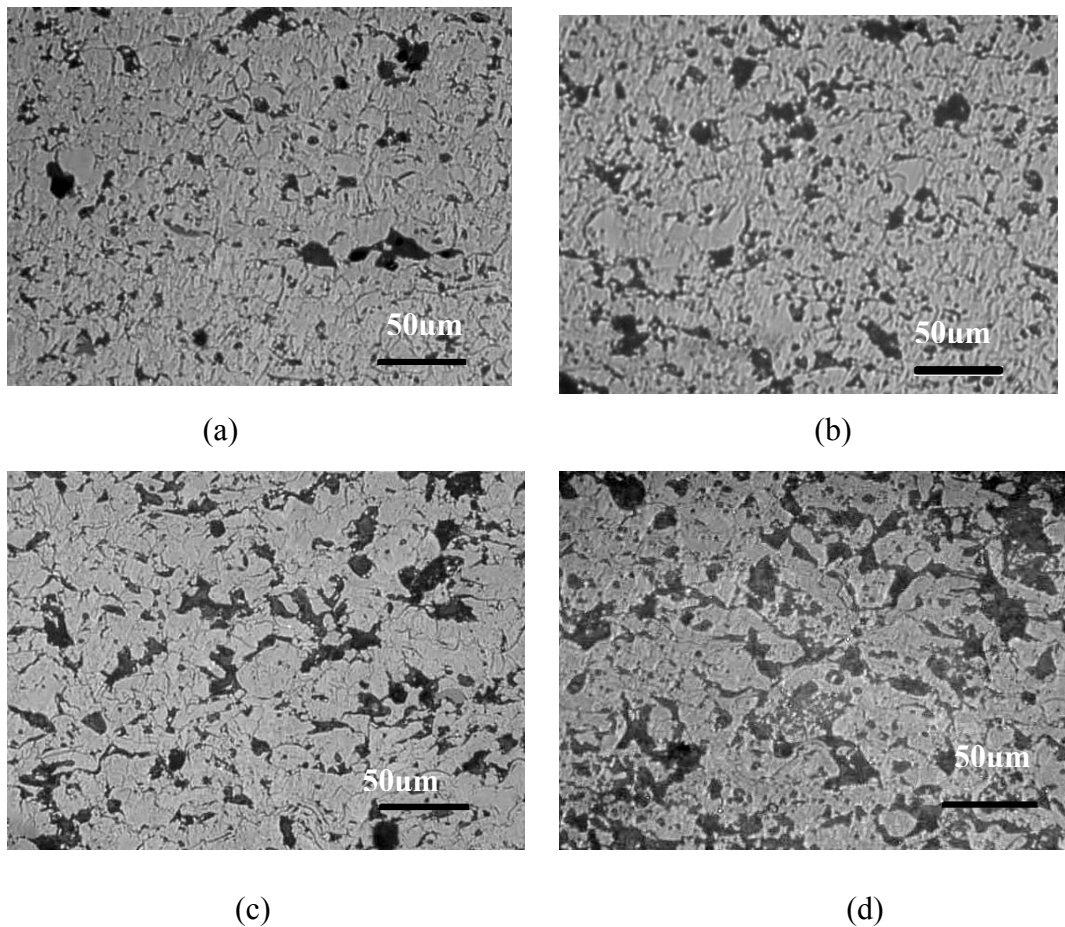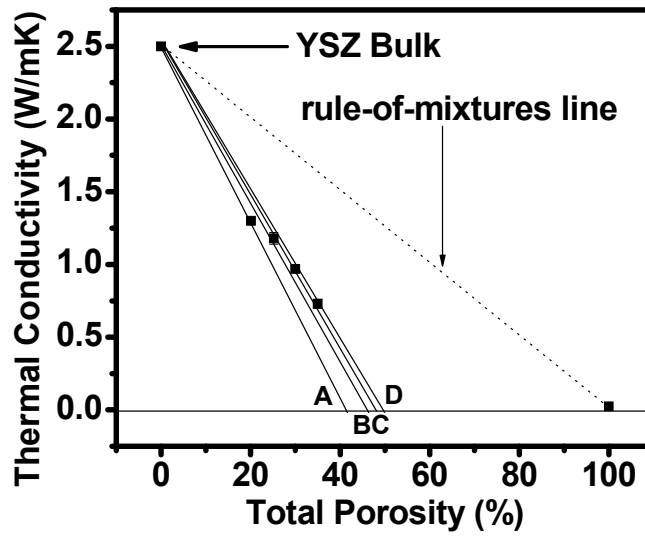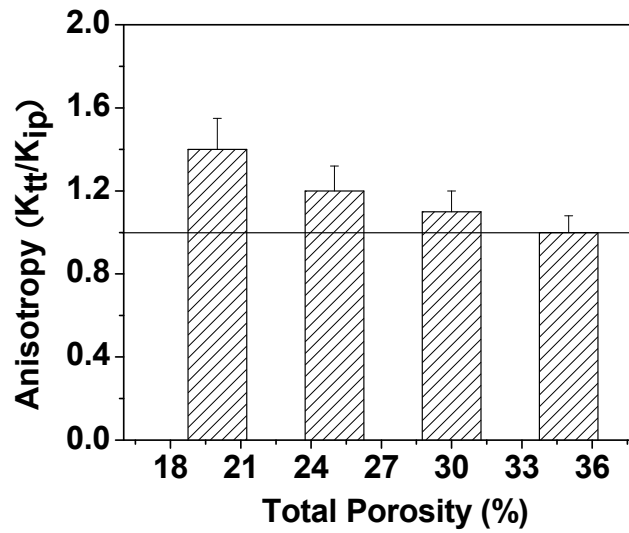(c)   (d)

Figure 7.1 Optical cross-section images of YSZ coatings with different amount of air

(a) 20% (b) 25% (c) 30% (d) 35%

(a)

(b)

Figure 7.2 Effect of the microstructure on thermal conductivity of YSZ-air composite

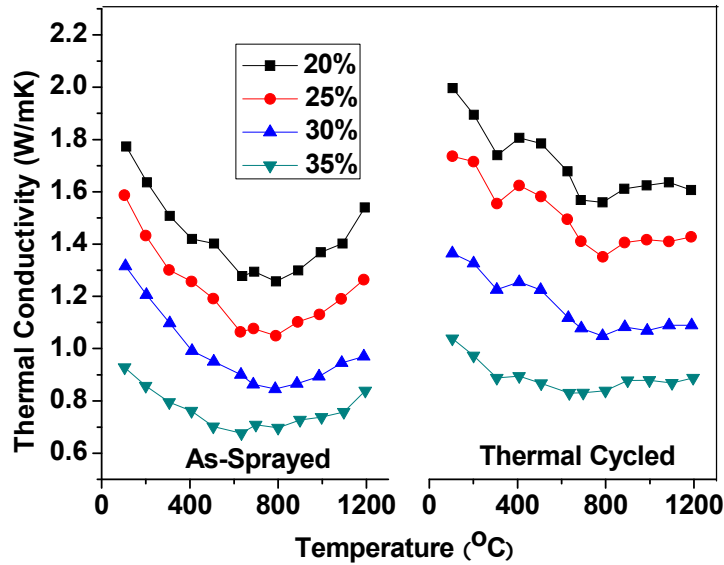(a) through thickness thermal conductivity (b) anisotropy

Figure 7.3 Effect of thermal cycling on temperature dependent thermal conductivity of YSZ coatings with different porosity

7.3.1.2 Effect of powder morphology on anisotropy of YSZ coatings

Figure 7.4 shows the anisotropy of thermal conductivity for YSZ coatings made of different morphology powders. The anisotropic values of thermal conductivity from the highest to the lowest are F&C > A&S > HOSP. From Table 7.1, it is observed that the in-plane thermal conductivities of coatings made of three morphology powders are close to each other. The thorough thickness thermal conductivity determines the anisotropy of thermal conductivity. The higher value of thermal conductivity results in higher anisotropy. The F&C powder coating has the highest through thickness thermal conductivity and therefore the highest anisotropy. The through thickness thermal conductivity of HOSP powder coating is the lowest due to its higher interlamellar porosity (Chapter 4), which leads to the lowest anisotropy of thermal conductivity around 1. The approximate isotropic thermal conductivity is favorable to the application of coatings in the circumstances with dynamic temperatures and will prolong the life time of the coating and components. Z. Wang et al. [8] have calculated the effective thermal conductivity for both through thickness and in plane directions based on SANS and SEM/OOF approaches. For the SANS approach, the thermal conductivity is greater along the through thickness direction due to the lower interlamellar porosity than cracks. This trend is consistent with the finding here in Fig. 7.4. The SEM/OFF approach estimated a higher thermal conductivity along the in plane direction. This discrepancy can be explained from the resolution of the SEM image and the size of cracks. The pore size of cracks is known to be 0.01-1 μ m and the 500x SEM image only has a relation of 0.2 μ m. Therefore, plenty of cracks were missed and the porosity of cracks was underestimated.
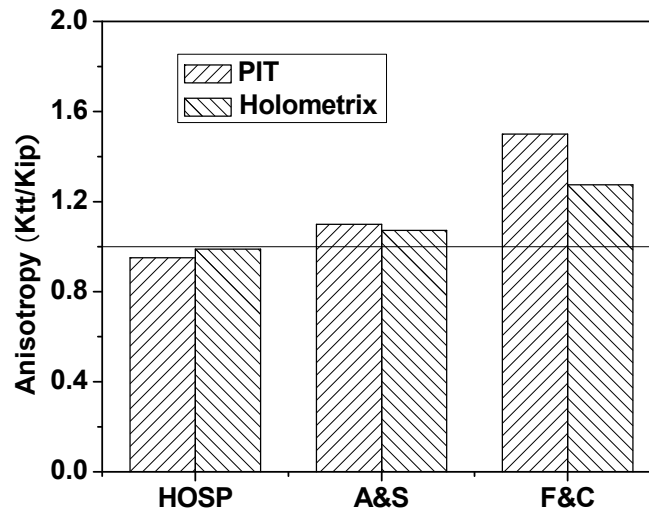
Figure 7.4 The anisotropy of thermal conductivity for YSZ coatings made of different morphology powders

7.3.1.3 Effect of particle state on anisotropy of YSZ

Process maps have been developed for air plasma spraying of YSZ in Chapter 4 and 6. It was found that tailoring the in-flight particle temperatures and velocities would be able to obtain different grades of porosity and properties. The differences in particle state also resulted in the changes in flattening ratio of splats and therefore the change of anisotropy of thermal conductivity. The anisotropies of thermal conductivity determined by Laser PIT and Holometrix instruments are shown in Fig. 7.5. Two particle states were selected from the process map in Chapter 4: low TV and high TV. The coating sprayed at higher temperature and velocity indicates higher anisotropic value for thermal conductivity. The high temperature improves the melting state of particle and the contact between splats. The higher velocity provides higher kinetic state and then a significant impact. The negative effect of the decrease of the dwell time resulting from high velocity on the melting state is counteracted by the elevation of temperature. Although high temperature and velocity result in higher flatting ratio of splats and thus more interfaces per unit thickness, they improve the contact between splats, and decrease the open dimension of interlamellar pores and interlamellar porosity. The different setting of temperature and velocity using process map achieves a wide variation of total porosity for the high TV and low TV coatings, almost 10%, due to the different melting state and kinetic state and thus the different degree incomplete contact among splats. The high porosity of low TV coating leads to low anisotropy of thermal conductivity, consistent with the finding in 7.3.1.1. The difference of total porosity caused by diverse particle states plays a dominant role in the anisotropic variation of thermal conductivity.
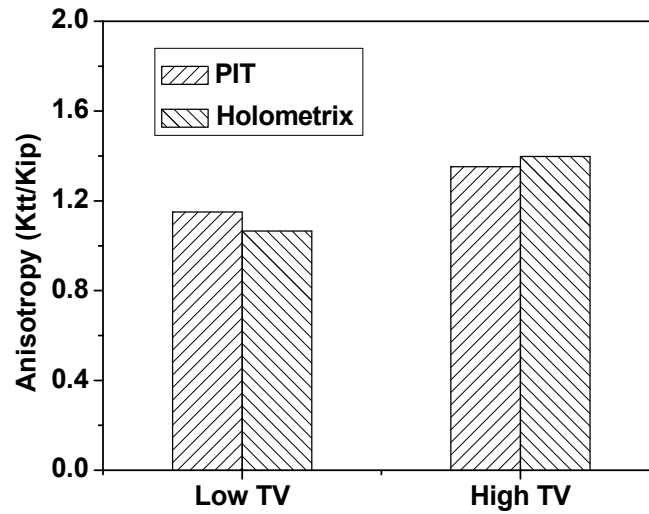
Figure 7.5 The anisotropy of thermal conductivity for YSZ coatings

made at different particle state

7.3.2 Effect of Spray Techniques on Anisotropy of Al_2O_3

The through thickness thermal conductivities of Al_2O_3 coatings sprayed by three techniques were measured by the HLF and the Laser PIT is used to measure in plane thermal conductivity, shown in Fig. 7.6 with the anisotropic values of thermal conductivity. [Since it is difficult to apply other thermal spray processes to deposit refractory YSZ material, this study was conducted for alumina].   The anisotropy of HVOF Al_2O_3 coating is lower than that of APS coating. It is known that the HVOF process has an order of magnitude greater velocity than APS. Kulkarni et al. [10] observed that APS Al_2O_3 coating showed large globular pores, interlamellar pores and cracks whereas the HVOF Al_2O_3 coating showed well adhered finer porosity due to the enhanced flattening of HVOF impacted droplets. The HVOF yields a higher number of flat interfaces per unit length normal to the substrate and effectively reduces though thickness thermal conductivity. But the thermal conductivity of HVOF Al_2O_3 coating is even lower than that of APS Al_2O_3 coating. In this study, the HVOF Al_2O_3 coating still has higher porosity than APS Al_2O_3 coating because the spraying parameters for both HVOF and APS Al_2O_3 coating are different from they were in Kulkarni's study [10]. Hence, both high total porosity and interlamellar porosity contribute to the reduction of the through thickness thermal conductivity. The value of anisotropy for thermal conductivity of HVOF Al_2O_3 coating drops significantly, even lower than that of flame sprayed Al_2O_3 coating having the highest total porosity, inverse to the finding in 7.3.1.1 and 7.3.1.3. The APS and flame sprayed Al_2O_3 coatings still obey the finding mentioned above. The difference of anisotropy resulting from the porosity variation between APS and flame sprayed Al_2O_3 coatings is not significant, not like the case of YSZ. The reason

is the both through thickness and in-plane thermal conductivities of Al_2O_3 coatings decrease with the increase of porosity but the in plane thermal conductivity of YSZ coatings keeps almost constant despite of the great decrease of through thickness thermal conductivity.
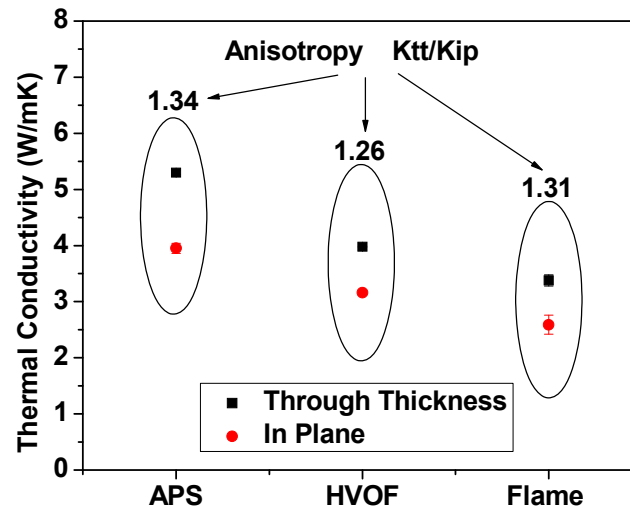
Figure 7.6 The anisotropy of thermal conductivity for Al_2O_3 coatings

sprayed by different techniques

7.3.3 Anisotropy of Metallic Coating (Mo, CoNiCrAlY)

Plasma sprayed Mo coatings are widely used as automotive piston rings, aeroturbine engines, and paper and plastics processing machinery due to the excellent wear resistance of Mo, particular at high temperatures ($>800^oC$)[11]. The nickel- or cobalt-based structural super-alloy is the bond coat material as an oxidation-resistant metallic layer[12].

The anisotropy of their thermal conductivities can cause the non-uniformity of temperature distribution and therefore a short life time. The investigation of the anisotropy can provide some information about the coating performance and thus the clue to coating design. In this study, the through thickness and in plane thermal conductivities were determined to examine anisotropy of APS Mo and APS CoNiCrAlY coatings, as shown in Fig. 7.7. The interesting phenomenon observed is that the values of anisotropy for both APS Mo and CoNiCrAlY coatings are lower than 1, which means lower thermal conductivity in the through thickness direction than the in-plane direction. The results are contradictory to ceramic coatings, such as YSZ and Al_2O_3 coatings. This is because the spread of the droplet provides very large area for the surface parallel to the substrate but only a very small area for the surface perpendicular to the substrate. The large surface

area has more chances to contact air and generate oxidation. And the oxidation reduces the through thickness thermal conductivity dramatically and therefore reverses the anisotropy of thermal conductivity to be lower than 1. The effect of oxidation on the reduction of anisotropy of thermal conductivity appears more distinctly for Mo coating than CoNiCrAlY coating. The thermal conductivity of APS CoNiCrAlY coating is influenced by impurity both through thickness and in-plane directions. The in-plane thermal conductivity also drops a lot due to the effects of both impurity and oxidation. The effect of impurity on thermal conductivity is isotropic although the higher content of oxidation causes a larger reduction in the through thickness thermal conductivity. The inclusion of impurity mitigates the influence of oxidation on the ratio of Ktt/Kip. Thus, the anisotropy is enhanced to a certain extent. In the case of the single element metal–Mo coating is lack of the effect of impurity and the different extent of oxidation plays a dominant role in the anisotropy of thermal conductivity. Therefore, APS Mo coating has lower value of anisotropy than APS CoNiCrAlY coating.
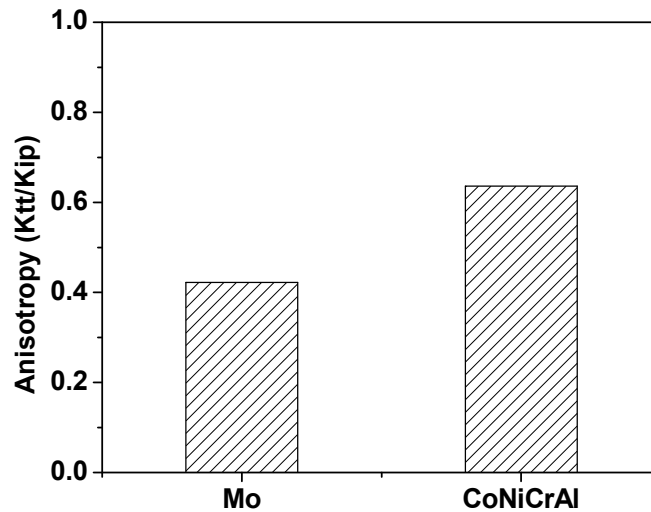
Figure 7.7 The anisotropy of thermal conductivity for APS metallic coatings

7.4 Conclusions

Two laser techniques, HLF and Laser PIT, were adopted to explore the anisotropy of thermal conductivities for three material systems including YSZ, Al_2O_3 and metallic coatings. For YSZ coating, these two techniques were compared for the measurements of in plane thermal conductivities and the Laser PIT instrument showed much better accuracy than HLF instrument despite of similar average value. For the YSZ coatings, the effect of porosity, powder morphology and particle state on anisotropy were examined. It is found that the increase of porosity decreases the anisotropy due to reduced flattening

ratio of splats and more randomized pore orientation. The thermal conductivities of the YSZ coating with graded porosity are located below the dotted rule-of-mixtures line. The percolation theory is applied for interpreting the effect of anisotropic microstructural defects on the thermal transport property. The variation of powder morphology has little influence on in plane thermal conductivities of YSZ coatings but a remarkable effect on though thickness thermal conductivities. The thorough thickness thermal conductivity determines the anisotropy of thermal conductivity F&C>A&S>HOSP. This trend is consistent with the previous analysis of microstructures by using SANS for the coatings made of three morphology powders that show lower interlamellar porosity than cracks. Another notable observation for YSZ coating is that high temperature and velocity leads to low porosity and therefore high anisotropy. The Al_2O_3 coatings sprayed by three techniques follow the rule that the high porosity decreases the anisotropy except the HVOF Al_2O_3 coating. The HVOF Al_2O_3 coating has the lowest anisotropy as a result of the contribution from more interfaces. For metallic coatings, the oxidation reverses the anisotropy of thermal conductivity to be lower than 1. This is due to the more oxidation which occurred on the surface parallel to the substrate than on the surface perpendicular to the substrate. The oxidation reduces the through thickness thermal conductivity dramatically and therefore reverses the anisotropy of thermal conductivity to be lower than 1.This study provides a framework to understand and design multifunctional multiphase coatings with novel microstructure and property.

References

1.   E. Morf, *U.S. Patent 28001 A. D.* , 1912.

2.   S. Sampath, X. Y. Jiang, J. Matejicek, L. Prchlik, A. Kulkarni and A. Vaidya, Role of thermal spray processing method on the microstructure, residual stress and properties of coatings: an integrated study for Ni-5 wt.%Al bond coats, *Materials Science and Engineering a-Structural Materials Properties Microstructure and Processing*, Vol. 364, No.1-2, 2004, p. 216-231.

3.   W. Chi, S. Sampath and H. Wang, Ambient and High Temperature Thermal Conductivity of Thermal Sprayed Coatings, *Journal of Thermal Spray Technology*, Vol. 15, No.4, 2006.

4.   H. Herman, Plasma Sprayed Coatings, *Sci American*, Vol. 259, No.3, 1988, p. 112-117.

5.   R. McPherson, The Relationship between the Mechanism of Formation, Microstructure and Properties of Plasma Sprayed Coatings, *Thin Solid Films*, Vol. 83, No.3, 1981, p. 297-310

6.   A. Kulkarni, Z. Wang, T. Nakamura, S. Sampath, A. Goland, H. Herman, J. Allen, J. Ilavsky, G. Long, J. Frahm and R. W. Steinbrech, Comprehensive microstructural characterization and predictive property modeling of plasma-sprayed zirconia coatings, *Acta Materialia*, Vol. 51, No.9, 2003, p. 2457-2475.

7.   S. Deshpande, A. Kulkarni, S. Sampath and H. Herman, Application of image analysis for characterization of porosity in thermal spray coatings and correlation with small angle neutron scattering, *Surface & Coatings Technology*, Vol. 187, No.1, 2004, p. 6-16.

8.   Z. Wang, A. Kulkarni, S. Deshpande, T. Nakamura and H. Herman, Effects of pores and interfaces on effective properties of plasma sprayed zirconia coatings, *Acta Materialia*, Vol. 51, No.18, 2003, p. 5319-5334.

9.   L. N. Smith and C. J. Lobb, Percolation in 2-Dimensional Conductor-Insulator Networks with Controllable Anisotropy, *Physical Review B*, Vol. 20, No.9, 1979, p. 3653-3658.

10.   A. Kulkarni, S. Sampath, A. Goland, H. Herman and B. Dowd, Computed microtomography studies to characterize microstructure-property correlations in thermal sprayed alumina deposits, *Scripta Materialia*, Vol. 43, No.5, 2000, p. 471-476.

11. S. Sampath and S. F. Wayne, Microstructure and Properties of Plasma-Sprayed Mo-Mo$_2$C Composites, *Journal of Thermal Spray Technology*, Vol. 3, No.3, 1994, p. 282-288.

12. N. P. Padture, M. Gell and E. H. Jordan, Materials science - Thermal barrier coatings for gas-turbine engine apptications, *Science*, Vol. 296, No.5566, 2002, p. 280-284.

Chapter 8.

The Evaluation of Various Measurement Techniques for Thermal Conductivity

8.1 Introduction

Thermally sprayed coatings have been widely used as prospective systems that fulfill various functions such as corrosion resistance, wear resistance, thermal barriers, electrical insulation or conductive contact, biomedical applications [1-3]. Some coatings are also used to restore worn or poorly machined parts to the original dimensions and specifications, or for their capability in near-net-shape manufacturing of high performance ceramics, composites, refractory metals and functionally graded materials[4]. The thermal transport property of the thermally sprayed coatings is a very important design parameter. Furthermore, the measurement of the thermal transport property of thermally sprayed coatings itself provides a challenge given the complex architecture of defects and interfaces in the system. Development of precise and reliable measurement methods becomes an important step in the study of the thermal transport property of thermally sprayed coatings. Significant attention has been directed increasingly towards characterizing, understanding and controlling the thermal transport property. Since its introduction in 1961[5], the laser flash technique has become a standard testing method for the thermal transport property measurements of solids [6]. The measurement requires the materials to be opaque to the wavelength of pulse and infrared, and two assumptions (all the pulse energy is absorbed in one side and all the thermal radiation of the other side is measured by IR) are tenable [7]. A complex laser flash system may not always be required for the routine measurement. The xenon flash technique, an alternate approach to characterization of the thermal transport property, has been developed recently in Oak Ridge National Laboratory (ORNL). Detector signal monitoring, data acquisition and analysis are integrated into one executable program [8].

In this work, we adopt both the laser and xenon flash techniques to study the thermal transport property of various thermally sprayed coatings in which either phonons or electrons are the predominant heat transporters. By investigating thermal properties of

an insulating ceramic, conducting alloys, and mixed phase composites, a range of information on the thermal transport property of thermally sprayed coatings are obtained. Our efforts aim to examine the measurement repeatability and precision of the laser and xenon flash diffusivity techniques as well as the effect of different factors on the thermal transport properties of various thermally sprayed coatings.

8.2. Experiment Measurement

Free standing coatings were obtained by grinding the substrate to 100-300μm and then detaching the coating from the substrate. The ambient through thickness thermal diffusivity measurements were carried out on 12.7mm disks coated with graphite by using both laser and xenon flash techniques.

8.2.1 Holometrix Laser Flash Instrument (HLF)

μ-HLF can be used to measure the thermal diffusivity of metals, coatings, composites, ceramics, polymers and so on. The thermal diffusivity of a material is usually tested by rapidly heating one side of a sample and obtaining the temperature rise curve on the opposite side [9]. The heat flux lines are assumed to be parallel and directed through the sample without heat flow in the plane. The excitation wavelength of the laser pulse is 1.06μm. The laser pulse has emitted energy up to 35 Joule and its pulse time is 0.33ms. The time taken for the back surface to reach half its maximum temperature ($t_{1/2}$) should be at least three times longer than the length of the laser pulse and no longer than 3s.

Figure 8.1 shows the reproducibility of this instrument for measuring thermal conductivity at ambient temperature. To determine the measurement accuracy of this instrument, one standard sample and 6 YSZ coating samples were studied. The thermal conductivity of standard sample (pyroceramic disk) was measured for 9 times. The coefficient of variation is 1.8%. For an experimental plasma sprayed YSZ specimen, 9 measurements were made with resulting in a coefficient of variation 5%. From the same coating, 6 separated specimens were made and 9 measurements were taken for each specimen. The coefficient of variation is 8%. From these measurements, the accuracy of Holometrix laser flash thermal property instrument was found of the order 8% for through thickness measurement.

8.2.2 Xenon Flash Thermal Diffusivity (XFTD) System

The XFTD system (Fig. 8.2) was developed using LabView (National Instruments Corporation, Austin, TX) program based on the factors of simplicity, economy and reliability. The pulse energy is 12 Joule and the pulse time is 6~8ms. The excitation wavelength is not a simple number since the xenon pulse is not monochromatic light. It is calculated using the field of view (or solid angle) to view 0.8 cm diameter area of the sample. So this design maximizes the signal. Also, the infrared detector and the sample holder are completely shielded from the flash source by multiple shielding layers and addition of reflecting surfaces [8]. Thus, the xenon energy is prevented from over heating the detector and holder, which decreases the rear face temperature rise with a good enough signal-to-noise ratio. Another advantage of the XFTD system is that the

temperature drift before the shot is recorded and taken into consideration. The detector output signal is monitored from the beginning of the test and in between each shot, which assures that the following flash starts only if the temperature of the sample is steady [8]. That is, the pre-shot monitoring feature ensures no uncontrolled baseline drift and the same equilibrium condition of each fired shot.
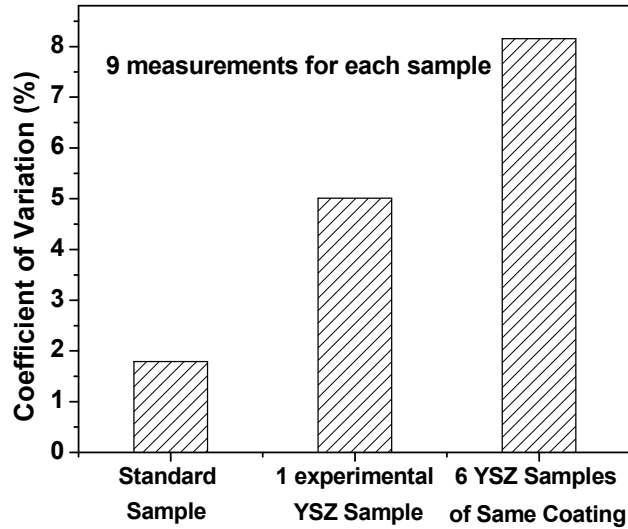

Figure 8.1 Fidelity of laser flash thermal conductivity instrument for room temperature.
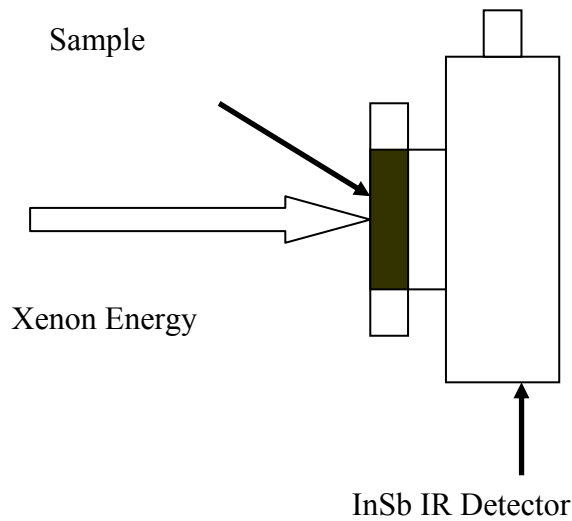

Figure 8.2 Schematic of IR detector with sample of xenon flash diffusivity system

Reliable measurement of thermal diffusivity in many cases can be obtained through the xenon flash technique. Xenon flash thermal diffusivity system is optimized for room-temperature thermal diffusivity measurements of ceramics, metals, composites, and coatings. However, this system can not be used to measure thermal conductivity directly. A separate Differential Scanning Calorimeter (DSC) system is necessary to measure Cp in order to calculate thermal conductivity and its accuracy is about 1-2% [9]. The formula for thermal conductivity calculation is K=αρCp, where K is the thermal conductivity, ρ is the bulk density and Cp is the specific heat. The accuracy of XFTD is somewhat better than that of laser flash instrument due to the short detector to sample distance and high signal to noise ratio.

8.3. Results and Discussion

8.3.1 Yttria Stabilized Zirconia Ceramic Coatings Made of Three Different Morphology Powders

Ceramic materials are thermal insulators due to the lack of a large number of free electrons. Consequently, the phonon conduction mechanism predominates for thermal transport. YSZ, as a ceramic material with very low thermal diffusivity, has long been adopted to make thermal barrier coatings (TBCs) for components in gas turbine and diesel engines [10, 11]. The thermally sprayed coating has lower thermal diffusivity than the bulk material with the same composition due to the contribution of microstructural features (pores, cracks,…) [12]. By controlling the temperature and velocity in a very narrow range for air plasma spraying (APS), YSZ ceramic coatings were made of three different morphology powders: the fused and crushed (FC), the agglomerated and sintered (AS), the plasma densified (HOSP). Their thermal diffusivities were examined by both HLF and XFTD and shown in Fig. 8.3 (a). Each sample was measured 9 times to determine the measurement repeatability of these two techniques. The values of thermal diffusivities measured by two methods are very close. The laser flash data are marginally higher due to little shorter pulse time and half rise time $t_{1/2}$ of laser than that of xenon (α is inverse to $t_{1/2}$). This demonstrates the fidelity of the thermal diffusivity measurements for the plasma sprayed YSZ coatings.

Figure 8.3 (b) shows the comparison of repeatability of the HLF and XFTD for measuring the thermal diffusivities of these three coatings at ambient temperature. The measurement scatter of the xenon flash technique is much lower than that of the laser flash technique. For each coating, the coefficient of variation (CV, the ratio of the standard deviation to the mean) obtained by the XFTD is lower than half of that obtained by HLF. One reason is that the field of view is 0.8cm diameter area of the sample and therefore the signal is maximized. The other reason is that the typical specimen rear face temperature rise by xenon pulse is 1-2°C (only 1/5-1/3 of the rise by laser pulse), which causes very little noise. Thus, excessive temperature increase, which drives the IR detector into a nonlinear temperature-voltage response and thereby leads to significant errors in thermal diffusivity measurement, is avoided. The development of the xenon

flash technique provides the ability to achieve high repeatability of thermal diffusivity measurement of YSZ ceramic coatings.
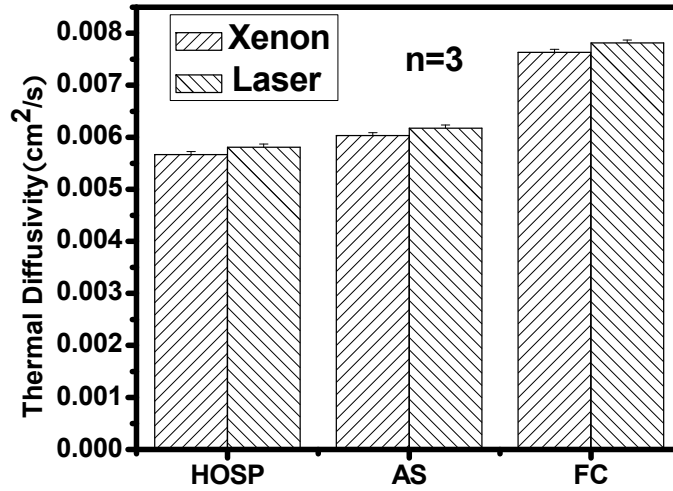
(a)
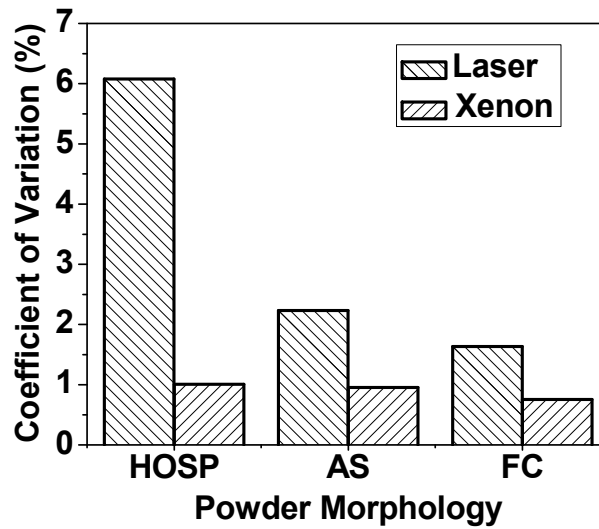
(b)

Figure 8.3 The measurement repeatability of laser and xenon flash techniques for YSZ coatings made of three different morphology powders (a) thermal diffusivity (b) coefficient of variation

8.3.2 High Thermal Diffusivity Coatings

Thermal diffusivity measurements were also conducted for plasma sprayed Si and Mo coatings. Figure 8.4(a) shows the thermal diffusivities obtained by both laser flash and xenon flash techniques. The results show large discrepancy for Si thermal diffusivity by these techniques, with the xenon flash reporting much lower than that from laser flash. Here the laser flash data is more appropriate to consider for the measured coatings. The time taken for the back surface to reach half its maximum temperature ($t_{1/2}$) should be at least three times longer than the pulse time. Due to high thermal diffusivity, $t_{1/2}$ of xenon flash is smaller than the optimum range which causes much bigger error for xenon than laser because of longer pulse time of xenon. For the metal molybdenum coating, two samples are measured: one is thick (about 1.1mm) and the other is thin (0.45mm). For the thick samples, the thermal diffusivities measured by xenon flash and laser flash are similar. But for the thin sample, the result of laser flash is much higher than that of xenon flash. Again, the $t_{1/2}$ of xenon flash is smaller than the optimum range (3 times larger than xenon pulse time) because of too small thickness and the correction for the finite width of the pulse becomes severe. For metal coatings, this causes the substantial error for xenon flash but not for laser flash due to longer pulse time of xenon. Figure 8.4 (b) shows the coefficient of variation of thermal diffusivities obtained by both laser and xenon flash techniques for Si and Mo Coatings. The xenon flash techniques indicates larger scatter of measured values due to high thermal diffusivity of Si and Mo.

8.3.3 High Purity Metal Coatings

In high purity metals, the electron mechanism of heat transport is much more efficient than the phonon contribution. The reasons are: (i) electrons are not as easily scattered as phonons (ii) electrons have higher velocity than phonons (iii) large numbers of free electrons exist and participate in thermal conduction.

Silver has one of the highest thermal diffusivities among metals. Ag is also one of the stable pure metals difficult to be oxidized in the nature. In this study, Ag was used to make different thickness (1.3mm and 2.8mm) coatings by APS.

The thermal diffusivities measured by both the laser and xenon flash techniques are shown in Fig. 8.5(a). The thermal diffusivities obtained by HLF are close for both thin and thick coatings. The results obtained by XFTD are much lower than those obtained by HLF. The thermal diffusivities of thin and thick Ag coating measured by XFTD decrease by about 90% and 40% respectively compared to that measured by HLF. Here the laser flash data are more appropriate to consider for the measured coatings. To obtain reliable results, the time taken for the back surface to reach half its maximum temperature ($t_{1/2}$) should be at least three times longer than the pulse time. The high thermal diffusivity of Ag makes $t_{1/2}$ deviate from the optimum range for the xenon flash with a longer pulse time (6~8ms). This problem has already been found for other metal coatings, such as thin Mo coating [9]. But the deviation from the optimum range disappeared when the thickness reached 1.1 mm. In the case of the Ag coating, the thicknesses of 1.3 mm and

2.8 mm are still not enough to enter the $t_{1/2}$ into the optimum range for the xenon flash. Thicker Ag coating is needed to obtain reliable measurement results for the XFTD. The measurement scatter is reflected in the CV (Fig. 8.5(b)) of the thermal diffusivity obtained by these two techniques. CVs of the thermal diffusivity obtained by the XFTD are 5 times (thin coating) and 3 times (thick coating) as high as those obtained by the HLF. Therefore, the XFTD is not suitable to measure high thermal diffusivity coatings unless the coatings are produced to appropriate thickness.
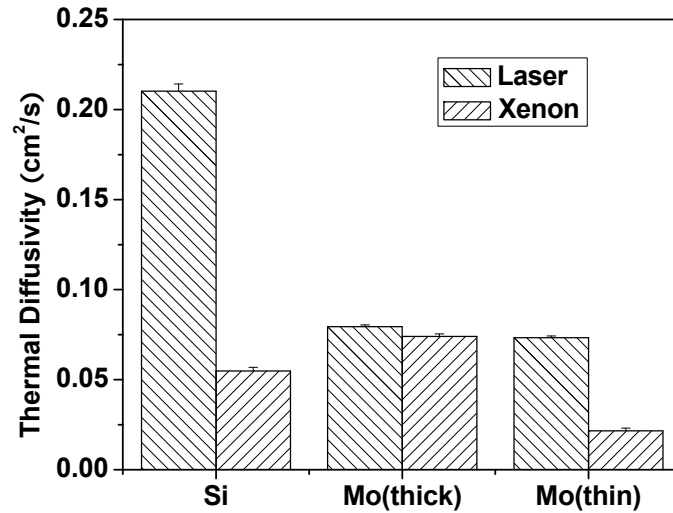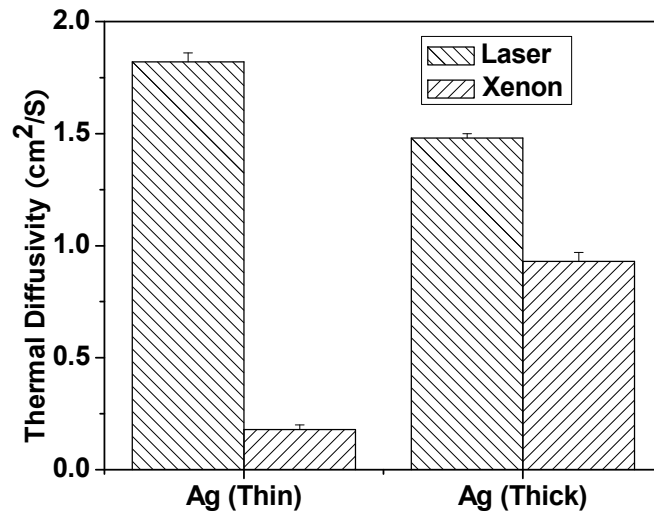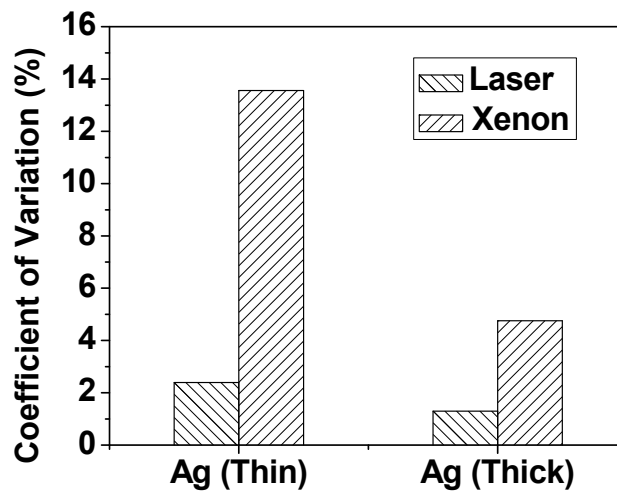
(a)
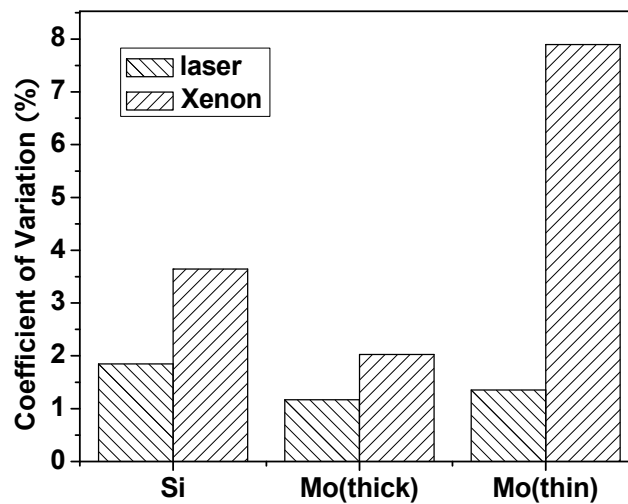
(b)

Figure 8.4 Thermal diffusivity measurements by xenon and laser flash at room temperature of semiconductor and metal coatings (a) thermal diffusivity (b) coefficient of variation.

(a)

(b)

Figure 8.5 The measurement repeatability of laser and xenon flash techniques for different thickness Ag coatings (a) thermal diffusivity (b) coefficient of variation

\

8.3.4 Alloy Coatings

Alloying metals result in a reduction in the metal thermal diffusivity. The impurity atoms, especially in solid solution, act as the scattering centers, lowering the efficiency of electron motion.
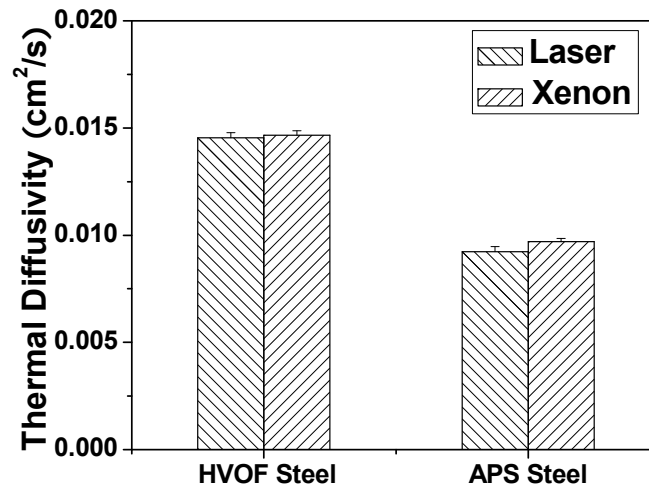
8.3.4.1 Steel coatings

Steel is an alloy of iron with small amounts of carbon, often with other constituents such as manganese, chromium, nickel, molybdenum, copper, tungsten, cobalt, or silicon, depending on the desired alloy properties. In this study, two steel coatings were made by APS and high velocity oxy-fuel (HVOF) techniques using the same powder. The thermal diffusivities of the APS and HVOF steel coatings measured by the HLF and XFTD are shown in Fig. 8.6 (a). The HVOF steel coating has higher thermal diffusivity than the APS steel coating. The reason can be interpreted from the characteristics of the APS and HVOF techniques. The APS process has higher particle temperature, which generates lower viscosity droplets, greater fragmentation of splats and more porous microstructure [13]. The combination of higher kinetic energy and lower thermal energy of the HVOF process compared to the APS promotes the splat-splat contact, improves steel coating density and reduces the microstructural defects. Furthermore, due to the relatively lower temperature and higher velocity of HVOF process, less oxidation occurs. Oxide is brittle and its thermal expansion coefficient is different from steel, which leads to more microstructural defects and changes in the thermal transport properties [14]. Therefore, the smaller amount of porosity and oxide content in the HVOF steel coating results in higher thermal diffusivity. The thermal diffusivities of the HVOF steel coating measured by the HLF and XFTD are close. The laser and xenon flash techniques also give similar thermal diffusivity for the APS steel coating. The thickness of both the HVOF and APS steel coatings is 1.1mm or so. The low thermal diffusivity and sufficient thickness ensure that the $t_{1/2}$ is three times longer than the xenon flash pulse time. Figure 8.6 (b) shows the CV of the thermal diffusivity obtained by the HLF and XFTD. For both the HVOF and APS steel coatings, the xenon flash technique presents lower CV and better repeatability. The reasons are the same as those for the three YSZ ceramic coatings.

8.3.4.2 Tribaloy T-800 coatings

The tribaloy T-800, which belongs to the family of Co-base alloys developed by DuPont in the early 1970s [15], consists of Co, Mo, Cr and Si. In this study, two T-800 coatings were fabricated: one has low oxide, the other has high oxide. The thickness was 1.2 mm for the low oxide T-800 coating and 1.1 mm for the high oxide T-800 coating.

The thermal transport properties were examined by both the HLF and XFTD. Figure 8.7(a) shows the measurement repeatability of the HLF and XFTD. The CV of thermal diffusivity obtained by the XFTD is lower than that obtained by the HLF. This is similar to the case of the three different morphology YSZ ceramic coatings and the steel coatings having low thermal diffusivities. Fig. 8.7(b) shows the thermal diffusivity obtained by the xenon flash technique. The higher content of oxide offers more thermal insulation composition and therefore results in lower thermal diffusivity for the high oxide coating.

(a)
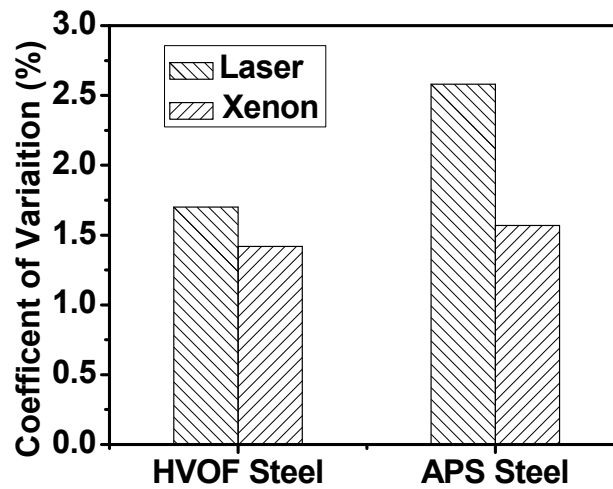
(b)

Figure 8.6 The measurement repeatability of laser and xenon flash techniques for steel coatings (a) thermal diffusivity (b) coefficient of variation

(a)

(b)

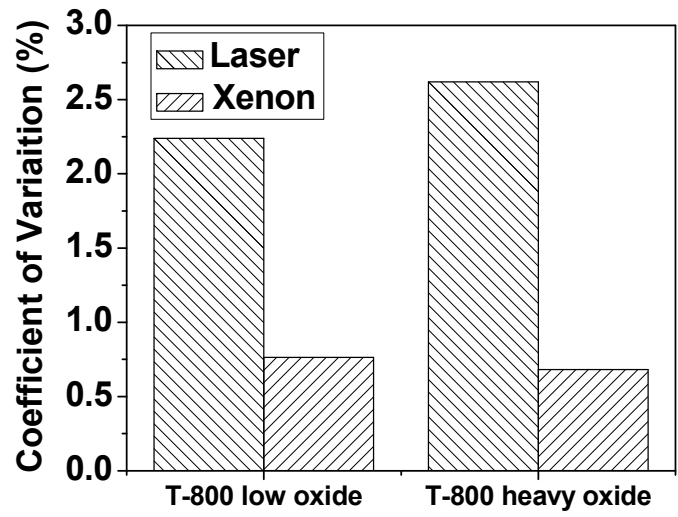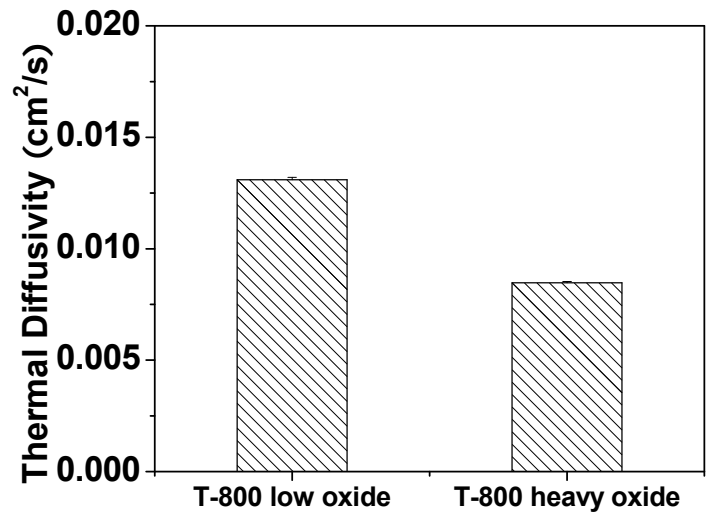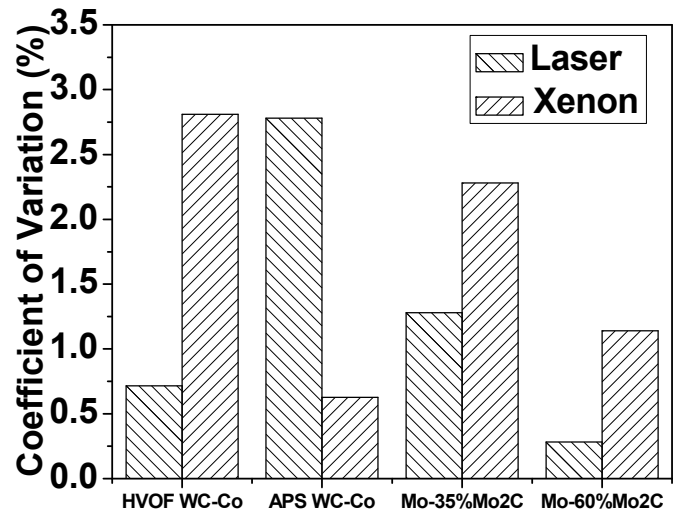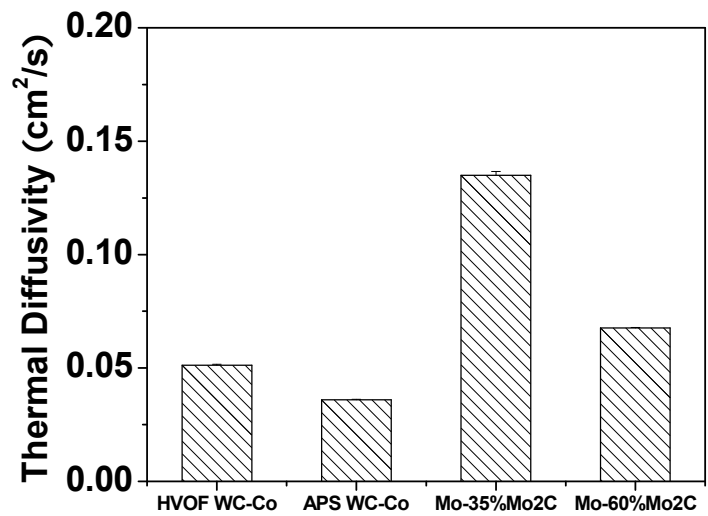Figure 8.7 Thermal diffusivity measurements for tribaloy coatings (a) the measurement repeatability of laser and xenon flash techniques (b) thermal diffusivity

8.3.5 Composite Coatings

Carbide-reinforced composite coatings are widely used in aerospace, pulp and paper, marine, diesel engine and oil industries. Their tribolgical properties have long been studied [16]. However, a limited number of investigations have focused on their thermal transport properties. This work examines the thermal diffusivities of WC-Co coatings and Mo-Mo$_2$C coatings by the HLF and XFTD. Two WC-Co coatings were made by the HVOF and APS. Mo-35%Mo$_2$C and Mo-60%Mo$_2$C powders were used to fabricate coatings by APS. The thickness was 1.2 mm for the HOVF WC-Co coating, 0.33mm for the APS WC-Co coating, 0.7mm for the Mo-35%Mo$_2$C coating and 1.1 mm for the Mo-60%Mo$_2$C coating. Figure 8.8(a) shows the measurement repeatability of the HLF and XFTD for these composite coatings. The CVs of the HVOF WC-Co coating and the two Mo-Mo$_2$C coatings obtained by the HLF are lower than those obtained by the XFTD respectively. The APS WC-Co coating has higher CV of the thermal diffusivity obtained by the HLF than that obtained by the XFTD due to its low thermal diffusivity. In Fig. 8.8(b), the thermal diffusivity of APS WC-Co is obtained by XFTD and the thermal diffusivities of other coatings are obtained by HLF. For WC-Co coating, the HVOF one has higher thermal diffusivity than the APS one, which is the same as the case of the HVOF and APS steel coatings. For Mo-Mo$_2$C coating, the different content of Mo$_2$C results in different thermal diffusivity. The thermal diffusivity is halved by increasing the Mo$_2$C content from 35% to 60%. In Mo-Mo$_2$C coatings, carbon acts as a sacrificial getter for oxygen [17] and increases thermal diffusivity significantly. But with excessive Mo$_2$C, thermal diffusivity reduces since a great deal of carbide is retained in the coating [17].

(a)

(b)

Figure 8.8 Thermal diffusivity measurements for composite coatings (a) the measurement repeatability of laser and xenon flash techniques (b) thermal diffusivity

8.4. Conclusions

Three different morphology YSZ-based thermal barrier coatings, high purity metal coatings, alloy coatings (steel and tribaloy) and metal ceramic composite coatings were investigated in their free standing form so as to discriminate measurement effects on the observed structure-property relationships and examine the measurement repeatability for both the laser and xenon flash techniques. The results indicate that both the laser flash and xenon flash techniques are suitable for measurement of thermal diffusivity of free standing thermally sprayed coatings. However, for low thermal diffusivity coatings, significant scatter in measurement by the laser flash technique was noted. The YSZ ceramic coatings, steel coatings, tribaloy T-800 coatings and APS WC-Co coating had a lower CV for measurements made by XFTD. The xenon flash technique ameliorated the repeatability of measurement for low thermal diffusivity coatings due to a higher signal-to-noise ratio and therefore a better estimation. For the HVOF WC-Co and the APS Mo-Mo_2C coatings, their higher thermal diffusivities exacerbated the XFTD measurement scatter. With the increase in intrinsic thermal diffusivity of the coating, the coefficient of variation of the XFTD technique trends higher. The high thermal diffusivity of Ag coatings even made $t_{1/2}$ deviate from the optimum range for the XFTD and resulted in much lower reliability aside from higher measurement scatter.

References

1.   H. Herman, Plasma Sprayed Coatings, *Sci American*, Vol. 259, No.3, 1988, p. 112-117.

2.   M. R. Dorfman, Thermal spray basics, Part I, *Advanced Materials & Processes*, Vol. 160, No.7, 2002, p. 47-50.

3.   P. Fauchais, A. Vardelle and B. Dussoubs, Quo vadis thermal spraying?, *Journal of Thermal Spray Technology*, Vol. 10, No.1, 2001, p. 44-66.

4.   P. Fauchais, Understanding plasma spraying, *Journal of Physics D-Applied Physics*, Vol. 37, No.9, 2004, p. 86-108.

5.   W. J. Parker, R. J. Jenkins, G. L. Abbott and C. P. Butler, Flash Method of Determining Thermal Diffusivity, Heat Capacity, and Thermal Conductivity, *Journal of Applied Physics*, Vol. 32, No.9, 1961, p. 1679-1684.

6.   L. M. Clark and R. E. Taylor, Radiation Loss in Flash Method for Thermal-Diffusivity, *Journal of Applied Physics*, Vol. 46, No.2, 1975, p. 714-719.

7.   H. Wang and R. B. Dinwiddie, Reliability of laser flash thermal diffusivity measurements of the thermal barrier coatings, *Journal of Thermal Spray Technology*, Vol. 9, No.2, 2000, p. 210-214.

8.   H. Wang and R. B. Dinwiddie, Development of a LabViewTM Based Portable Thermal Diffusivity System, *Thermal Conductivity 27/Thermal Expansion 15* 2004, p. 484-492.

9.   W. Chi, S. Sampath and H. Wang, Ambient and high-temperature thermal conductivity of thermal sprayed coatings, *Journal of Thermal Spray Technology*, Vol. 15, No.4, 2006, p. 773-778.

10.   R. A. Miller, Current Status of Thermal Barrier Coatings - an Overview, *Surface & Coatings Technology*, Vol. 30, No.1, 1987, p. 1-11.

11.   H. Herman, S. Sampath and R. McCune, Thermal spray: Current status and future trends, *Mrs Bulletin*, Vol. 25, No.7, 2000, p. 17-25.

12.   A. Kulkarni, Z. Wang, T. Nakamura, S. Sampath, A. Goland, H. Herman, J. Allen, J. Ilavsky, G. Long, J. Frahm and R. W. Steinbrech, Comprehensive microstructural characterization and predictive property modeling of plasma-sprayed zirconia coatings, *Acta Materialia*, Vol. 51, No.9, 2003, p. 2457-2475.

13.   S. Sampath, X. Y. Jiang, J. Matejicek, L. Prchlik, A. Kulkarni and A. Vaidya, Role of thermal spray processing method on the microstructure, residual stress and properties of coatings: an integrated study for Ni-5 wt.%Al bond coats, *Materials Science and Engineering a-Structural Materials Properties Microstructure and Processing*, Vol. 364, No.1-2, 2004, p. 216-231.

14.   S. Deshpande, S. Sampath and H. Zhang, Mechanisms of oxidation and its role in microstructural evolution of metallic thermal spray coatings - Case study for Ni-Al, *Surface & Coatings Technology*, Vol. 200, No.18-19, 2006, p. 5395-5406.

15.   C. Navas, M. Cadenas, J. M. Cuetos and J. de Damborenea, Microstructure and sliding wear behaviour of Tribaloy T-800 coatings deposited by laser cladding, *Wear*, Vol. 260, No.7-8, 2006, p. 838-846.

16.   L. Prchlik, S. Sampath, J. Gutleber, G. Bancke and A. W. Ruff, Friction and wear properties of WC-Co and Mo-Mo2C based functionally graded materials, *Wear*, Vol. 249, No.12, 2001, p. 1103-1115.

17.   S. Sampath and S. F. Wayne, Microstructure and Properties of Plasma-Sprayed Mo-Mo$_2$C Composites, *Journal of Thermal Spray Technology*, Vol. 3, No.3, 1994, p. 282-288.

Chapter 9.

Conclusions

This dissertation has examined thermally sprayed coatings made of a range of materials in an effort to establish the relationships between microstructural defects and thermal transport property. As discussed in the introduction, the thermally sprayed coatings exhibit thermal conductivity in the range of 10% to 90% of bulk values, and the coating thermal conductivity is dependent on intrinsic attributes of materials and the extrinsic effects arising from microstructure. Quantifying and categorizing microstructural characterization of thermal spray coatings are not only the bridge of linking microstructure with process but also of better understanding the correlation between microstructure and thermal conductivity. A comprehensive and integrated investigation has been performed, considering the defect architecture and anisotropic nature of coatings. In the case of oxides, the effect of thermal exposure and the associated dynamic changes on the microstructure-property relationship has also been considered. Finally, the thermal transport measurement of metallic and ceramic coatings has itself been critically addressed in terms of data repeatability and thickness considerations. This work provides a fundamental basis to coating material selection and design with consideration of thermal properties. It also offers a pathway to understanding the role of chemistry, processing effects and microstructure for a spectrum of materials systems. The key conclusions of the research are outlined in the following aspects.

Porosity-Thermal Conductivity Maps for Ceramic Coatings

The thermal transport property of thermally sprayed coatings is intimately related to the starting microstructure. New developments in advanced diagnostics and process control have allowed for manipulation and control of the plasma spray particle stream enabling synthesis of coatings with factored microstructures. A range of starting microstructures were achieved for three sets of plasma sprayed YSZ coating systems made using different morphology powders, different particle size distribution and controlled modification of particle states via plasma torch parameters. The thermal conductivity-porosity relationships for the coatings produced with controlled changes in

process conditions and resulting microstructures were systematically examined. Such a systematic approach enables distilling the intrinsic microstructural differences achieved through feedstock and process modifications and enables a critical assessment of the process variables on the resultant thermal properties of the coating. The results clearly suggest that a range of thermal conductivities can be achieved from these starting microstructures offering potential for microstructural tailoring for desired performance. This expansive study of a range of coatings based on feedstock or processing differences has also allowed synthesis of the results through thermal conductivity-porosity maps and has allowed elucidation of the contributing microstructural components on both the ambient and high temperature thermal conductivity. All the commonalities in the observed results from the three sets of coatings were synthesized to establish such a mapping strategy to enable future coating design and process optimization. From the thermal conductivity-porosity maps, it is found that the effective starting microstructure determines both the room temperature and temperature dependent thermal conductivity of coatings. The important role of interlamellar porosity associated with splat based assemblage on both room temperate and temperature dependent thermal conductivity of ceramic coatings has been pointed out. The difference of splat thickness results in different amount of interfaces and thus dominates the thermal response of the material.

Thermal Cycling and Isothermal Exposure

Thermal barrier coatings offer improved operating efficiency and increase durability of hot-section in gas turbine. The pores in thermal barrier coatings reduce thermal conductivity as compared to bulk material and are favorable to the application. But the pores are prone to high temperature sintering which can reduce or even eliminate the conductivity reduction benefit. The dynamic evolution of microstructure and property during service offers a significant challenge in critically defining the design strategies and extended coating performance. To understand the effect of thermal exposure on coating microstructure and thermal conductivity, studies were performed for thermally cycled and isothermally aged TBCs. The selection of these thermal aging conditions is based on respective application issues in aeroengine and land based turbine applications. The land based turbines experience prolonged exposure at high temperatures while the aeroengine turbines experience more cyclic environments. The results demonstrate that different as-deposited microstructures display varying propensity for sintering and need to be considered in the design and manufacturing cycle. The larger open dimension of interlamellar pores is unfavorable to sintering and leads to less increase of thermal conductivity after thermal aging. Another notable observation is that the dominant role of radiation contribution to thermal conductivity decreases the differences of the high temperature thermal conductivity increase before and after thermal aging and changes the variation trend of high temperature thermal conductivity as compared to room temperature thermal conductivity. In addition, at high temperature, the thermal conductivity shows the same percentage increase for low porosity and high porosity coatings arising from the radiation despite the lower absolute rise of thermal conductivity for high porosity coatings.

Quantitative Characterization for Microstructure

Past research and confirmatory findings of this dissertation suggest that the anisotropic nature of pore architecture results in different effective contributions to resultant through thickness thermal conductivity of thermally sprayed coatings. In an effort to quantify the role of these exemplary features, we seek in this dissertation to identify a unified single porosity parameter that captures the weighted contribution of these features. Termed "effective porosity", this parameter provides for a better understanding of microstructure-thermal transport property relationships according to the heat resistance principle by treating different morphology pores play a role as a second phase. This new approach is based application of fundamental work on pore shape effects on thermal conductivity for idealized material by Loeb et al.. By combining effective porosity with linear fit and percolation model, it was successful in interpreting the relationships between microstructural defects and thermal conductivity from the point view of the phase nature of pores. The new microstructural parameter and the two proposed models can be used as predictive tools in industrial applications for microstructure design and quantitative estimate of the thermal conductivity change under persistent thermal exposure.

Anisotropy and Percolation

Two laser techniques, laser flash and scanning-laser-heating, were adopted to explore the anisotropy of thermal conductivities for three material systems including YSZ, Al_2O_3 and metallic coatings. The comparison of measurement accuracy of these two techniques for the in-plane thermal conductivity of the YSZ coatings was carried out and the PIT instrument showed much better accuracy than HLF instrument despite similar average values. As for the YSZ coatings, the effects of porosity, powder morphology and particle state on the anisotropy were also examined. A percolation model was employed for interpreting the anisotropic variations of the thermal transport property from the theoretical aspects of amorphous solid physics. It is found that the increase of porosity results in a decrease the anisotropy due to reduced flattening ratio of splats and more randomized pore orientation. For Al_2O_3 coatings, the effect of spray techniques on the anisotropy has been evaluated. It is observed that the HVOF Al_2O_3 coating has the lowest anisotropy as a result of the contribution from more interfaces. The study for metallic coatings reveals that the oxidation reverses the anisotropy of thermal conductivity to be lower than 1. This is due to the more oxidation which occurred on the surface parallel to the substrate than on the surface perpendicular to the substrate. The oxidation reduces the through thickness thermal conductivity dramatically and therefore reverses the anisotropy of thermal conductivity to be lower than 1. The examination of the NiCrAlY-YSZ FGMs displays that the anisotropic microstructures result in lower thermal conductivities than obtained by rule-of-mixtures and therefore nonlinear behavior of thermal conductivity with respect to YSZ content.

Materials and Process Effects on Thermal Conductivity of Thermal Spray Coatings

A systematic assessment of thermal transport property of a wide range of materials was carried out to critically evaluate the role of material chemistry and processing effects on the thermally sprayed coatings. For single elemental metallic coatings, the intrinsic attributes of materials and extrinsic effects determine the thermal transport property. The intrinsic attributes are related to crystal structure, atomic structure and grain size and boundaries. The extrinsic effects arising from process include oxide content/morphology and microstructure defects. For Ni and Co based alloy coatings, in order to clarify these respective roles, a map of the thermal conductivity with respect to density and other characteristics were developed. The combination of the intrinsic and extrinsic effects makes the alloy coatings fall into different zones where the thermal conductivity is dominated by distinct mechanisms. The effect of intrinsic attributes of materials is reflected by the fact that the coating thermal conductivity decreases with the increase of alloying elements. The extrinsic effects include oxidation and microstructure defects resulting from different spraying process. A generalized rationalization will provide new insights into coating design and processing.

Techniques for Thermal Conductivity Measurements

Three flash diffusivity techniques were adopted to examine the thermal transport properties of a variety of thermally sprayed coatings: metals, alloys, cermets, semiconductor and ceramics. The results indicate that both the laser flash and xenon flash techniques are suitable for thermal conductivity measurement of free standing coatings. However, for low thermal conductivity coatings, significant scatter in measurement by the laser flash technique was noted. The YSZ ceramic coatings, Mo coatings, Si coating, steel coatings, tribaloy T-800 coatings and APS WC-Co coating have a lower coefficient of variation (CV) for measurements made by XFTD. The xenon flash technique to some extent enhances the repeatability of measurement for low thermal conductivity coatings due to a higher signal-to-noise ratio and therefore a better estimation. But for the HVOF WC-Co and the APS Mo-Mo$_2$C coatings, their higher thermal conductivities exacerbate the XFTD measurement scatter. With the increase in intrinsic thermal conductivity of the coatings, the coefficient of variation for the XFTD technique trends higher. The high thermal conductivity of Ag coatings even makes $t_{1/2}$ deviate from the optimum range for the XFTD and results in much lower reliability aside from higher measurement scatter. For the case of metal and semiconductor coatings, the coating thickness must also be carefully considered to get accurate information for both the techniques. The high temperature laser flash system using LFTD at ORNL was employed for high temperature thermal property measurement. The microstructural effects are seen in the high temperature results as well indicating the strong role of interlamellar porosity on high temperature thermal barrier effect.

Chapter 10.

Future Work

A systematic study on the effect of materials, processing and microstructural defects on thermal conductivity has been carried out in this dissertation. On the basis of the discussions and conclusions presented in previous chapters, the following research areas are suggested.

Development of Microstructure Assessment (MIP)

The mercury intrusion porosimetry (MIP) is a versatile tool to characterize the microstructural features and can be used to obtain additional characteristics of microstructure. It is essential to understand the measurement methodology and examine the fidelity of MIP to ensure the reliable analysis for the pore information. Valuable contributions can be made by combining the pore size distribution with porosity investigated previously for further exploring the microstructure-property relationship. A deeper and more comprehensive investigation will be expected for the effect of microstructural defects on the thermal transport property. Preliminary result for pore size distribution of YSZ coating obtained by MIP is shown in Fig. 10.1. The bimodal feature for the pore size distribution is consistent with the presence of globular pores, interlamellar pores and cracks. The confirmation for the reliability of the results and the further investigation of the relationship to thermal conductivity are needed.

Anisotropy of Various Coatings

Limited experiments have been carried out for the investigation of the anisotropy of thermal conductivity in these coatings. More experimental data can be attained by performing the in-plane thermal conductivity measurements for a range of materials in collaboration with ORNL to evaluate anisotropy of thermal transport property. The effect of other factors on anisotropy, such as chemical composition, spray technique, process parameter, and particle size distribution and so on can be examined and the theoretical treatment by using percolation concepts can be developed.
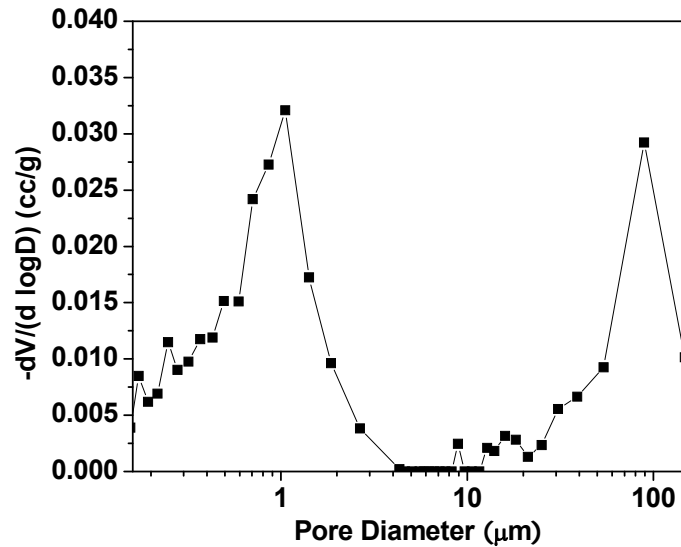
Figure 10.1 Pore size distribution of YSZ coating

Multiple Layer Thermal Conductivity

Some coatings are designed with a thickness much smaller than the minimum value for laser flash technique. The thermal conductivity can not be measured and a method using thermal conductivity equations for two-layer composite is needed to estimate the thermal conductivity of the thin coatings. The thermal conductivities of the two samples (No.1 and No. 2) with coating and substrate as well as substrate only have been tested. The thermal conductivity of YSZ coating can be calculated according to the formula:
Ktotal=Dtotal/[(Dcoating/Kcoating)+(Dsubstrate/Kcoating)]

Dtotal=Dcoating+Dsubstrate, the thickness of the whole button including coating and substrate
Kcoating- thermal conductivity of coating
Dcoating- thickness of coating
Ksubstrate- thermal conductivity of substrate
Dsubstrate- thickness of substrate

The calculated thermal conductivities are shown in Table 10.1.

Table 10.1 Thermal conductivity of thin coatings

Samples	Thickness of free standing (mm)	Thermal Conductivity (W/mK)
No. 1	0.14	3.07
No. 1	0.06	1.62
No. 2	0.14	2.98
No. 2	0.06	1.57

The thickness range of the whole system is from 1.04~1.12mm and the thickness of YSZ coating varies from 0.6~1.4mm. For thickness of free standing, we considered both the designed value 0.14mm and the measured value of some thinner locations. If we use 0.14mm as the coating thickness, we get thermal conductivity of coating around 3W/mK. As we know, thermal conductivity of bulk zirconia is only 2.5~3W/mK. The YSZ coating should have much lower thermal conductivity. If we use 0.6mm as the coating thickness, the coating thermal conductivity is about 1.6W/mK. This value appears reasonable especially when compared to its Electron Beam Physical Vapor Deposited (EB-PVD) counterpart (~ 1.6 W/ m K). Improving this method is favorable for eliminating the difficulty to make freestanding and can be extended to wide application in industry.

Long Term Thermal Cycling

The failure mechanism has long been studied to develop a predictive capability for life time of TBCs. Despite numerous studies for time-at-temperature effect on the failure of TBCs, less work focuses on the systematic examination of thermal cycling effect. The preliminary results for room temperature and high temperature thermal conductivity after different thermal cycles are shown in Fig. 10.2. The experiments involve annealing freestanding deposits for 5, 10 and 20 cycles of heating at 1100 °C for 30 minutes followed by cooling in air for 15 minutes. The increase of thermal cycles leads to higher thermal conductivity of YSZ coatings. The sintering of coatings is relatively fast at the beginning of cycling and then slowly towards latter cycles. But after 20 cycles, the thermal conductivity of coatings is still lower than bulk value. More cycles are required to determine the steady point of thermal conductivity and access the effectiveness of YSZ coatings as TBCs.
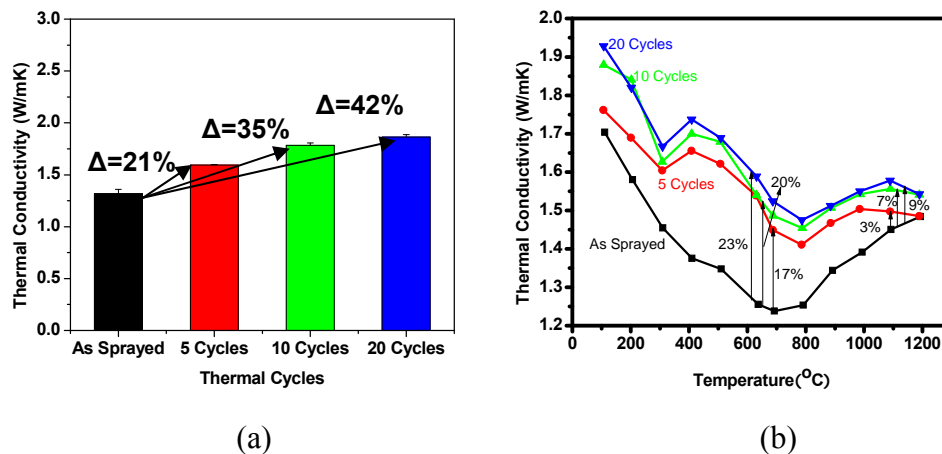

(a)   (b)

Figure 10.2 Effect of thermal cycling on thermal conductivity (a) room temperature (b) high temperature

The Relationship between Thermal and Electrical Conductivity for Elemental Metallic Coatings

The free electrons contribute to both electrical and thermal conductivity for metals and the relationship between thermal conductivity and electrical conductivity of single element metals follows the well known Wiedemann-Franz law. The preliminary work indicated that the thermally sprayed coatings of four single element metals (Ag, Cu, Al Mo and Ni) made by different techniques generally follow the Wiedemann-Franz law. In Fig. 10.3, the thermal conductivities of Ag (APS), Cu (HVOF), Al (APS, HVOF and CS) Mo (APS) and Ni (APS, HVOF and CS) coatings are plotted against their electrical conductivities together with those of the corresponding bulk materials. The microstructural defects generated from thermal spray process reduce the electrical conductivity and the thermal conductivity simultaneously. Linear dependence of the experimental results of the thermal conductivity is observed with respect to the electrical conductivity of the same coating. This fully indicates the dominant role of electrons for conduction. More work needs to be performed to examine and confirm this finding by extending it to a wide range of metallic coatings and investigating the fundamental physical mechanism.
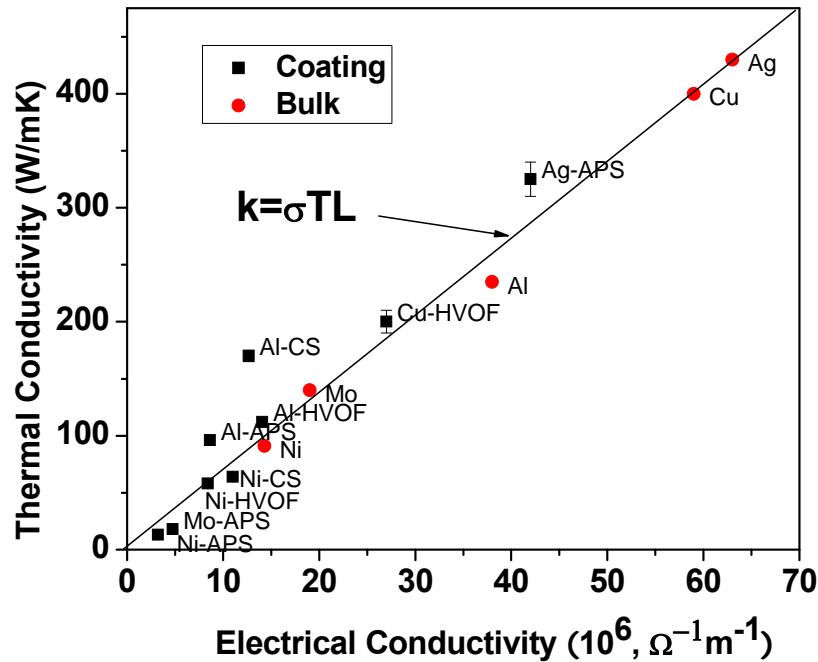

Figure 10.3 Thermal conductivity versus electrical conductivity for various metal bulks and coatings

Thickness Dependent Thermal Conductivity of Mo coatings

For Mo coating, the thickness dependence of thermal property was studied from the point view of heterogeneous evolution of the through thickness microstructure. Fig. 10.4 shows the cross-section of Mo coating, which is separated into 3 sections. [It is unclear as to the origin of such a banded structure. It may be related to process changes or changes in coating-substrate temperature during deposition]. The section near the top has fewer layers and interlamellar pores. The middle section is densified by droplet impaction from the top and forms better contact of layers, which results in fewer defects. The interior layer in contact with substrate includes more layers and interlamellar pores due to impact of top droplets and more defects resulting from mismatch of coefficients of thermal expansion between coating and substrate.

100μm

Microstructure with fewer layers and

With more layers and fewer defects

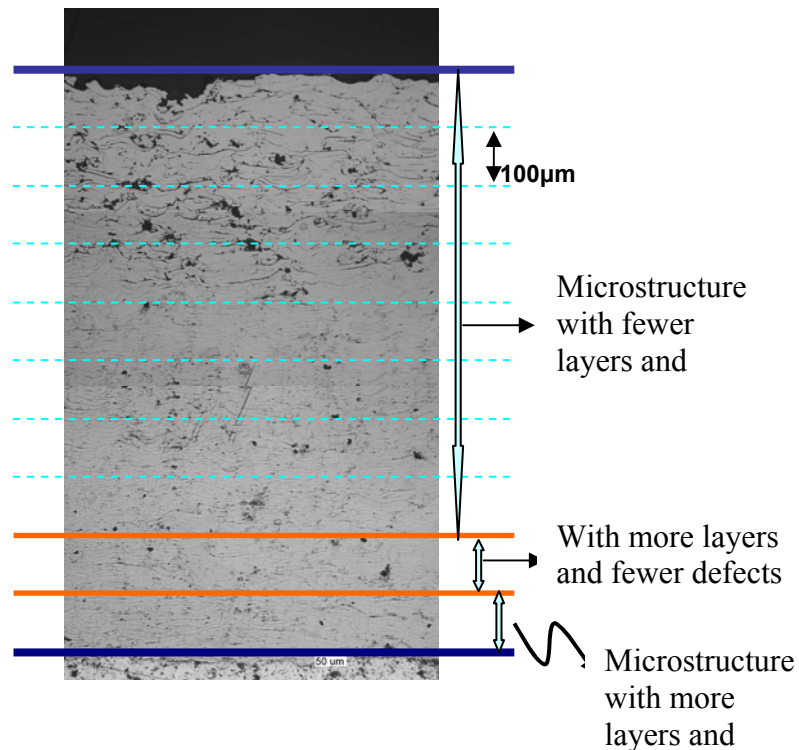Microstructure with more layers and

Figure 10.4 Image of cross section of Mo coating

In order to examine the effect of such a heterogeneous microstructure on thermal property, two coatings were polished (interval 100μm) to get different thickness for property measurement: one was polished from top to bottom and the other was from bottom to top. The thermal conductivity is plotted against thickness as shown in Fig. 10.5. For the coating polished from top to bottom, thermal conductivity continues to decrease. The reason is that the section nearest the top has fewer interlamellar pores, which are the important impediment for heat transport. Therefore, this section plays a role to improve

the thermal conductivity of the whole coating. When the top section is removed more, the thermal conductivity decreases further. For the coating polished from bottom to top, the change of thermal conductivity is difficult to ascertain. Increase of thermal conductivity happens as the first 100μm coating is removed. This is because the section nearest the substrate has more interlamellar pores and defects, which plays a role to reduce the thermal conductivity of the whole coating. After another 100μm coating is removed, thermal conductivity diminishes further. The middle section is densified by impact of subsequent spray droplets and improves contact of among layers. Therefore, the middle section has the function to increase the thermal conductivity of the whole coating, which is even larger than that of the top section. In the succedent steps, thermal conductivity remains almost constant since the rest section is nearly homogenous.
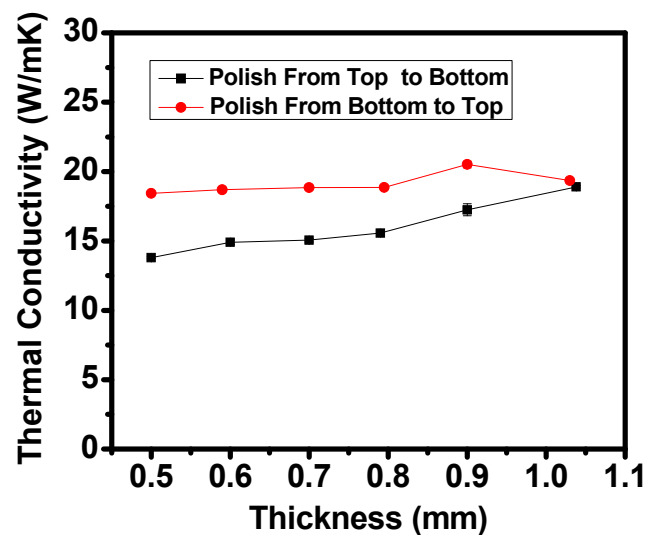

Figure 10.5 Thermal conductivity of different thickness Mo coating

The origin of such a banded structure should be examined from the point of view of process. It is suggested to make Mo coatings with different thickness by either APS or HVOF to assess the effect of impaction on heterogeneous microstructure and property.